# Sensory Modulation of Muscle Synergies for Motor Adaptation during Natural Behaviors

by

Vincent Chi-Kwan Cheung

B. Sc., Mathematics, and Pharmacology & Therapeutics
University of British Columbia, 2000

Submitted to the Harvard-MIT Division of Health Sciences and Technology in partial fulfillment of the requirements for the degree of

Doctor of Philosophy in Neuroscience and Biomedical Engineering
at the
Massachusetts Institute of Technology

February 2007



Signature of author ……...……..
Harvard-MIT Division of Health Sciences and Technology
January 12, 2007

Certified by…….
Emilio Bizzi, M.D.
Institute Professor
Thesis Supervisor

Accepted by……
Martha L. Gray, Ph.D.
Edward Hood Taplin Professor of Medical and Electrical Engineering
Director, Harvard-MIT Division of Health Sciences and Technology

# Sensory Modulation of Muscle Synergies for Motor Adaptation during Natural Behaviors

by

Vincent Chi-Kwan Cheung

Submitted to the Harvard-MIT Division of Health Sciences and Technology
on January 12, 2007 in Partial Fulfillment of the
Requirements for the Degree of Doctor of Philosophy in
Neuroscience and Biomedical Engineering

ABSTRACT

To achieve any motor behavior, the central nervous system (CNS) must coordinate the many degrees of freedom in the musculoskeletal apparatus. It has been suggested that the CNS simplifies this formidable task of coordination by grouping multiple muscles together into units of activation, or muscle synergies. Previous studies have shown that electromyogram (EMG) signals collected from many muscles during natural behaviors can be reconstructed by linearly combining a few synergies, identified by the non-negative matrix factorization algorithm. But to what extent synergies are neural constraints, or merely structures reflecting experimental constraints, has remained an open question. I address this question with the hypothesis that, muscle synergies are robust neural patterns constraining motor outputs. The strategy adopted was that of analyzing EMGs collected before and after delivery of a perturbation to the motor system. In my first experiment, EMGs from bullfrog muscles were recorded during locomotor behaviors before and after deafferentation. Systematic comparison of intact and deafferented synergies suggests that most of the synergies remained unchanged after afferent removal. In my second experiment, the frog hindlimb was perturbed by either an inertial load or an elastic load. Using a novel algorithm capable of simultaneously extracting shared and specific synergies, I demonstrate that, most synergies were shared between the different conditions, but their activation patterns were reversibly altered by loading. Overall, my results suggest that muscle synergies are robust, centrally organized structures, and descending and afferent signals cooperate in modulating their activations so that the resulting motor commands can be efficiently adapted to the external environment.

Thesis Supervisor: Emilio Bizzi, M.D.
Title: Institute Professor, MIT

# Acknowledgments

Back in 1970, the essayist George Steiner has already observed that "[o]verwhelmingly, today, science is a collective enterprise in which the talent of the individual is a function of the group."[1] Indeed, nowadays seldom can one claim to be the sole contributor to any piece of scientific work. The present work is no exception. Several fundamental ideas presented in this thesis owe their provenance to a number of individuals, and to them I express my sincerest gratitude for their teaching, inspiration, and generosity in sharing with me their insights and expertise.

Emilio Bizzi, my thesis supervisor, was the first who demonstrated experimentally the presence of spinal motor primitives represented as force fields (see Bizzi *et al.*, 1991). This idea of modularity within the motor system has led eventually to the formulation of the concept of muscle synergy explored in this thesis. I must thank Prof. Bizzi for his inspiration, encouragement, his teaching of the different surgical and experimental techniques, and more importantly, the vision and perspective that he offered as an established leader in neuroscience. Without his constant support, completion of this thesis would not have been possible.

Philippe Saltiel was one of the first investigators to pursue the concept of muscle synergy as defined in this thesis (see Saltiel *et al.*, 2001). His patience, creativity, and incredible devotion to research even when under severe pressure have been a constant source of inspiration. I have learned from Philippe how an important and general concept could emerge from detailed, meticulous, and repeated inspections of a large amount of raw data.

Matthew Tresch was the first to apply a computational algorithm to identify muscle synergies objectively from electromyogram data (see Tresch *et al.*, 1999), a strategy pursued in this thesis. An extremely generous and knowledgeable scholar, Matthew has kindly shared with me his experiences in the laminectomy and deafferentation surgeries, as well as his view of the synergy concept. I have learned from him how to perform a set of analyses systematically, and also, how to communicate scientific results effectively. In particular, the

[1] George Steiner. *In Bluebeard's castle: some notes towards the redefinition of culture* (New Haven, CT: Yale UP, 1971), 134.

presentations of both chapters 2 and 3 have benefited greatly from his many insights and suggestions.

Andrea d'Avella has spent an enormous amount of time developing the necessary techniques for recording beautiful electromyogram data from a large number of frog hindlimb muscles during natural behaviors. I am very honored to have inherited his recording techniques as well as the frog experimental setup he built for his graduate thesis work (d'Avella, 2000). Many important ideas in my analyses, such as determining the number of synergies using $R^2$ curves, or assessing synergy similarity by estimating the shared subspace dimensionality, were first suggested to me by Andrea. Without his guidance and encouragement, this thesis would certainly not end up in the present form.

I also owe much intellectual debt to Emery N. Brown, who initially referred me to the laboratory of Prof. Bizzi upon knowing that I was interested in performing physiological experiments concerning the motor system. The core idea of chapter 2 – that the non-negative matrix factorization algorithm can be statistically interpreted – in fact owes its origin to Prof. Brown. Furthermore, his open-mindedness and willingness to communicate with people of different intellectual backgrounds will forever serve as a role model of mine. I am also grateful for his support of my participation in the neuroinformatics class held in the summer of 2003 at the Marine Biological Laboratory, Woods Hole, Massachusetts.

In developing the arguments of my thesis, I have benefited enormously from discussions with many of my colleagues and mentors in the Bizzi lab, the Department of Brain and Cognitive Sciences (BCS) at MIT, and also, the Harvard-MIT Division of Health Sciences and Technology (HST). In the Bizzi lab, my labmates – Robert Ajemian, Max Berniker, Maureen Holden, Glenda Lassi Tucci, Silvestro Micera, Simon Overduin, Andrew Richardson, Jinsook Roh, Caterina Stamoulis, and others – have not only been a constant source of emotional support, but also enlightened me in many things over our vibrant discussions during lab meetings. In BCS, I thank Thomas Byrne, Suzanne Corkin, Rutledge Ellis-Behnke, Ann Graybiel, and Gerald Schneider for their many words of wisdom. In HST, I treasure my conversations with Maya Barley, Iahn Cajigas-González, Adrien Desjardins, Lee Gehrke, Steve Massaquoi, Chunyao Jenny Mu, Valerie Pronio-Stelluto, Rajiv Saigal and many others.

Many experiments described in this thesis would have been impossible without the superb technical and administrative assistance of many staff members at MIT and the

Harvard Medical School. I would like to especially thank Margo Cantor, Patty Cunningham, Hannah Diller, Denise Heintze, and Charlotte Potak whose help over the last six years has been essential and critical. Staff at the MIT Division of Comparative Medicine has also contributed greatly by taking good care of the bullfrogs.

Not to be omitted from this acknowledgment section are the several funding agencies and donors who have provided generous financial support to my graduate study. Over the last six years my graduate tuition and stipend have been covered by the MIT Presidential Fellowship, the Chyn Duog Shiah Memorial Fellowship (administered by the MIT Graduate Student Council), the Schoemaker Foundation Fellowship (administered through the MIT McGovern Institute for Brain Research), the HST Fellowship for students in Medical Engineering and Medical Physics, teaching fellowships offered by the BCS department, and funds coming from research grants awarded to Prof. Emilio Bizzi (NIH-NINDS grants NS09343 and NS39865).

Thanks are due to the Society for Neuroscience and IEEE for granting me permission to reproduce previously published materials in the present thesis.

More personally, I would take this opportunity to thank all those who have made my graduate experience so enjoyable, colorful, and satisfying an adventure. My countless over-wine conversations with my apartment-mate, Yue Tan David Tang, have engrossed a permanent mark in both my thinking and my persona. My supervisors in the MIT Department of Music and Theater Arts, including David Deveau, John Harbison, and Marcus Thompson, as well as my collaborators in my chamber music ensemble, including Bonnie Cochran, Mea Cook, Juliet Gopinath, Catherine McCurry, Darius Torchinsky, and Sunny Wicks, have catalyzed my musical maturation. I am grateful for their constant reminder that science is only part of what I want to do in life. Other friends of mine, including Ada Au, Rodney Chan, Showming Sally Kwok, Heiwai Henry Tang, Ernie Yeh, Ernest Wan, Dennis Ming-Yiu Wu, and more recently, Shi Jue, have been the most reliable source of consolation and companionship. Throughout these years, my parents, my sister Joyce Cheuk-Yan, and my brother Jackie Chi-Kit have shown their unlimited love, patience, and support to which I am forever indebted.

V. C. K. C.
Cambridge, Massachusetts
January, 2007

To

Emilio Bizzi, Andrea d'Avella
Matthew C. Tresch, and Philippe Saltiel

*in admiration, respect, and gratitude*

# Contents

# List of figures

# List of tables

*Chapter 1*

# Introduction

In a recently published commentary, Marc Kirschner (2005) speaks eloquently of how systems biology may be understood as "the study of the behavior of complex biological organization and processes in terms of the molecular constituents" (p. 504). Kirschner's description nicely captures the recent enthusiasm among biologists in establishing causal links between high level biological phenomena (such as the phenotypes of a species) and some low level, but observable, entities (such as the genotypes of a set of genes). Similarly, systems neuroscience seeks to understand the relationship between an organism's behaviors and its neuronal circuitries. We may thus reasonably adapt Kirschner's statement for neuroscience, characterizing systems neuroscience as the study of the productions and organizations of behaviors in terms of the neuronal constituents.

This thesis concerns an important question in systems neuroscience, that of how the nervous system produces diverse, purposeful motor behaviors by appropriately specifying the neural commands for the activations of many muscles. From the perspective of a control engineer trying to build an intelligent robot capable of moving like a real animal, the problem of movement production turns out to be exceedingly difficult, to the extent that it is natural for the curious engineer to wonder how the central nervous system (CNS) achieves motor control with such flexibility and ease. A basic assumption of this thesis is that nature circumvents the difficulties of motor control (as perceived by us students of nature and engineering) by utilizing strategies that can simplify control. In particular, this thesis focuses on one such possible strategy – that of controlling multiple muscles together as a single unit of activation, or a muscle synergy – and how activations of muscle synergies can generate adaptive movements in a constantly changing external environment. In this introductory chapter, we shall first briefly describe some computational challenges associated with movement execution, and how muscle synergies can potentially alleviate the control difficulties posed by those challenges. Then, we will review some experimental evidence supporting the existence of muscle synergies, and some of the unresolved issues surrounding the conclusions of those experiments. Finally, we will present the goals of this thesis, and outline experiments that might provide insights into the nature of muscle synergies.

**The computational challenges of motor execution**

Many computational models of movement generation can be conveniently divided into two stages, motor planning and motor execution, each of which involves a series of coordinate transformations (Hogan, 1988). In the motor planning stage, a behavioral goal is first mapped to a trajectory of the limb endpoint capable of accomplishing that task goal. This endpoint trajectory, which may be simply represented in Cartesian coordinates with respect to some fixed reference point in the external space, needs to be further transformed into a time series of joint angles for every joint of the moving limb. This latter transformation, sometimes known as the inverse kinematics problem (Brady *et al.*, 1982), is necessary, because without joint angle information it is impossible to derive appropriate activation levels of the muscles, whose contractions are ultimately responsible for the joint motions effecting the endpoint movement.

The inverse kinematics transformation is already a difficult problem, because there are often many joint motion patterns consistent with any given endpoint trajectory, and it is not clear how the nervous system chooses one among the many alternatives. But suppose for now that through some additional constraints a desired joint motion is specified for every joint. The goal of the motor execution stage, then, is to transform this time series of joint angles to a set of neural commands for all muscles in the moving limb (and often, for the non-moving limbs as well) so that movement results.

How does the CNS specify the motor command for every muscle in the limb? To answer this question, an engineer might naturally think that before commands can be specified, the net torque needed to be exerted around each joint has to be computed first. Such a transformation from the joint kinematic trajectory to the torque profile has been called the inverse dynamics problem (whereas the prediction of kinematics from a given torque profile, the forward dynamics problem). Computing inverse dynamics essentially amounts to applying Newton's second law, $F=ma$, to a multi-articular system. However, solving the torque profile for each joint explicitly turns out to be a very computationally intensive procedure, given the large number of kinematic degrees of freedom in each limb, and also, the fact that in a system with multiple links, the motion of one link can produce torques at other links due to mere mechanical linkages (Hollerbach, 1982; Hollerbach and Flash, 1982). These torques, called interaction torques, can significantly complicate any analysis of limb dynamics, for the interaction forces around each joint can include a number

of components, including the inertial component (forces proportional to the acceleration of another joint), the Coriolis component (forces proportional to the product of the velocities of different joints), and the centripetal component (forces proportional to square of the velocity of another joint). To appreciate the complexity of inverse dynamics, it is worth restating here a set of equations given by Hollerbach and Flash (1982) relating the shoulder and elbow angles ($\theta_1$ and $\theta_2$) to the net torques required for those two joints ($\tau_1$ and $\tau_2$) in a much simplified model of the human arm with motions of only two joints confined to a horizontal plane:

$$\tau_2 = \ddot{\theta}_1(I_2 + \frac{m_2 l_1 l_2}{2}\cos\theta_2 + \frac{m_2 l_2^2}{4}) + \ddot{\theta}_2(I_2 + \frac{m_2 l_2^2}{4}) + \dot{\theta}_1^2(\frac{m_2 l_1 l_2}{2}\sin\theta_2),$$

$$\tau_1 = \ddot{\theta}_1(I_1 + I_2 + m_2 l_1 l_2\cos\theta_2 + \frac{m_1 l_1^2 + m_2 l_2^2}{4} + m_2 l_1^2) + \ddot{\theta}_2(I_2 + \frac{m_2 l_2^2}{4} + \frac{m_2 l_1 l_2}{2}\cos\theta_2) -$$
$$\dot{\theta}_2^2(\frac{m_2 l_1 l_2}{2}\sin\theta_2) - \dot{\theta}_1\dot{\theta}_2(m_2 l_1 l_2\sin\theta_2),$$

where $l_1$ and $l_2$ are lengths of the arm and forearm, $I_1$ and $I_2$ are the rotational inertia of the two limb segments, and $m_1$ and $m_2$ are the masses. As can be seen above, the equations for two degrees of kinematic freedom are already quite complicated. In fact, as derived by Jerard (1976), the dynamic equations for a more realistic model of the human arm with five degrees of freedom occupy two pages of closely packed text. Given such complexity of the limb dynamics, it is unclear how the CNS manages to handle so many differentiations and trigonometric operations simultaneously to arrive at an explicit solution of the required joint torques for many joints.

Moreover, the torques calculated by the above equations refer to the *net* torques required to move the joints along the desired trajectory. Given the redundancy of the muscular system, there are also many possible muscle activation patterns consistent with any profile of net joint torques. Again, it is unclear how the CNS chooses one particular pattern among many alternatives. An additional problem associated with solving inverse dynamics explicitly for motor control is that, it implicitly assumes that muscles are "ideal" actuators whose force outputs are independent of their lengths and velocities (Bizzi *et al.*, 1992), but it is well known that muscle force depends on its length, velocity, and activation level (e.g., see Brooks, 1986).

The difficulty in specifying muscle activations for a given desired trajectory can be understood in another way. Bernstein (1967) was probably the first who realized that any

movement resulting from the activation of any muscle or muscle groups depends critically on the context in which the movement is being performed. In Bernstein's words, "movements are not completely determined by effector processes," and thus, "motor effect of a central impulse cannot be decided [*a priori*] at the centre, but is decided entirely at the periphery" (1967 ed., pp. 105-106). One source of such indeterminacy between muscle activations and movements can be attributed entirely to anatomical factors. As a result of the particular insertion positions of a muscle, the movement produced by contracting the muscle is very often a function of the limb's configuration. For example, activating the muscle pectoralis major abducts the arm when the arm is raised above the shoulder joint's horizontal axis, but adducts the arm otherwise (Turvey *et al.*, 1982). Additionally, the movement effect resulting from contracting a muscle also depends on the state of the limb, that is, its position and velocity. An example of this source of indeterminacy is that activating the brachialis muscle when the elbow is at rest and extended leads to elbow flexion, but activating the same muscle, to the same degree, when the elbow is being extended from a flexed position may halt elbow motion instead (Turvey *et al.*, 1982). The above examples illustrate that the relationship between muscle activations and the resulting movement can be ambiguous, and such context-dependent variability of movement generation poses a significant challenge for the CNS to specify the activation level of each muscle appropriately.

The movement resulting from activating just one muscle can already be quite variable, as described above. But to generate a gracious movement, the CNS has to specify the activation of not just one, but many muscles the limb, and more importantly, to properly coordinate their activations. As recognized by Bernstein (1967), successful motor execution depends critically on motor coordination, which is "an activity which guarantees that a movement shall have (the) homogeneity, integration and structural unity … this activity is principally based not on particular processes in individual neurons, but on the determinate *organization* [*sic*] of their common activity" (1967 ed., p. 30). Given the large number of muscles present in the musculature representing a large number of degrees of freedom to be specified, it is difficult for students of systems neuroscience to fathom how the CNS achieves successful coordination. For one thing, with so many degrees of freedom any adjustment of motor commands for compensating systems noise or external perturbations becomes extremely difficult, because to ensure proper coordination, correcting the

command of any muscle might necessitate adjustments in the activations of all other muscles. Also, the number of available muscles far exceeds the minimal number necessary for executing a given task; hence, it is likely that for any task there are many possible combinations of muscle patterns capable of accomplishing the same trajectory. The CNS thus needs to cope with such redundancy by solving a problem with no unique solution. Thus, successful motor coordination is in essence "the process of mastering redundant degrees of freedom of the moving organ, in other words its conversion to a controllable system" (Bernstein, 1967, p. 127).

There remains a possibility that, all possible combinations of motor commands are stored somewhere in the CNS, and motor execution amounts to finding the best combination from a giant look-up table. But this possibility seems extremely unlikely to be biologically plausible, given the large number of muscles present in the musculature and the almost infinite number of activation states that each muscle may assume. This approach of computation obviously suffers from the "curse of dimensionality," a term coined by Bellman (1961) to describe the exponential increase in data points as the data dimensionality increases.

To summarize briefly, the complexity of solving the inverse dynamics problem explicitly, the context-dependent nature of the relationship between muscle activations and the resulting movement, and the large number of degrees of freedom in the muscular system all contribute to the seeming difficulty for the CNS to appropriately specify the muscle commands to achieve any motor behavior.

**Organizing motor outputs through muscle synergies as a simplifying control strategy**

Given the computational challenges of motor execution outlined above, it is therefore reasonable to expect that, the CNS adopts some simplifying control strategies that circumvent the complexity of explicitly solving the inverse dynamics problem, and also, alleviate the burden of coordinating many degrees of freedom in the musculoskeletal system. One such possible simplifying strategy is that, during motor execution, multiple muscles are activated together as a fixed group, or a muscle synergy, and the final motor patterns emerge from an organized combination of the activations of a small number of synergies, each potentially comprising different muscles (Greene, 1972; Kugler *et al.*, 1980; Lee, 1984; Macpherson, 1991). As a result of collapsing multiple degrees of freedom (i.e., multiple

muscles) into a single unit of activation, the number of degrees of freedom needed to be controlled is reduced. The muscle synergies, then, represent a set of low-level, neurally-encoded patterns that constrain the muscle patterns achievable (Lee, 1984).

Generating muscle patterns through a set of muscle synergies simplifies control, at least theoretically, in several ways. The most obvious advantage offered by synergies is that they reduce redundancy by constraining the set of all conceivable muscle patterns (Bernstein, 1967; Full and Koditschek, 1999). As pointed out earlier, in many animals redundancy exists at both the kinematic level (i.e., for any task, multiple joint trajectories are possible) and the actuator level (i.e., for any trajectory, multiple muscle patterns are possible). While synergies obviously reduce actuator redundancy, it is possible that they reduce kinematic redundancy as well by disallowing the muscle patterns necessary for some of the possible trajectories.

Secondly, by constraining a group of muscles to act as a unit, a synergy may serve to eliminate certain muscle patterns that lead to uncoordinated movements (Tuller *et al.*, 1982). This point is best illustrated with a hypothetical example given in Turvey *et al.* (1982). Suppose that there exists a four-wheel car in which the direction of each wheel has to be independently controlled, so that the driver has to attend to four steering wheels simultaneously. With such a car, the driver would have a difficult time controlling the car's direction and speed, because the directions of the four wheels have to match, and any slight deviation of direction in one steering wheel would necessitate adjustments in those of all other three wheels. But if the directions of the two front wheels are coupled, and those of the rear wheels, locked, so that the driver needs only to attend to one steering wheel, controlling the car's direction becomes much easier. Similarly, if each muscle is controlled independently, then any slight deviation in the activation of one muscle would demand fine-tuning the activations of all other muscles to prevent the emergence of uncoordinated movements. But if certain muscles are grouped together in a way that their co-activations would always compensate or assist each other to result in coordinated movement even if the synergy's activation is perturbed with noise, then the formidable task of coordinating the activations of many muscles is much simplified.

Thirdly, if each muscle synergy is composed in such a way that co-activations of the synergy's constituents always result in the execution of certain simple biomechanical functions, or movements with certain predictable features, then motor commands might be generated easily through specifications of the synergies' activation levels without the need to

explicitly solve the inverse dynamics equations. This idea is closely related to the proposal that, each synergy should ideally be a "self-regulatory entity" (Tuller *et al.*, 1982, p. 258) whose composition implicitly contains knowledge of the limb's dynamics. For example, a synergy may comprise both agonist muscles for producing certain movement around a joint, and other muscles for simultaneously counteracting the resulting interaction torques around other joints. Presumably, the specific biomechanical or kinematic functions performed by the synergies should be consistent with a minimal model of the behavior of the animal's body in pursuit of a goal (e.g., an inverted pendulum could serve as a minimal model of human postural control). Using the terminology of Full and Koditschek (1999), muscle synergies should ideally be the "anchors," or strategies of motor execution, that embed a "template" of the body, or the simplest possible model that describes the body's behavior during a motor behavior.

As a result of being structured to perform some simple biomechanical or kinematic functions, muscle synergies might also facilitate generalization of motor control (Poggio and Bizzi, 2004), in the sense that altering the activations of the same set of synergies might enable the animal to perform the same behavior in a very different dynamical environment (Mussa-Ivaldi, 1997), or a different behavior in the same environment (d'Avella *et al.*, 2003). In abstract terms, synergies may be regarded as structures that has been "learned" during the organism's evolutionary course (not in the Lamarckian sense, but in the sense of being the end result of natural selection), or, structures that permit generalization – that is to say, their flexible use can produce diverse adaptive motor behaviors.

In essence, specifying muscle commands through muscle synergies simplifies control because synergies can reduce the number of degrees of freedom, and can represent some pre-programmed combinations that automatically take care of some aspects of the system's dynamics. As a result, motor execution becomes much more robust and efficient, as the central executive of the CNS is not burdened by the details of how the movement should be implemented (Greene, 1972).

In the following section, we briefly review some experimental evidence supporting that motor command generation through combination of a small number of muscle synergies is a biologically plausible strategy of control simplification.

**Experimental evidence for muscle synergies**

As reviewed thoroughly in Tresch *et al.* (2002), there have been many experimental results, obtained from a variety of preparations using different techniques, suggesting that high-dimensional muscle commands could be generated by combining several muscle synergies. Here, we shall summarize the results of the few studies that are the most relevant to the goals of this thesis (to be described below).

One approach that has been pursued by a number of authors for demonstrating the existence of synergies involves recording electromyogram (EMG) data from many different muscles simultaneously during one or several behaviors. In these studies, a definition of muscle synergy is first given, and a model of how the synergies are combined, proposed; then, the EMG data are computer analyzed for finding the muscular compositions of a set of putative synergies according to the proposed model of synergy combination. The existence of synergies and the validity of the synergy model are then inferred from the result that only a small number of putative synergies is needed to explain most amount of variance in the EMG data.

In one of the first studies taking the approach described above, Tresch *et al.* (1999) recorded EMG data from 9 hindlimb muscles of the spinalized bullfrog during reflexive behaviors evoked by cutaneous stimulations. The EMG data of each muscle obtained from each reflex were then averaged to yield an EMG response vector across the 9 muscles for each reflex. In their synergy model, a muscle synergy is defined to be a non-negative (i.e., zero or positive) activation profile across all 9 muscles. Each reflex response is hypothesized to be generated by linearly combining several synergies, each of which is activated by a non-negative coefficient. Formally, the synergy model of Tresch *et al.* (1999) can be stated as follows:

$$\vec{m}_j = \sum_{i=1}^{N} c_{ij}\vec{w}_i, \quad c_{ij}, \vec{w}_i \geq 0, \tag{1.1}$$

where $\vec{m}_j$ is the observed EMG response vector of the *j*th reflex, $\vec{w}_i$ is the synergy vector of the *i*th muscle synergy, $N$ is the number of synergies, and $c_{ij}$ is the coefficient for the *i*th synergy during the *j*th reflex. Estimates of the synergy vectors and their corresponding coefficients were obtained by applying a least-squares gradient descent algorithm onto the set of all EMG responses. Tresch *et al.* found that, under the model described by eqn. 1.1, 4

synergies are sufficient for predicting the EMG responses with an $r^2$ of ~90%. These results are consistent with the idea that the CNS reduces the number of degrees of freedom (in this case, from 9 to 4) by coupling muscles together as synergies. Variability of the EMG responses is explained by the synergy coefficients, which vary across different reflexes.

In another study, Saltiel *et al.* (2001) recorded EMGs of 12 hindlimb muscles of the spinalized frog during responses elicited by intraspinal *N*-methyl-*D*-aspartate (NMDA) microstimulation. This approach of eliciting responses by focal chemical stimulation offers the potential advantage that, the synergies derived are more likely to represent some task-independent modules used for constructing a wide range of movements, as the EMGs were obtained by direct stimulation of spinal interneurons rather than during particular behaviors. Using the same model of synergy combination (eqn. 1.1), Saltiel *et al.* (2001) found that, 7 muscle synergies, also extracted from the EMGs using non-negative gradient descent, are sufficient to explain 91% of the EMG variance. These results suggest that there might be a small number of synergies, encoded within localizable regions of the spinal cord (see also Saltiel *et al.*, 2005), whose linear combination could be a mechanism for generating diverse motor outputs from the spinal cord.

Both of the studies summarized above test the synergy hypothesis by recording and analyzing EMGs of spinalized animals. While the use of spinalized preparations ensures that any synergy observed can be attributed to some low-level neural structures, whether the synergies obtained are indeed used for constructing natural behaviors has remained an open question. D'Avella (2000) extended the conclusions of those studies by recording EMGs of 13 hindlimb muscles during intact, natural behaviors of the bullfrog, including jumping, stepping, kicking, wiping, and swimming. The EMGs from these natural motor behaviors are much more variable than those from spinalized animals, and hence, d'Avella's study is a more stringent test of the generalizing power of muscle synergies across behaviors. Owing to the complexity of the EMGs collected, it is difficult to divide every EMG episode into discrete phases for obtaining averaged EMG values during each phase. Thus, in d'Avella (2000), every EMG data point (after pre-processing) is regarded as a EMG response. Specifically, the model of synergy combination can be stated as follows:

$$\vec{m}(t) = \sum_{i=1}^{N} c_i(t) \cdot \vec{w}_i, \quad c_i(t), \vec{w}_i \geq 0, \tag{1.2}$$

where $\vec{m}(t)$ represents the vector of EMG data at time *t*, and $c_i(t)$ is the time-varying scalar activation coefficient for the *i*th synergy. D'Avella showed that for each behavior, the EMG data set comprising signals from 13 muscles can be reconstructed by linearly combining only 5-7 synergies with $R^2$ values >90%. More important, some of the synergies extracted from the data sets of different behaviors are very similar to each other, suggesting that a subset of synergies are modules shared between different behaviors (see also, d'Avella and Bizzi, 2005). D'Avella's study provides direct evidence supporting the proposal that, the CNS organizes the motor outputs of diverse everyday motor behaviors by flexible combinations of a small number of fixed muscle synergies.

Existence of muscle synergies has been inferred by similar approaches of EMG analysis in many other preparations and behaviors, including brainstem behaviors of the bullfrog (Hart and Giszter, 2004), postural responses of the cat (Ting and Macpherson, 2005; Torres-Oviedo *et al.*, 2006), feline locomotion (Krouchev *et al.*, 2006), monkey grasping and reaching (Overduin, 2006), human locomotion (Ivanenko *et al.*, 2004; Cappellini *et al.*, 2006), human arm movements (Sabatini, 2002; d'Avella *et al.*, 2006), human standing postural responses (Krishnamoorthy *et al.*, 2003), and human hand postural responses (Weiss and Flanders, 2004).

**Definitions of muscle synergy**

Before stating the goals of the present thesis, it is worth distinguishing the several different meanings that have been associated with the word 'synergy' in the motor control literature. In this thesis, the term synergy refers to the concept of muscle synergy, or a grouping of muscle activities. This usage differs from that used for describing some invariant kinematic features (e.g., the "kinematic synergy" of Freitas *et al.*, 2006). However, in the literature there are also several definitions or formulations of muscle synergy. We list several of them below, and discuss their respective strengths and limitations.

(1) In many textbooks (e.g., Kandel *et al.*, 2000) and articles, two muscles with similar functions are referred to as 'synergist' muscles, and those with opposing functions, 'antagonist' muscles. For instance, in the human leg, soleus is a synergist of gastrocnemius, while anterior tibialis, an 'antagonist.' While simple, this usage can potentially lead to much confusion in studies involving many muscles, because often a multiarticular muscle possesses several distinct functions. For example, the frog

semitendinosus is both a hip extensor and a knee flexor. Also, two muscles with different functions can conceivably be co-activated as a functional unit, and this definition of a 'synergy' is clearly inadequate for our purposes.

(2) In a number of studies (e.g., Smith *et al.*, 1985), muscles that appear to be co-activated together during a behavior are grouped under the same muscle synergy. Importantly, under this definition, each muscle belongs only to one synergy. Recently, such a definition has been adopted by Krouchev *et al.* (2006) in an analysis of feline locomotor patterns. They define a synergy as "comprising a group of muscles that are temporally co-activated and the period of activity of which begins and ends synchronously" (p. 1992). To identify synergies objectively, Krouchev *et al.* then proceeded to develop a new clustering algorithm which detects synergies based only on the onset and offset times of the EMG bursts. As acknowledged by the authors, this definition may result in synergies whose activation patterns are more physiologically plausible. However, since only the onset and offset times of the EMG bursts are used to define a synergy, information contained within the actual waveforms of the EMG bursts are not incorporated into the structures of the extracted synergies. Also, as compared with other definitions [e.g., definition (3) below], this definition appears to require more number of synergies to describe the EMG data (see Krouchev *et al.*, 2006, their Figs. 5 & 8C).

(3) Some investigators have extracted synergies from multi-channel EMG data using either principal component analysis (PCA) (Jolliffe, 2002; Krishnamoorthy *et al.*, 2003; Weiss and Flanders, 2004; Shemmell *et al.*, 2005) or independent component analysis (ICA) (Bell and Sejnowski, 1995; Hyvärinen and Oja, 2000; Kargo and Nitz, 2003; Hart and Giszter, 2004). These algorithms require a synergy to be defined as an activation balance profile across all recorded muscles, and the muscle data are then explained as linear combinations of several synergies. Thus, under this definition, a muscle can belong to more than one synergy. This model of EMG generation is almost the same as that specified by eqn. 1.2, except that neither the synergy components nor their activation coefficients are constrained to be non-negative. A real strength of this definition of synergy is that, the positive and negative muscle components of a synergy could be respectively interpreted as the excitatory and inhibitory synapses between the synergy-coding interneurons and the motoneurons. In addition, the assumption of the ICA algorithm that the activation coefficients of the different synergies are statistically

independent corresponds very nicely to the notion that an ideal module should be an "autonomous" process (Schlosser, 2004). However, in a study using simulated data sets (Tresch *et al.*, 2006), the performance of PCA has been shown to be generally poorer than other algorithms; in data sets corrupted by signal-dependent noise, ICA's performance was also much impaired. More important, because the signs of the synergy components are unconstrained, the EMG data (especially those data points with near-zero magnitude) can at times be explained as the positive components of one synergy canceling out the negative components of another. Consequently, the synergies extracted by PCA or ICA tend to be holistic (i.e., non-zero activation components are present in most of the recorded muscles), and thus, less physiologically interpretable.

(4) Latash and colleagues distinguish two different concepts related to multi-muscle units in the context of the uncontrolled manifold (UCM) hypothesis, which posits that the CNS selectively limits the variability of certain control variables whose fluctuations could lead to instability in a performance variable (Scholz and Schöner, 1999). According to Krishnamoorthy *et al.* (2003), in UCM analyses, 'synergies' should specifically be "task-specific groups of elements that stabilize particular performance variables" (p. 152). Depending on the level of analysis, groupings of muscles, motor units, or even neurons could potentially be called synergies so long as stabilization of a performance variable could be achieved by their co-activations. At the same time, the large number of muscles in the muscular system implies that many muscles are likely to be controlled together as a unit. This necessitates the formulation of another concept, that of the 'muscle modes,' or 'M-modes,' which "represent [hypothetical] multimuscle units that decrease the number of control variables manipulated by the controller, but they are not specific to a particular performance variable" (p. 158). These definitions have the merit of being very precise. But in experimental settings in which the nature of the most behaviorally relevant performance variables is not clear in the first place, it could be difficult to ascertain whether an observed muscle grouping is a synergy or an M-mode.

(5) All four definitions of synergy described above conceptualize a synergy as a synchronous, time-invariant unit of activation. But inspections of the EMGs of many behaviors often reveal fixed relationships between the activation timings of several muscles, and thus, a synergy may be defined not only in the spatial domain as an activation profile across muscles, but also in the temporal domain as an invariant

sequence of EMG bursts of different muscles. This concept of 'time-varying muscle synergy' (d'Avella and Tresch, 2002; d'Avella *et al.*, 2003; d'Avella *et al.*, 2006) can be formally stated as follows:

$$\vec{m}(t) = \sum_{i=1}^{N} c_i \vec{w}_i(t - t_i), \qquad \vec{w}_i(\tau) = 0 \text{ if } \tau < 0 \text{ or } \tau > T, \tag{1.3}$$

where $\vec{w}_i(\tau)$ denotes the *i*th synergy specifying an activation profile for all recorded muscles for every time point, τ, that falls within a time window of duration *T*. Each time-varying synergy is activated by a scalar, $c_i$, and time-shifted by another scalar, $t_i$. As demonstrated by d'Avella *et al.* (2006, their Fig. 16), such a synergy model can potentially represent high-dimensional EMG data with a smaller number of parameters than any model of synchronous synergies. The trade-off's for this reduction of parameters are that the EMGs tend to be described less well (i.e., with lower $R^2$ values), and that the computational resource required for extracting synergies tends to be larger.

(6) In this thesis, the definition of muscle synergy adopted is similar to that used in d'Avella (2000), Saltiel *et al.* (2001), and Ting and Macpherson (2005). Each muscle synergy is represented as a synchronous, time-invariant activation balance profile across all recorded muscles, so that each muscle can potentially belong to more than one synergy. Furthermore, all components of every synergy are assumed to be non-negative. Each synergy is activated by a time-varying, non-negative activation coefficients, and the final EMG output is generated by linearly combining several synergies, each of which is weighted by their respective time-varying coefficients. Eqn. 1.2 is a formal mathematical statement of the synergy model used in this thesis.

This formulation of synergy combination is a reasonable choice of model for analyzing EMGs of natural behaviors for the following reasons. Firstly, the fact that every muscle can potentially belong to multiple synergies corresponds well with the finding that the motoneuronal pool of every muscle is activated by many interneuonal groups (Jankowska, 1992; and in particular, see Sugiuchi *et al.*, 2004), each of which could represent a muscle synergy. Secondly, the linearity assumption is justified by the conclusion of a recent simulation study that, the musculo-tendon's capacity to generate forces that scale linearly with its activation could be a biomechanical result of the operating range of the musculo-tendon's length (Berniker, 2005). Thirdly, non-negative synergies can be easily

extracted from the EMG data using the non-negative matrix factorization (NMF) algorithm (Lee and Seung, 1999, 2001). As a result of the non-negativity constraints, the extracted synergies tend to be sparse (i.e., only a few of all muscles have non-trivial activation components in a synergy) rather than holistic, and therefore, more physiologically interpretable. Finally, as will be shown in chapters 3-4, the multiplicative update rules of the NMF algorithm allows simultaneous extraction of synergies shared between multiple data sets, as well as synergies specific to one or several data sets. This unique property of the NMF update rules facilitates comparison of synergies extracted from different conditions, allowing any hypothesis of synergy sharing to be evaluated more easily.

Of course, this synergy model is not without limitations. It does not capture any potential inhibitory synapses between interneurons and the motoneuronal pools, and any fixed temporal relationships between EMG bursts are not captured by the synergies. A thorough, rigorous comparison between the different definitions of muscle synergy outlined above is beyond the scope of the present thesis.

**Goals of the thesis, and an abstract of my argument**

As briefly reviewed above, evidence for the existence of muscle synergies has been provided by the frog experiments of Tresch *et al.* (1999), Saltiel *et al.* (2001), d'Avella (2000), and also, other studies focusing on a variety of preparations. However, a number of unresolved issues pertaining to those studies have remained, some of which cast doubt on whether the observed synergies represent constraints utilized by the CNS for simplifying movement control.

Firstly, in the aforementioned studies, synergies were extracted from the EMG data using a decomposition algorithm such as the NMF algorithm (e.g., d'Avella, 2000; Ting and Macpherson, 2005). Even though the EMG data are described well by the extracted synergies ($R^2 \approx 90\%$), it is conceivable that, the extracted synergies are merely artifactual structures resulting from the constraints and assumptions imposed by the algorithm used. In other words, if we regard the algorithm as a model of EMG generation imposed onto the data, it is uncertain whether the algorithm is a good enough 'synergy-recognition model' whose assumptions should ideally match those of the 'generative model' thought to underlie the process of synergy combination (Dayan and Abbott, 2001, pp. 359-60).

Secondly, it could be argued that the observed synergies in the aforementioned studies only reflect experimental constrains instead of neural constraints for control simplification – that is to say, under those experimental conditions, the EMGs could only be configured in a limited way to achieve the observed behaviors, and thus, the observed synergies could just be an epiphenomenon due to constraints like the biomechanical requirements of the tasks, the specific dynamic environments, or the specific afferent inflow pattern during the behaviors. This concept of neural versus experimental constraints is best illustrated using Venn diagrams.[1] Shown in each panel of Fig. 1.1 are two axes denoting the space of all conceivable muscle patterns. The area delimited by circle *B* represents the set of muscle patterns capable of executing a particular behavior, and that delimited by circle *N*, the set of patterns that can be produced by the nervous system. The experimentally observed muscle patterns are then denoted by the intersection of circles *B* and *N*, colored gray in the figure. As shown in panels A1 and B1 in Fig. 1.1, in the synergy studies mentioned above, the observed 'synergies' can either be due to stringent neural constraints within a large set of possible muscle patterns consistent with the behaviors (panel A1), or, stringent experimental constraints within a large *N* set resulting from each muscle being controlled individually (panel B1). Clearly, only the former of these two scenarios (panel A1) are consistent with the notion that, muscle synergies function as neural constraints for control simplification.

This thesis seeks to shed light on the open questions described above, with the primary goal of testing the hypothesis that, the nervous system simplifies motor control by generating muscle commands through combinations of a small set of muscle synergies, conceptualized as robust neural patterns that constrain motor outputs (Fig. 1.1, panel A1) (Lee, 1984). I first addressed the question concerning the need to use an appropriate synergy identification algorithm by analyzing the non-negative matrix factorization (NMF) algorithm, first proposed by Lee and Seung (1999), and used in a number of studies to extract synergies (e.g., d'Avella, 2000; Torres-Oviedo *et al.*, 2006). In chapter 2, I show that this algorithm, originally formulated as a procedure of estimating synergy vectors through minimization of the data reconstruction error (Lee and Seung, 2001), can be reinterpreted as a procedure of searching for synergies that maximize the likelihood of observing the data set, assuming that the data set is corrupted by a constant-variance Gaussian noise. I further demonstrate that,

[1] I thank Yue Tan David TANG for this suggestion.

the NMF can be rearranged to model other noise distributions, and in particular, the gamma distribution. Using both the Gaussian and gamma versions of the NMF, I then performed simulation experiments whose results suggest that, when the data noise magnitude is low, both versions of the NMF algorithm perform identically. More importantly, when applied to real EMG data sets obtained from frog natural behaviors, both versions of the NMF yielded similar synergies. These results suggest that the noise magnitude of the EMG data is likely to be low, and thus, the NMF seems to be a reasonable synergy extraction algorithm, at least for EMG data sets obtained from frog natural behaviors.

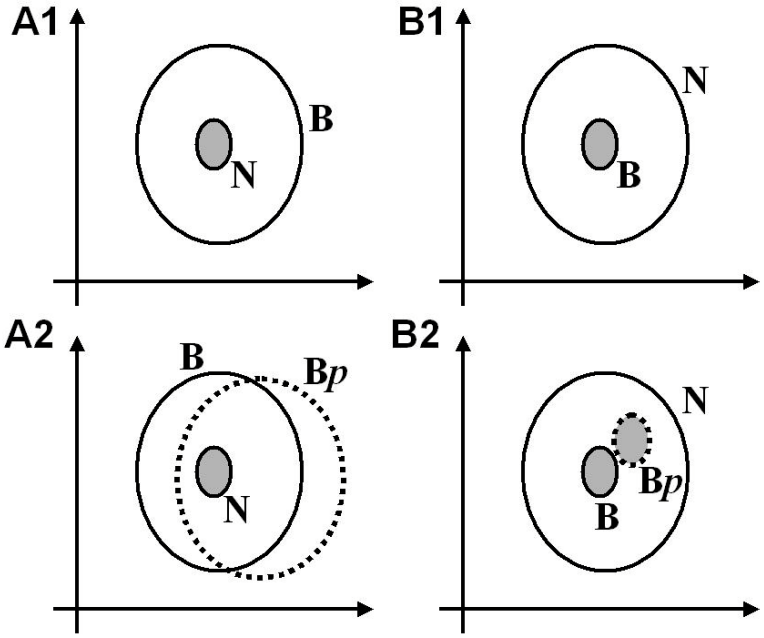


**FIGURE 1.1.** Venn diagrams illustrating the goals of the perturbation experiments described in this thesis. In each panel, the two axes denote the space of all conceivable muscle patterns (i.e., patterns of EMG activity). The circle *N* delimits the set of patterns that can be produced by the nervous system, and the circle *B*, the set capable of executing a motor behavior under a particular experimental condition. The observed EMG patterns are then necessarily bounded by the interaction of circles *N* and *B*, colored gray in the figure. In previous studies, the experimentally observed muscle synergies can either be attributed to stringent neural constraints (*A1*), or to tight experimental constraints (*B1*). To distinguish these two possibilities, the experimental conditions can be perturbed (circle B*p*). Scenario *A1* predicts that after perturbation, the synergies remain the same (*A2*). Scenario *B1*, on the other hand, predicts that synergies are changed after perturbation (*B2*).

Concerning the second question of whether synergies are indeed a set of neural constraints, I sought to distinguish the two possibilities illustrated in panels A1 and B1 of Fig. 1.1 by means of perturbation experiments. More specifically, I recorded EMG patterns

from the right hindlimb of the bullfrog (*Rana catesbeiana*) during natural motor behaviors, before and after delivery of a perturbation to the frog's motor system. This perturbation is expected to alter the original experimental constraints (Fig. 1.1, circles B*p* in panels A2 & B2), thus allowing the two possibilities (Fig. 1.1, panels A1 *vs* B1) to be distinguished. If the observed muscle synergies do represent neural constraints, then the synergies are expected to remain unchanged after perturbation (Fig. 1.1, panel A2). On the other hand, if the synergies observed in earlier studies are merely reflections of experimental constraints, then the original 'synergies' observed before perturbation are not expected to remain invariant after perturbation delivery, as the new experimental constraints (B*p* in panel B2) would necessitate some new muscle activation patterns for production of the same behavior.

Two chapters in this thesis are devoted to such perturbation experiments. In chapter 3, I describe a set of experiments designed to test whether muscle synergies underlying locomotor behaviors rely on sensory signals for their organizations. Muscle signals from 13 hindlimb muscles were recorded during jumping and swimming before and after ipsilateral hindlimb deafferentation, the surgical procedure of removing sensory inflow into the CNS by severing the dorsal nerve roots. I then compared intact and deafferented synergies systematically using a novel reformulation of the NMF capable of simultaneously extracting synergies shared between the two data sets, as well as synergies specific to each data set. My analytical results demonstrate that most of the locomotor synergies remained invariant after deafferentation, suggesting that the observed synergies are robust neural structures encoded within spinal and/or supraspinal networks.

In chapter 4, I present results of a set of experiments in which the dynamics of the frog hindlimb was perturbed by both inertial loading and elastic loading. Muscle signals were collected during jumping, swimming, kicking, and stepping before, during, and after loading. Then, the EMGs of the different unloaded and loaded conditions were systematically analyzed using another novel algorithm capable of extracting synergies from the pooled data set comprising EMGs of all conditions, and for each extracted synergy, indicating in which condition(s) that particular synergy was activated. Most of the extracted synergies were activated in all unloaded and loaded conditions, suggesting that most muscle synergies are robust structures independent of the particular sensory stimuli engendered during a specific condition. But the activation pattern of several invariant synergies was

reversibly changed by loading, indicating that the motor system may adapt to a new dynamic environment by modulating the activations of a fixed set of synergies.

Overall, the robustness of the synergies observed in my perturbation experiments argues for the case that, the muscle synergies extracted from the EMG data reflect neural structures that constrain motor outputs during natural motor behaviors. At the same time, both descending signals and sensory stimuli cooperate in modulating the activations of synergies, so that the resulting motor commands can be efficiently adapted to the changing external environment.

*Chapter 2*

# A statistical interpretation of the non-negative matrix factorization algorithm[§]

[§] This thesis chapter is a revision of a previously published article:
Cheung VCK, Tresch MC (2005) Non-negative matrix factorization algorithms modeling noise distributions within the exponential family. *Proc. IEEE Eng. Med. Biol. 27th annl. conf.* (Shanghai, China, Sept 1-4, 2005), 4990-4993. 

## INTRODUCTION

In many experimental contexts, investigators are faced with highly complex and high dimensional data. Often, this complexity is only apparent, and the data in fact exist in a simpler, low dimensional subspace of the total possible dimensionality. The problem for the investigator is to identify a representation of the data which captures this low dimensional subspace, thereby characterizing the critical features of the observed data.

Many methods have been proposed to perform this subspace identification, or matrix factorization. Here we describe a general framework for the factorization of data sets consisting of non-negative data. This work extends the framework developed by Lee and Seung (1999, 2001), to non-negative data sets generated according to any of the probability distributions belonging to the exponential family. This approach allows us to develop factorization algorithms which can be adapted to data sets with different expected statistical properties. We illustrate this approach using a factorization algorithm based on generalized gamma distributions, for which the standard deviation of a data point is proportional to its mean. Such signal dependent noise is expected for many physiological data sets, such as muscle activation patterns (Harris and Wolpert, 1998).

## ALGORITHM DERIVATION

Let $D$ be a non-negative $M \times T$ data matrix comprising $T$ samples of a $M$-dimensional data vector. We model the data matrix as a linear combination of $N$ basis vectors, $N \leq M$, such that

$$D \approx W \bullet C; \quad D,W,C \geq 0; \tag{2.1}$$

where each column of $W$ ($M \times N$) represents a basis vector, and each row of $C$ ($N \times T$) represents the coefficients for a corresponding basis across all data samples. We further assume that the observed $D$ is generated by corrupting $W \bullet C$ with noise that can be characterized as a distribution in the exponential family. Our problem is to estimate $W$ and $C$ given $D$.

In the noise model pursued here, each observed data sample from each channel, $D_{ij}\,(i = 1...M,\, j = 1...T)$, is a random variable whose distribution is described by one in the

exponential family; the mean of the distribution for each data point is then equated to the uncorrupted data point generated by linearly combining the basis vectors, i.e., $[WC]_{ij}$. Suppose that the distribution involves $P$ parameters, $\theta_1,...,\theta_P$. We first assume that one of the parameters (say, $\theta_1$, without loss of generality) can be related to the mean of the distribution, denoted by $\mu$, through a link function, $g$, such that

$$\theta_1 = g(\mu, \theta_2, \theta_3, ..., \theta_P). \tag{2.2}$$

If we further assume that the data samples and the data dimensions are both independently distributed, the likelihood function for $D$ can be expressed as follows for any noise distribution in the exponential family:

$$P(D \mid \vec{\mu}, \theta_2, ..., \theta_P) = \prod_{i=1}^{M}\prod_{j=1}^{T} h(D_{ij}) y\left(g(\mu_{ij}, \theta_2, ..., \theta_P), \theta_2, ..., \theta_P\right) \exp\left(\sum_{q=1}^{K} z_q\left(g(\mu_{ij}, \theta_2, ..., \theta_P), \theta_2, ..., \theta_P\right) \bullet t_q(D_{ij})\right), \tag{2.3}$$

where $h$, $y \geq 0$, $t_q$ , $z_q$ , $h$, $y$ are real-valued functions, and $K$ an integer, which together characterize a particular distribution in the exponential family; $\mu_{ij}$ is the distribution mean for data sample $D_{ij}$, and $\vec{\mu}$ is the set of all $\mu_{ij}$'s. To simplify equation (2.3), denote $\theta_2,...,\theta_P$ by $\bar{\theta}$, $y\left(g(\mu_{ij}, \theta_2, ..., \theta_P), \theta_2, ..., \theta_P\right)$ by $\bar{y}(\mu_{ij} \mid \bar{\theta})$, and $z_q\left(g(\mu_{ij}, \theta_2, ..., \theta_P), \theta_2, ..., \theta_P\right)$ by $\bar{z}_q(\mu_{ij} \mid \bar{\theta})$. Then, setting the distribution mean to be $W \bullet C$ yields the following expression relating the basis vectors and their coefficients to the likelihood function:

$$P(D \mid W, C, \bar{\theta}) = \prod_{i=1}^{M}\prod_{j=1}^{T} h(D_{ij}) \bar{y}(\sum_{a=1}^{N} W_{ia} C_{aj} \mid \bar{\theta}) \exp\left(\sum_{q=1}^{K} \bar{z}_q(\sum_{a=1}^{N} W_{ia} C_{aj} \mid \bar{\theta}) \cdot t_q(D_{ij})\right). \tag{2.4}$$

We estimate $W$ and $C$ through maximization of the log-likelihood function stated in equation (2.4). To accomplish this, we first differentiate $\log P(D \mid W, C)$ with respect to each component of the basis vector matrix, $W_{\bar{i}\bar{a}}, \bar{i} = 1...M, \bar{a} = 1...N$:

$$\frac{\partial}{\partial W_{\bar{i}\bar{a}}} \log P = \sum_{j=1}^{T} \frac{\bar{y}'(\sum_{a=1}^{N} W_{\bar{i}a} C_{aj} \mid \bar{\theta})}{\bar{y}(\sum_{a=1}^{N} W_{\bar{i}a} C_{aj} \mid \bar{\theta})} \cdot C_{\bar{a}j} + \sum_{j=1}^{T}\left(\sum_{q=1}^{K} \bar{z}_q'(\sum_{a=1}^{N} W_{\bar{i}a} C_{aj} \mid \bar{\theta}) \cdot t_q(D_{\bar{i}j})\right) \cdot C_{\bar{a}j},$$

$$= -\sum_{j=1}^{T} \Psi_{\bar{i}j} C_{\bar{a}j} + \sum_{j=1}^{T} \Phi_{\bar{i}j} C_{\bar{a}j} = [\Phi C^T]_{\bar{i}\bar{a}} - [\Psi C^T]_{\bar{i}\bar{a}}, \tag{2.5}$$

where

$$\Phi_{ij} = \sum_{q=1}^{K} t_q(D_{ij}) \bullet \bar{z}_q{}'([WC]_{ij} \mid \bar{\theta}); \qquad \Psi_{ij} = \frac{-\bar{y}'([WC]_{ij} \mid \bar{\theta})}{\bar{y}([WC]_{ij} \mid \bar{\theta})}. \tag{2.6}$$

Similarly, the partial derivative of the log-likelihood function with respect to each component of the coefficient matrix, $C_{\bar{a}\bar{j}}, \bar{a} = 1...N, \bar{j} = 1...T$, is as follows:

$$\frac{\partial}{\partial C_{\bar{a}\bar{j}}} \log P = [W^T \Phi]_{\bar{a}\bar{j}} - [W^T \Psi]_{\bar{a}\bar{j}}. \tag{2.7}$$

After obtaining the partial derivatives, the log-likelihood function can then be maximized through a 2-step iterative gradient ascent procedure. In the first step, $W$ is updated while keeping $C$ fixed; in the second step, $C$ is updated while keeping $W$ fixed. Denoting the learning rates of the first and second steps by $\eta^W$ and $\eta^C$, respectively, we obtain the following additive update rules (for the sake of clarity, the bars of every matrix subscript will be dropped in all ensuing equations):

$$\begin{aligned} W_{ia} &\leftarrow W_{ia} + \eta^W \bullet \frac{\partial}{\partial W_{ia}} \log P(D \mid W, C, \bar{\theta}), \quad \eta^W \geq 0; \\ C_{aj} &\leftarrow C_{aj} + \eta^C \bullet \frac{\partial}{\partial C_{aj}} \log P(D \mid W, C, \bar{\theta}), \quad \eta^C \geq 0. \end{aligned} \tag{2.8}$$

Since $W$ and $C$ are assumed to be non-negative, both of the above learning rates can be formulated component-wise as functions of $W$ and $C$. Let $\eta_{ia}^W = W_{ia} / [\Psi C^T]_{ia}$, and $\eta_{aj}^C = C_{aj} / [W^T \Psi]_{aj}$. After some straight-forward rearranging using the expressions in equations (2.5) and (2.7), the additive update rules in (2.8) can be reformulated as multiplicative update rules:

$$W_{ia} \leftarrow W_{ia} \bullet \frac{[\Phi C^T]_{ia}}{[\Psi C^T]_{ia}}; \quad C_{aj} \leftarrow C_{aj} \bullet \frac{[W^T \Phi]_{aj}}{[W^T \Psi]_{aj}}, \tag{2.9}$$

with the $\Phi$ and $\Psi$ matrices as defined in (2.6).

In this paper, we focus on two non-negative algorithms, derived using (2.9) from the Gaussian and the generalized gamma distributions, respectively. In the Gaussian case, if we set $\mu = WC$, then $\Phi = D / \sigma^2$, and $\Psi = [WC] / \sigma^2$. Substituting these expressions for $\Phi$ and $\Psi$ into (2.9), we obtain the update rules for the Gaussian algorithm (GAU), which are the same as the non-negative matrix factorization update rules proposed by Lee and Seung (1999, 2001).

To model signal-dependent noise, we use the generalized gamma distribution having the following form:

$$f(D_{ij} \mid \alpha, \kappa) = \left(\frac{D_{ij}\alpha}{\kappa}\right)^{\alpha} \frac{e^{-D_{ij}(\alpha/\kappa)}}{D_{ij}\Gamma(\alpha)}, \tag{2.10}$$

where $\alpha$ and $\kappa$ are parameters for the distribution, and $\Gamma(\alpha)$ is the gamma function. The distribution mean for (2.10) equals $\kappa$,[#] and hence, to obtain the non-negative matrix factorization update rules for this distribution, we can set $\kappa = [WC]_{ij}$. Let $\phi = 1/\sqrt{\alpha}$, we obtain the following relationship between the mean and standard deviation of each data point:

$$E(D_{ij}) = [WC]_{ij}; \quad Var(D_{ij}) = [WC]_{ij}^2/\alpha = \left(\phi \bullet E(D_{ij})\right)^2. \tag{2.11}$$

Thus, the generalized gamma distribution defines a signal-dependent noise model in which the standard deviation of the noise is proportional to the data amplitude. Such signal-dependent noise has been observed to underlie variation of control signals in the motor system (Harris and Wolpert, 1998). Update rules for the generalized gamma algorithm (GGM) can be obtained by deriving expressions for $\Phi$ and $\Psi$:

$$\Phi_{ij} = \frac{\alpha D_{ij}}{[WC]_{ij}^2}; \quad \Psi_{ij} = \frac{\alpha}{[WC]_{ij}}; \quad \alpha, W, C > 0; \tag{2.12}$$

and the noise proportionality constant $\phi$ in (2.11) can be obtained by estimating $\alpha$ using standard maximum likelihood methods.

## ASSESSING ALGORITHM PERFORMANCE

We assessed the ability of the GAU and GGM algorithms described above to identify underlying basis vectors from simulated data sets generated by known bases. Ten different simulated data sets were initially generated. Each contained 1000 data samples, and was generated by linearly combining a set of 5 basis vectors. The components of both the basis vector matrix ($W$) and the coefficient matrix ($C$) used for data generation were uniformly distributed in (0, 1). Each of these 10 data sets was then corrupted by two

[#] Note that the generalized gamma distribution stated in equation (2.10) can be viewed as a reparametrization of the standard gamma distribution using the link function $\beta = g(E(D),\alpha) = \kappa/\alpha$.

different types of noise – Gaussian noise, and signal-dependent noise with a generalized gamma distribution. In the case of Gaussian noise, the data set, $D$, was corrupted so that

$$D = g(\overline{D}); \quad \overline{D} \sim N(W \bullet C, \sigma^2),$$

where $g(x) = x$ if $x \geq 0$, and $g(x) = 0$ if $x < 0$. Such thresholding of the data was necessary to ensure that the simulated data set stayed non-negative. Each simulated data set was corrupted by Gaussian noise of 8 different magnitudes, corresponding to the following values of $\sigma$: (0.01, 0.02, 0.05, 0.1, 0.15, 0.2, 0.25, 0.3). In the case of signal-dependent noise, each of the 10 data sets was corrupted so that

$$D \sim Gamma \quad (\alpha, W \bullet C/\alpha).$$

As in the case of Gaussian noise, each of the 10 original simulated data set was corrupted by noise of 8 different magnitudes using the following values of $\alpha$: (20, 40, 60, 80, 100, 120, 150, 300). Thus, there was a total of 10×2×8 = 160 data sets, 80 of which contained Gaussian noise, and the other 80, signal-dependent noise.

For each type of noise, and for each noise level, we quantified noise magnitude by calculating $1\text{-}R^2$, where $R^2$ is the coefficient of determination representing the percentage of variance in the noise-corrupted data set explicable by the original uncorrupted data set.

We then proceeded to extract 5 basis vectors from each of these 160 data sets using both the GAU and GGM algorithms. For each extraction, we also randomly and independently shuffled each row of the data matrix, and extracted basis vectors from this shuffled data set. This allowed us to assess the baseline similarity between the extracted and original basis vectors (see below).

Performance of the two algorithms was assessed by comparing the extracted bases and the original bases generating the simulated data set. Similarity was quantified by calculating the sum of the cosine of the principal angles between the two sets of bases (Golub and Van Loan, 1983). Since 5 bases were identified in each extraction, the maximum similarity value was 5. To account for the possibility that a fraction of the calculated similarity value is expected by chance, for each data set, each noise magnitude, and each algorithm, the normalized similarity ($s^{norm}$) was calculated as follows:

$$s^{norm} = (s - s^{baseline})/(5 - s^{baseline}),$$

where $s$ is the similarity value between the original bases and the bases extracted from unshuffled data, and $s^{baseline}$ is the similarity value between the original bases and those extracted from shuffled data.

Figure 2.1 summarizes the performance of the two algorithms in the two types of noise-corrupted data sets. Results from both the GAU algorithm (solid line) and the GGM algorithm (dotted line) are presented (mean ± SD, $n$ =10). It is apparent from Fig. 2.1A that for data sets with Gaussian noise, when the noise magnitude was low, both algorithms performed equally well (with $s^{norm}$ close to 1). But for Gaussian noise magnitudes >20%, the GAU algorithm performed substantially better than the GGM algorithm. On the other hand, as shown in Fig. 2.1B, for data sets containing signal-dependent noise, the GGM algorithm performed better than the GAU algorithm for all noise magnitudes tested. Thus, the non-negative algorithm is better able to recover the original generative basis vectors if the actual noise structure of the data set agrees with the noise structure assumed by the algorithm.

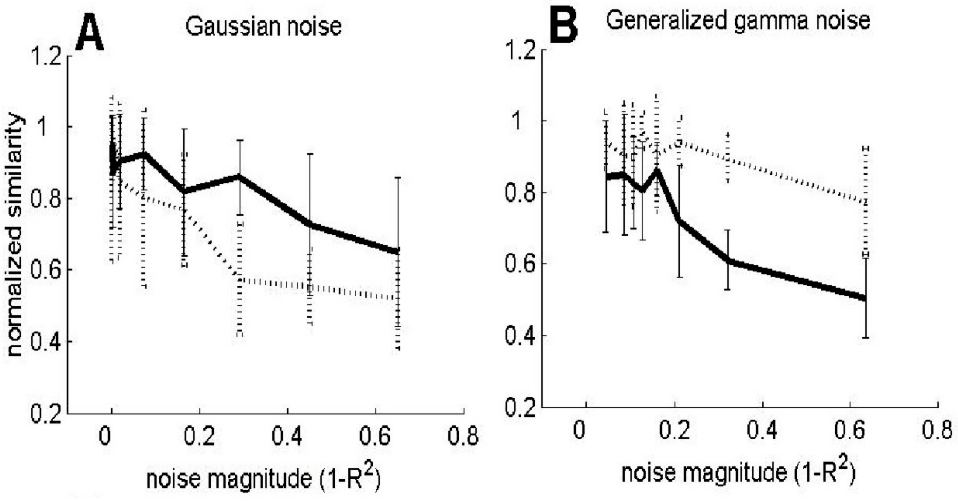


**FIGURE 2.1**. Assessing performance of the GAU and GGM algorithms with simulated data sets. Basis vectors extracted using the GAU algorithm (solid line) and GGM algorithm (dotted line) were compared with the original basis vectors generating the data sets. Data sets were corrupted by either constant variance Gaussian noise (*A*) or signal-dependent noise (*B*). Mean ± SD plotted ($n$=10).

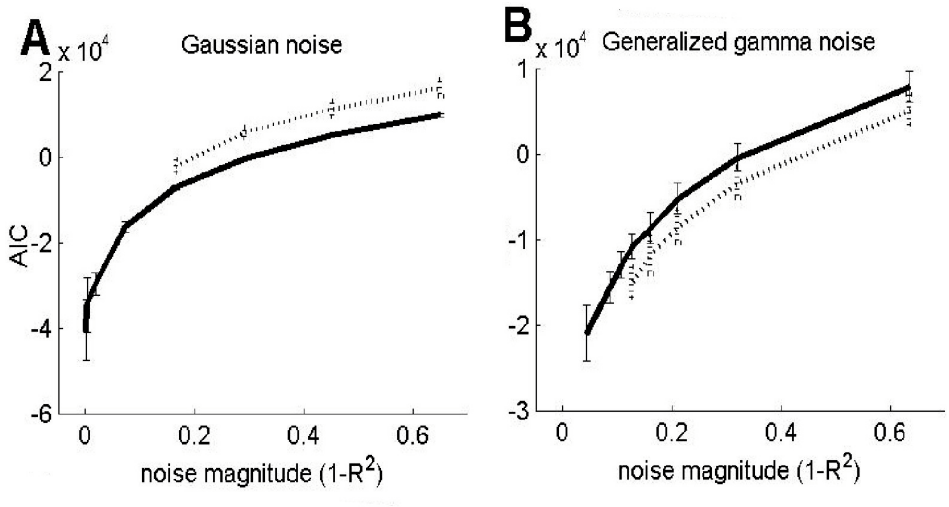


**FIGURE 2.2.** Testing the performance of the Akaike Information Criterion. The AIC values were computed using results obtained from both the GAU (solid line) and GGM (dotted line) algorithms. The simulated data sets were corrupted by either constant variance Gaussian noise (*A*) or signal-dependent noise (*B*). Note that for data sets with low noise magnitudes, we were unable to obtain the AIC values for the signal-dependent noise model, because the gamma function in Matlab cannot handle large input arguments. Mean ± SD plotted ($n$=10).

## MODEL SELECTION CRITERION – THE AIC

As shown above, the closer the data noise structure is to the noise structure assumed by the algorithm, the better the algorithm performs in retrieving the correct basis vectors. However, the noise structure of any given physiological data set is often not known. Whether results of any one algorithm are potentially "better" or "worse" than those of another in capturing underlying data structures has to be determined by some model selection criteria. Here, we tested whether the well-known Akaike Information Criterion (AIC) (Akaike, 1973) could reveal the underlying data noise structure in the simulated data sets described above: the lower the AIC, the better the fit of the parameters to the observed data.

For each of the 160 simulated data sets described in the previous section, the AIC was computed for both the GAU and GGM algorithms using their respective extracted bases and coefficients. Figure 2.2 shows the AIC values obtained from the two algorithms (GAU: solid line; GGM: dotted line; mean ± SD, $n$ =10). It is apparent that for data sets corrupted with constant-variance Gaussian noise, the GAU algorithm consistently yielded

results with lower AIC values, indicating that the Gaussian noise model of the GAU algorithm was a better fit to the data than the signal-dependent noise model. On the other hand, for data sets corrupted with signal-dependent noise, the AIC values from the GGM results were lower than those from the GAU results for all noise magnitudes tested. Hence, the underlying noise structure of the data set could be revealed by comparing the AIC values obtained through different algorithms having different assumptions of noise structure.

### APPLYING THE ALGORITHMS TO EMG DATA

We next proceeded to analyze electromyographical (EMG) data sets collected from 13 hindlimb muscles of the frog during jumping in order to identify the basis vectors, or muscle synergies, underlying these high-dimensional data sets. Previous studies (Tresch *et al.*, 1999; Cheung *et al.*, 2005; d'Avella and Bizzi, 2005) have suggested that the frog motor system might simplify control of the many degrees of freedom in the muscle space through linear combination of a small number of muscle synergies. However, none of the above-mentioned studies compared performance of different algorithms assuming different noise structures. It is not known also whether frog EMGs collected during natural behaviors are corrupted by signal-dependent noise similar to the kind suggested by Harris and Wolpert (1998). Here, we address this question by applying both the GAU and GGM algorithms to frog EMG data sets, and by comparing AIC values from both algorithms to see which noise model might be a better fit to these physiological data.

Methods for data collection have been described previously (d'Avella *et al.*, 2003). Data collected from 6 different intact frogs during jumping were analyzed. For each frog, the GAU and GGM algorithms were applied to the EMG data to extract 5 synergies. Such a model order was suggested by previous studies (d'Avella *et al.*, 2003; Cheung *et al.*, 2005). Also, synergy extraction was repeated 5 times for each frog and each algorithm, each time with different initializing $W$ (the synergy matrix) and $C$ (the coefficient matrix). The AIC value for each extraction was also computed.

Table 2.1 lists the AIC values for both the GAU and GGM models applied to each of the 6 frogs. For all frogs, the AIC of GGM was smaller than the AIC of GAU. Such a consistent result suggests that the noise underlying frog EMGs might be better described using a signal-dependent noise model whose noise standard deviation is proportional to the

mean EMG amplitude. Another implication is that the muscle synergies extracted using GGM might be closer to the actual physiological synergies underlying jumping than the GAU synergies.

**TABLE 2.1.** The Akaike Information Criterion (AIC) values for the GAU and GGM models applied to frog jumping EMG data (13 muscles, 5 synergies; mean, $n$=5). The MLE estimate for the $\phi$ parameter in the GGM noise model (equation 2.11) is also listed (mean ± SD, $n$=5).

| Animal | GAU (x$10^6$) | GGM (x$10^6$) | MLE est. for $\phi$ (GGM) |
|---|---|---|---|
| Frog 1 | -1.9236 | -3.8506 | 0.5002±0.0117 |
| Frog 2 | -0.5617 | -1.2010 | 0.4529±0.0284 |
| Frog 3 | -0.5095 | -1.3870 | 0.5275±0.0242 |
| Frog 4 | -0.6505 | -1.3020 | 0.4688±0.0112 |
| Frog 5 | -0.6310 | -1.2783 | 0.4606±0.0115 |
| Frog 6 | -0.3357 | -0.7764 | 0.5162±0.0051 |

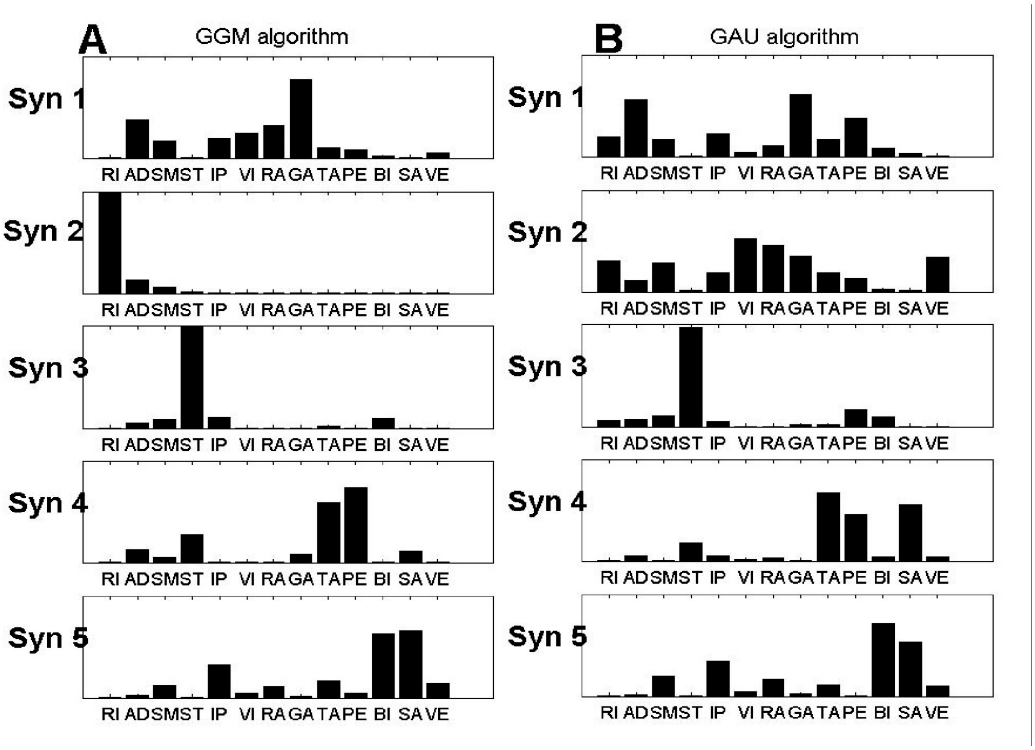


**FIGURE 2.3.** Muscle synergies (Syn) of frog 2 extracted using the GGM (*A*) and the GAU (*B*) algorithms. Results from the extraction repetition with the lowest AIC were shown. The 13 recorded muscles were rectus internus major (RI), adductor magnus (AD), semimembranosus (SM), semitendinosus (ST), ilio-psoas (IP), vastus internus (VI), rectus femoris anticus (RA), gastrocnemius (GA), tibialis anticus (TA), peroneus (PE), biceps (or ilio-fibularis) (BI), sartorius (SA), and vastus externus (VE). Synergies from the two synergy sets were matched by calculating scalar products.

Figure 2.3 shows the jumping muscle synergies extracted using GGM (*A*) and GAU (*B*) for one frog. In this figure, it can be seen that both algorithms yielded similar results for synergies 3-5, all of which were activated during the flexion phase of the jump. However, for synergies 1-2, both of which were activated during jump extension, the GGM and GAU synergies are quite different from each other. A closer examination of these two synergies reveals, for example, that both synergies 1 and 2 from GAU have a strong gastrocnemius (GA) component; however, only synergy 1 from GGM contains GA activation. An interpretation of this observation is that because GA was activated strongly during extension, its EMG was also more variable due to signal-dependent noise. Such variability forced the GAU algorithm to divide the GA extension bursts up between two different synergies. Whether the GAU or GGM synergies correspond better to other physiological measures (such as kinematics) would require further studies and analyses.

## DISCUSSION AND CONCLUSION

In this paper, we have derived a non-negative blind source separation algorithm capable of modeling any noise distribution in the exponential family (equation 2.9). It is shown that our update rules can be reduced to the non-negative matrix factorization algorithm proposed by Lee and Seung (1999, 2001) by assuming constant-variance Gaussian noise. Also, update rules for a signal-dependent noise model were derived (equation 2.10). The ability of both the Gaussian (GAU) and generalized gamma (GGM) algorithms to recover bases from data corrupted with noise was tested using simulated data sets, and it was confirmed that the algorithm performs better if the data noise structure agrees with the noise model of the algorithm (Fig. 2.1). It was further shown that the AIC could be used as a model selection criterion to decide which algorithm might be better fitted to the data (Fig. 2.2). Both the GAU and GGM algorithms were then applied to EMG data collected from 6 frogs. Calculation and comparison of AIC values suggested that frog EMG data might be better described using a signal-dependent noise model.

One of the most important features of the algorithm presented here is that it is generalized to any noise distribution in the exponential family, thus allowing modeling of signal-dependent noise. In this paper we have presented one possible formulation of signal-

dependent noise using the generalized gamma distribution. But other formulations, such as *Gamma*(*WC*, 1) or *N*(*WC*, *WC*), are in principle possible, provided that the resulting algorithms converge. Such flexibility of our algorithm would be particularly useful in analyses of data sets with unknown noise structures. In such cases, basis vectors can be extracted using multiple versions of our algorithm having different noise model assumptions, and a model selection criterion such as AIC can then be applied to gain insight into the underlying data noise structure. For this reason, we think the algorithms presented here might be useful in analyses of not only EMG signals, but also a wide variety of high-dimensional physiological data (such as neuronal firing rates of multiple neurons).

*Chapter 3*

# Muscle synergies as centrally organized modules: evidence from deafferentation[§]

[§] This thesis chapter is a revision of a previously published article:
Cheung VCK, d'Avella A, Tresch MC, Bizzi E (2005) Central and sensory contributions to the activation and organization of muscle synergies during natural motor behaviors. *J. Neurosci.* **25**(27): 6419-6434.

## INTRODUCTION

Motor coordination can be understood as the mechanism by which the central nervous system (CNS) controls the many degrees of freedom in the redundant musculoskeletal system to achieve purposeful behaviors (Bernstein, 1967). Earlier experiments have suggested that the CNS may simplify control by activating a small number of modules (Grillner, 1985; Bizzi *et al.*, 1991; Stein and Smith, 1997; Tresch *et al.*, 2002), formulated as muscle synergies, or activation profiles across a set of muscles, the linear combination of which can generate diverse motor patterns (Tresch *et al.*, 2002; Hart and Giszter, 2004; Ting and Macpherson, 2005). Previous studies examining this hypothesis have relied on animals with intact afferents (Saltiel *et al.*, 2001), or have characterized predominantly feed-forward, ballistic movements such as cutaneous reflexes (Tresch *et al.*, 1999) and kicking (d'Avella *et al.*, 2003). The role of sensory feedback in synergy organization and activation has thus remained an open question.

The simplest role of feedback in such a modular motor system would be to modulate activation of centrally organized synergies (Fig. 3.1-A1). Spinal and/or supraspinal neuronal networks would specify the particular muscle activation balance of each synergy, with sensory feedback playing no role in its specification. It is well established that complex electromyographical (EMG) patterns during many behaviors can be generated without afferents (Grillner, 1975; Delcomyn, 1980). Force field primitives of the spinalized frog before and after deafferentation were also very similar (Leob *et al.*, 1993), suggesting the presence of modules directly activated by central commands.

In addition, there may be synergies organized within the CNS, but specifically accessible only by feedback signals (Fig. 3.1-A2). This possibility is suggested by the corrective responses observed upon limb perturbations in the cat (Forssberg, 1979) and frog (Kargo and Giszter, 2000a). Alternatively, sensory inflow may modify activations of individual muscles within a synergy (Fig. 3.1-A3), or contribute to specification of synergies by reorganizing interneuronal networks (Pearson, 2004) (Fig. 3.1-A4). Yet another possibility is that synergies arise as emergent properties of the entire neural network comprising both central circuits and feedback loops. Whether differences between afferented and deafferented EMGs (Grillner and Zangger, 1984; Kargo and Giszter, 2000b) reflect afferent modulation of centrally organized synergies, recruitment of afferent-specific

synergies, feedback reorganization of existing synergies, or emergent properties of the motor circuitry has remained unclear.

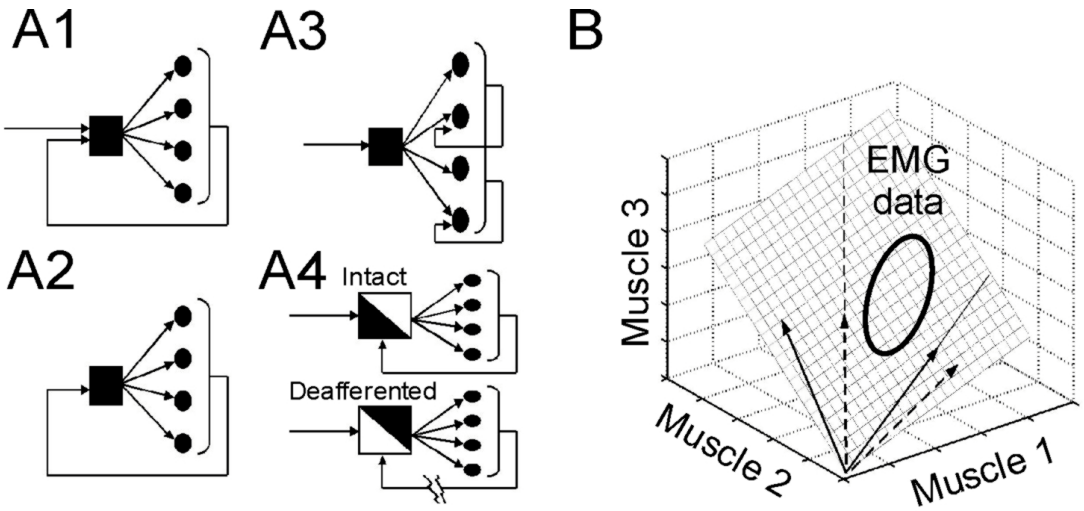


**FIGURE 3.1.** Hypotheses and concepts invoked in this study. *A,* Different possible roles of sensory feedback in a modular motor system. Each black square represents a CNS neuronal network specifying the muscle activation balance within a muscle synergy, and each circle represents the motoneuron pool for a muscle. *A1,* In this scheme, synergies are organized centrally, and activated by spinal and/or supraspinal commands. Sensory feedback can modulate their activation, but plays no role in specifying the activation balances within the synergies. *A2,* Centrally organized synergies specifically accessible by sensory inflow. These synergies may be responsible for the corrective responses seen upon limb perturbations (Forssberg, 1979; Kargo and Giszter, 2000a). *A3,* Centrally organized synergies acting as templates for motor output generation. Each muscle within each synergy is independently regulated by afferent signals. *A4,* Feedback reorganization of CNS neuronal assemblies, resulting in altered synergy structures after deafferentation. It is possible that when feedback is available, some interneurons capable of generating motor patterns under the deafferented condition are not activated, while some other interneurons requiring sensory signals for activation are recruited instead. This scheme is similar to the model put forth by Pearson (2004). *B,* The concept of synergy bases spanning a subspace. Shown in the diagram is a hypothetical case with EMG data collected from 3 muscles. The EMG trajectory is described by two different sets of synergy bases, shown in solid and dashed arrows, respectively. Despite having different structures, these two synergy sets span the same 2-d subspace within the 3-d EMG space, and can describe the EMG data equally well.

In this study, we assess to what extent the CNS relies on centrally organized synergies accessible by central commands (Fig. 3.1-A1) to generate motor outputs for locomotor behaviors. We collected hindlimb EMGs from intact frogs during swimming and jumping, before and after ipsilateral deafferentation. Then, we exploited a non-negative factorization algorithm (Lee and Seung, 1999) to identify synergies shared by, and synergies specific to, the intact and deafferented data sets. Our analyses indicate that to a large degree,

both data sets can be explained by a set of shared synergies. We conclude that a small number of centrally organized synergies, activated by central commands but modulated by sensory feedback, plays a predominant role in generating complex motor patterns for locomotor behaviors.

## MATERIALS AND METHODS

### Surgeries and experimental procedure.

Four adult bullfrogs (*Rana catesbeiana*, 270-590 g) were studied. On each frog, three surgeries were performed on separate days. In all surgeries, the frog was anesthetized with ice and tricaine (ethyl 3-aminobenzoate methanesulfonate; Sigma, St. Louis, MO; 0.1 mg/g) injected into the left iliac lymph-sac. In the first surgery, the dorsal nerve roots were exposed by rongeuring vertebrae 5-6 and cauterizing the dura mater. In the second surgery, bipolar EMG electrodes were implanted into 13 muscles in the right hindlimb, including (following nomenclature of Ecker, 1971): rectus internus major (RI), adductor magnus (AD), semimembranosus (SM), semitendinosus (ST), ilio-psoas (IP), vastus internus (VI), rectus femoris anticus (RA), gastrocnemius (GA), tibialis anticus (TA), peroneus (PE), biceps (or ilio-fibularis) (BI), sartorius (SA), and vastus externus (VE). All wires were passed subcutaneously to a 37-pin d-sub connector, secured to the back skin with a custom-made plastic platform and Nexaband glue (Veterinary Products Lab., Phoenix, AZ). The crimp contacts were insulated by epoxy. The third surgery was a deafferentation procedure: dorsal roots 7-9 on the right side were severed at the level of the sixth vertebra. After some of the surgeries, antibiotic (enrofloxacin; Bayer, Shawnee Mission, KS; $10^{-3}$ mg/g) was also administered subcutaneously for prophylaxis.

Patterns of EMG during unrestrained swimming and jumping, performed in a specially designed tank and cage, respectively, were collected after electrode implantation and before deafferentation during 1-2 experimental sessions conducted over 1-3 days. After deafferentation, another 1-2 sessions of EMG data were collected over 1-3 days. Between surgeries and experimental sessions, the frog was allowed at least 18 hours for recovery. Episodes of both in-phase and out-of-phase swimming (Nauwelaerts and Aerts, 2002) were either spontaneous, or elicited by lightly touching the hindlimbs with a plastic rod. During all swimming trials, removable light-bodied Permlastic (Kerr USA, Romulus, MI) was also

used to provide additional insulation of the EMG-electrode connector against water. For the jumping responses, a few of them were spontaneous, but most of them were elicited by lightly scratching the skin of either hindlimb with a pair of sharp forceps. All swimming and jumping experimental trials were also videotaped, and the EMG and video recordings were approximately synchronized by a digital counter. Correct placement of electrodes was confirmed in post-mortem examinations following all experimental procedures. All procedures were approved by the MIT Committee on Animal Care prior to experimentation.

**Data collection and preprocessing.**

Continuous EMG signals, both intact and deafferented, were amplified (gain = 10000), band-pass filtered (10-1000 Hz) through differential AC amplifiers, and digitized (1000 Hz). Using a custom software written in Matlab (Mathworks, Natick, MA), the EMG traces were manually parsed into segments, each containing a single jump or consecutive swimming cycles. The parsed data were then high-pass filtered (window-based FIR; $50^{th}$-order; cutoff = 50 Hz) to remove any motion artifacts. Subsequently, the data were rectified, low-pass filtered (FIR; $50^{th}$-order; 20 Hz) to remove noise, and integrated over 10-ms intervals. The EMGs were not normalized before further analyses.

**Analysis stage I: Extracting muscle synergies separately**.

We modeled EMGs of each behavior as the linear combination of a set of muscle synergies, each represented as an activation profile across the 13 recorded muscles, and activated by a time-varying activation coefficient. We hypothesized that the synergies and their activations are non-negative, and are identifiable by applying the non-negative matrix factorization algorithm (NMF) (Lee and Seung, 1999) to the EMG data. The NMF algorithm is a reasonable method for extracting synergies because as a result of its non-negativity constraint imposed on both the synergies and their activations, the synergies extracted tend to be sparse rather than holistic, and thus, more physiologically interpretable (Lee and Seung, 1999). Also, unlike methods such as the independent component analysis (Bell and Sejnowski, 1995; Hyvärinen and Oja, 2000), NMF does not rely on the assumption that synergy activations are statistically independent; hence, NMF is more compatible with the previous finding that activations of multiple synergies might be correlated (Saltiel *et al.*, 2001).

Our synergy analyses were divided into two stages. In stage I, our goals were to estimate the number of intact and deafferented synergies, the number of synergies shared by the two data sets, as well as the amount of variance representing systematic variation within each data set. We considered the intact and deafferented data sets separately, and extracted synergies from each of them. Stated formally, our model in stage I has the following mathematical form:

$$\mathbf{d}(t) = \sum_{a=1}^{N} c_a(t) \bullet \mathbf{w}_a \ , \tag{3.1}$$

where, for the 13 recorded muscles, $\mathbf{d}(t)$ represents the EMG data at time $t$, $\mathbf{w}_a$ is a 13-dimensional vector denoting the $a^{\text{th}}$ synergy, $c_a(t)$ is the time-varying scalar activation coefficient for $\mathbf{w}_a$, and $N$ is the total number of synergies extracted. Note that equation (3.1) can also be stated in matrix notation as $D=WC$, where $D$, $W$, and $C$ are the data, synergy, and coefficient matrices, respectively. In stage I, the above model was applied separately to each of the intact and deafferented data sets, for each of the swimming and jumping behaviors.

The intact and deafferented synergies and their activation coefficients were extracted by implementing the NMF multiplicative update rules (Lee and Seung, 2001) in Matlab. Under these update rules, at each iteration new estimates of $W$ and $C$ were calculated by multiplying the current estimates by factors depending on $D$ and current estimates of $W$ and $C$. This iterative estimation procedure was stopped after convergence of the reconstruction error $||D-WC||$, defined here as having 20 consecutive iterations with a change of EMG reconstruction $R^2$ <0.01%.

The NMF algorithm requires the number of synergies extracted to be specified before application of the algorithm. Since such information was not known *a priori*, for each behavior, we extracted 1 to 10 synergies from subsets of the intact and deafferented data sets, respectively. At each number of synergies, we performed cross-validation (Browne, 2000) as a step for estimating the correct number of synergies (see also next section). In our cross-validation procedure, the jumping or swimming EMG segments were first divided into four equal partitions. Three of the four partitions were pooled together, and synergies were extracted from this pooled data set. These synergies were then validated by fitting them to the remaining unused partition (using NMF with $W$ held fixed and $C$ updated across

iterations), and the quality of fit was quantified as an $R^2$ value. This cross-validation procedure was repeated 20 times at each number of synergy, each time with different random $W$ and $C$ (uniformly distributed between 0 and 1) initiating NMF, and with different randomly selected data partitions for cross-validation.

For each number of synergies, a baseline cross-validation $R^2$ was also computed by repeating the extraction-validation procedure described above on the same training and testing EMG segments, but with the samples of each muscle in each data set independently and randomly shuffled. An actual cross-validation $R^2$ higher than this baseline cross-validation $R^2$ suggests that systematic variation in the data set is captured by the synergies.

**Estimating the numbers of intact and deafferented synergies for stage I.**

In cross-validation, when more synergies are extracted than necessary, some synergies may capture random fluctuations rather than systematic variation within the extraction data set. In such a case, the quality of fit of the synergies to the validation data is expected to be reduced. Thus, the correct number of intact or deafferented synergies (denoted by $N^{in*}$ and $N^{de*}$ for the intact and deafferented data sets, respectively) can be estimated by plotting the cross-validation $R^2$ against the number of synergies extracted. A point beyond which further increase in the number of synergies decreases the $R^2$, or at which the slope of the $R^2$ curve changes sharply, indicates that any additional synergies beyond that point capture only noise and/or a small additional fraction of data variation. This point should then, in principle, be the correct number of synergies.

However, our previous experience with cross-validation $R^2$ curves from frog EMGs during natural behaviors has shown that the slope of the curve usually decreases gradually as the number of synergies extracted increases, making it difficult to determine the number of synergies by visual inspection of the $R^2$ curve. To estimate $N^{in*}$ and $N^{de*}$ objectively, we fit portions of the $R^2$ curve to straight lines using standard least squares technique, first including all data points on the curve in the fit, and then the 2$^{nd}$ to 10$^{th}$ points, and so on until only the 9$^{th}$ and 10$^{th}$ points were included. As the range of the fit moves towards the right side of the curve, the mean squared error (MSE) of the fit is expected to decrease because the $R^2$ curve approaches a straight line as the number of synergies extracted increases. The correct number of synergies can then be estimated as the first point on the $R^2$ curve at which the linear fit of all points from that point to the 10$^{th}$ point produces a small

MSE. In other words, this chosen point represents the point at which the $R^2$ curve plateaus to a straight line. In our analyses, the first point on the $R^2$ curve whose corresponding MSE falls below $5\times10^{-5}$ was selected as the correct number of synergies for stage I (see arrows in Fig. 3.3A,B). This criterion resulted in numbers of synergies corresponding to qualitative inspection of the $R^2$ curves, but performed this identification objectively.

**Two approaches of assessing synergy similarity for stage I.**

After estimating the correct numbers of synergies, we proceeded to assess similarity between the intact and deafferented synergy sets. The intact and deafferented synergy sets each define a lower-dimensional subspace within the 13-dimensional EMG space. The intact and deafferented synergies can be similar in the weaker sense that their subspaces overlap each other, or in the stronger sense that the actual synergy bases of the two synergy sets are similar. Thus, it is possible that the intact and deafferented synergy sets are similar only in their subspaces, but not in their actual synergies. For example, in Fig. 3.1B, the two sets of synergies, represented by solid and dashed arrows, respectively, are different in their structures (i.e., they point to different directions in the EMG space); but they nonetheless span the same 2-dimensional subspace within the 3-dimensional EMG space. Comparing the intact and deafferented subspaces as well as the structures of the synergies underlying them, we can then assess whether the NMF algorithm is capable of finding only the shared subspace, or the actual synergy bases spanning the shared subspace as well.

For the first approach of similarity assessment, we evaluated the degree of overlap between the two subspaces respectively spanned by the intact and deafferented synergies by computing a set of principal angles using an algorithm described in Golub and Van Loan (1983) (pp. 428-430). If, for instance, the intact and deafferented subspaces share a 3-dimensional common subspace, the cosines of the first three principal angles should be close to one. We refer to the number of principal angles whose cosines are $\geq 0.90$ as the shared subspace dimensionality (*ssd*) between two synergy sets. If the intact and deafferented subspaces completely overlap each other, then *ssd* = number of intact or deafferented synergies, whichever number is smaller.

The second, more stringent, method of assessing similarity between the intact and deafferented synergies evaluates the degree of similarity between the actual synergy vectors using scalar products. We first computed the best-matching scalar products between the

intact and deafferented synergy sets. The vector norm of each synergy was first normalized to one. Each synergy in the intact set was then matched to the synergy in the deafferented set giving the maximum scalar product between them. If two or more synergies from one set were matched to the same synergy in the other set, we isolated all multiply-matched and unmatched synergies, and the total scalar product of every possible matching combination between those two sets of remaining synergies was calculated; the combination giving the maximum total scalar product was then considered to be the best match. We refer to the number of best-matching scalar products ≥ 0.90 as the number of shared synergies (*nss*), representing the number of synergies which are similar between the intact and deafferented synergy sets.

Since extraction of synergies was repeated 20 times, there were 20×20 = 400 intact and deafferented synergy sets for comparison, and thus, 400 *ssd* and 400 *nss* values. The average *ssd* and *nss* values were calculated for each animal and each behavior.

**Baseline synergy similarity for stage I.**

The procedures described above estimate the number of shared dimensions (*ssd*) and the number of shared synergies (*nss*) between intact and deafferented data sets. To assess the significance of these values, we computed baseline *ssd* and *nss* values using a randomization procedure. For each of the 400 pairs of intact-deafferented synergy sets, two sets of random synergies comprising $N^{in*}$ and $N^{de*}$ vectors were generated by random shuffling of the vector components in the original intact and deafferented synergy sets, respectively. The *ssd* and *nss* values between these two sets of random synergies were then determined. Calculation of baseline *ssd* or *nss*, between every intact-deafferented pair of synergy sets, was repeated 20 times, each time with the vector components shuffled anew. For each repetition, the average baseline *ssd* and *nss* across the 400 pairs of synergy sets were also calculated.

**Analysis stage II**: **Simultaneous extraction of shared and data set-specific synergies.**

In the stage-I procedures described above, synergies were extracted separately from the intact and deafferented data sets. The subspaces spanned by these synergies were then compared to one another, and the similarity between the synergies themselves, assessed. However, there are a number of potential shortcomings with the stage-I analysis.

First, while the stage-I intact and deafferented subspaces may share a common subspace, the synergies extracted from either data set may not actually span this common subspace, because this common subspace does not necessarily coincide with the subspace defined by any subset of the extracted synergies. To see this, consider a 3-dimensional space defined by 3 synergies, represented as vectors along the x-, y-, and z-axes, respectively. Suppose further that the common subspace is a 2-dimensional tilted plane within this 3-dimensional space. Obviously, this plane is not spanned by any 2 of the 3 synergies. In such a case, the compositions of the 2 synergies preserved after deafferentation remain unclear from the stage-I extraction results.

Second, separate extraction of synergies performed in stage I might be expected to underestimate the number of intact or deafferented synergies ($N^{in*}$ or $N^{de*}$). If the activation of 2 synergies tended to co-vary within one of the two data sets, NMF would tend to combine these synergies together into a single synergy. If in the other data set these 2 synergies were activated independently, NMF would identify them correctly for this data set. Thus, if, for instance, 2 of 5 intact synergies tended to co-vary in the deafferented data set, the stage-I estimates of $N^{in*}$ and $N^{de*}$ would be 5 and 4, respectively, whereas the correct estimates should be 5 and 5. Therefore, the stage-I estimates of data set dimensionalities are expected to underestimate the true number of intact and deafferented synergies.

Beyond this problem in identifying the correct numbers of synergies, such co-variation of synergies might also result in an underestimation of the number of synergies preserved after deafferentation. Again, if, for instance, 2 synergies tended to co-vary in the deafferented but not in the intact data set, the combined deafferented synergy uncovered by NMF would be seen as dissimilar to its two corresponding intact synergies. Thus, if there were 5 synergies in fact shared between the two data sets, the *nss* value would indicate that only 3 synergies were shared.

In order to account for such possibilities, we therefore performed a second stage of analysis, using a novel reformulation of the NMF algorithm. Information from both data sets is utilized simultaneously in this reformulation, allowing both for synergies shared between the data sets, and for synergies observed specifically within one data set or another. We let the NMF algorithm search, by itself, for synergies common to both data sets while at the same time allowing the algorithm to isolate synergies relevant only to each data set. Our model in stage II can be stated formally as follows:

$$\mathbf{d}^{in}(t) = \sum_{a=1}^{N^{sh}} c_a^{sh\_in}(t)\mathbf{w}_a^{sh} + \sum_{a=1}^{N^{insp}} c_a^{insp}(t)\mathbf{w}_a^{insp};$$
$$\mathbf{d}^{de}(t) = \sum_{a=1}^{N^{sh}} c_a^{sh\_de}(t)\mathbf{w}_a^{sh} + \sum_{a=1}^{N^{desp}} c_a^{desp}(t)\mathbf{w}_a^{desp}, \quad (3.2)$$

where the superscripts *in* and *de* respectively stand for intact and deafferented, and *sh*, *insp*, and *desp* stand for synergies shared by the two data sets, synergies specific to the intact data set, and synergies specific to the deafferented data set, respectively. Note that the coefficients, $c_a^{sh\_in}(t)$ and $c_a^{sh\_de}(t)$, though activating the same synergy $\mathbf{w}_a^{sh}$, in fact contribute to the intact and deafferented EMG data, respectively. The number of intact or deafferented synergies in the stage-II model is then the sum of the number of shared synergies and the number of synergies specific to each data set (i.e., $N$ for intact data set = $N^{sh}+N^{insp}$; and $N$ for deafferented data set = $N^{sh}+N^{desp}$). Converting the equations in (3.2) into their matrix forms, we have

$$D^{all} = [D^{in} \mid D^{de}] = W^{all} \bullet C^{all};$$
$$W^{all} = [W^{sh} \mid W^{insp} \mid W^{desp}], \quad (3.3)$$
$$C^{all} = \left[\begin{array}{c|c} C^{sh\_in} & C^{sh\_de} \\ \hline C^{insp} & \mathbf{0} \\ \hline \mathbf{0} & C^{desp} \end{array}\right].$$

In the above equations, for the columns in $C^{all}$ corresponding to the range of the deafferented data, the rows for the intact-specific synergies were set to zero, because by definition they do not contribute to the generation of the deafferented data. Similarly, in the $C^{all}$ columns used for reconstructing the intact data, the rows for the deafferented-specific synergies were set to zero.

We extracted shared and specific synergies simultaneously from equal numbers of intact and deafferented EMG segments using the NMF algorithm. As a result of its multiplicative update rules, if the initial condition of any matrix component is zero, the estimate of that matrix component after any number of iterations remains zero. Thus, the only manipulation necessary for stage II is to set the relevant matrix components of the initial $C^{all}$ to zero (as indicated in equation (3.3)) while choosing random values (uniformly distributed between 0 and 1) for all the nonzero entries. These initial conditions ensure that the specific synergies in $W^{all}$ will explain only one of the two data sets.

**Estimating the numbers of intact and deafferented synergies for stage II.**

As in stage I, the stage-II procedure we have described requires the number of synergies to be specified before application of the algorithm. To estimate the number of shared synergies ($N^{sh*}$), stage-II synergies were extracted with $N^{sh}$ progressively increasing from 1 to the smaller of $N^{in}$ or $N^{de}$. As $N^{sh}$ increases, the degree of overlap between the subspaces defined by the intact-specific and deafferented-specific synergies is expected to decrease, because every time $N^{sh}$ is increased by one, another feature shared between the intact and deafferented EMGs is taken up as a shared synergy. Thus, $N^{sh*}$ is indicated by the $N^{sh}$ at which there is minimal overlap between the subspaces spanned by the intact- and deafferented-specific synergies. The degree of this overlap between the specific synergies was quantified as a dimensionality value by finding the number of principal angles with cosines ≥ 0.90. The smallest $N^{sh}$ with a mean shared dimensionality between the specific synergies (averaged across 20 extraction repetitions) below 0.25 was taken to be the correct number of shared synergies. This threshold of 0.25 ensures that at the chosen $N^{sh*}$, sharing between the specific synergies is observed in less than 5 of the 20 extraction runs.

The above procedure estimates the correct number of shared synergies given particular total numbers of intact and deafferented synergies, comprising shared synergies and synergies specific to each data set. To estimate the correct total numbers of synergies, we utilized the results of the stage-I analysis, choosing the total numbers of intact and deafferented synergies to be those numbers which gave an $R^2$ in the stage-II analysis closest to the $R^2$ obtained in the stage-I analysis (see Fig. 3.5B). This $R^2$ criterion guarantees that the stage-II solution explains the intact and deafferented data sets as well as the stage-I solution, while directly identifying the synergies which are shared between intact and deafferented data sets.

**Clustering synergies of different frogs.**

After selecting the stage-II numbers of synergies, for each frog and behavior, the synergy solution for the extraction repetition giving the highest overall $R^2$ was selected for further analyses. For each behavior, the shared and data set-specific synergies from the four frogs were pooled together, and grouped into classes by cluster analysis. The Matlab statistics-toolbox functions pdist (Minkowski option; p=3), linkage (ward option), and

cluster were applied sequentially to the pooled synergy matrix. The number of clusters was determined by selecting the minimum number of clusters partitioning the synergies such that no two synergies from each cluster were from the same frog.

**Analyzing the coefficients of the stage-II shared synergies.**

For each frog, and each behavior, the activation coefficients of the stage-II shared synergies before and after deafferentation were analyzed. The coefficients of each shared synergy were multiplied by the magnitude of that synergy vector, so that the coefficients represent activation of unit vectors. A Matlab graphical user interface was then built for manual parsing of the coefficient time traces into extension and flexion phases, so that the extension phase of each cycle would correspond to a burst of activation of the extension synergies. The peak coefficient amplitudes of each phase, and of each shared synergy, before and after deafferentation were compared (t-test, $\alpha = 0.05$).

Effects of deafferentation on the duration of synergy activation were characterized by first fitting the coefficient time trace of each phase to a Gaussian function using standard nonlinear least squares method (see pp. 32-42 of Bates and Watts, 1988). The time points corresponding to mean $\pm$ 2×(standard deviation) of the Gaussian function were defined to be the offset and onset of the activation burst, respectively. For the extension phases, if the burst offset as defined above lay within the flexion phase following that extension phase, the burst offset was redefined to be the last time point of that extension phase. Likewise, for the flexion phases, if the burst onset as defined above lay within the adjoining extension phase, the onset was redefined to be the first time point of that flexion phase. The coefficient burst duration of each phase, and of each shared synergy, before and after deafferentation were then compared (t-test, $\alpha = 0.05$). Only the phases where the Gaussian fit explained the original coefficient time trace with $R^2 \geq 60\%$ were included in our statistics of burst duration.

**Patterns of correlation between synergies.**

To investigate whether the activation of two or more synergies are coordinated by central mechanisms or sensory feedback, we computed the Pearson's correlation coefficient ($r$) between the peak coefficient amplitudes of every pair of shared synergies for each of the two phases, for each of the intact and deafferented conditions, and for each behavior. Statistical significance of the difference between the intact $r$ and the deafferented $r$ was

determined by Fisher's *r*-to-*Z* transformation method ($\alpha = 0.01$; see pp. 647-651 of Hays, 1994).

## RESULTS

From 4 frogs, we collected and analyzed EMG signals from 13 hindlimb muscles during intact swimming (91, 315, 311, and 200 cycles from frogs 1-4, respectively), deafferented swimming (56, 205, 169, and 140), intact jumping (97, 47, 76, and 50 jumps), and deafferented jumping (172, 60, 22, and 56).

### Synergies underlying intact and deafferented behaviors – visual inspection of EMG data.

Figure 3.2 shows representative examples of EMG segments, all collected from frog 1, during intact and deafferented swimming and jumping. In Fig. 3.2A, there are five consecutive swimming cycles. Notice that in this episode, the muscles SM, GA, and VE tend to be co-activated as a group, and that their peak cycle amplitudes stay relatively constant across these five cycles. The muscles RI, AD, and IP tend to be coactive with the SM-GA-VE group, but their peak cycle amplitudes from the first to last cycles decrease gradually. More importantly, the same two muscle groups seem to underlie the deafferented swimming EMG patterns in Fig. 3.2B as well. Both the SM-GA-VE and RI-AD-IP groups are present in the two episodes of Fig. 3.2B, but the amplitude of the latter group appears to be significantly smaller in the second episode than in the first episode. Thus, visual inspection of EMG data suggests that some of the swimming muscle synergies may be preserved after deafferentation, and that their activation across time may be differentially modulated.

Shown in Fig. 3.2C is an EMG segment collected during an intact jump. It is divided into three phases, labeled *a*, *b*, and *c*, for ease of visual inspection. Phase *a* is characterized by activation of all 13 muscles. In phase *b*, we notice EMG bursts in SM, IP, BI and SA. Phase *c*, on the other hand, features a prominent ST with some activity in TA and PE. A similar tripartite structure is also seen in deafferented jumping EMGs, exemplified by Fig. 3.2D. The three phases in Fig. 3.2D, labeled *a'*, *b'*, and *c'*, are analogous to phases *a*, *b*, and *c* of Fig. 3.2C, respectively. Despite the fact that *b'* has a longer duration than *b*, the SM-IP-BI-SA

group active in phase *b* is also noticeable in the deafferented episode, but in both *b'* and *c'*. Note also that the TA and PE bursts in *c'* have larger peak amplitudes and longer durations than those in phase *c*. It appears therefore that in jumping, at least some of the synergy structures remain invariant across deafferentation, though the amplitudes and time courses of their activation may be affected.

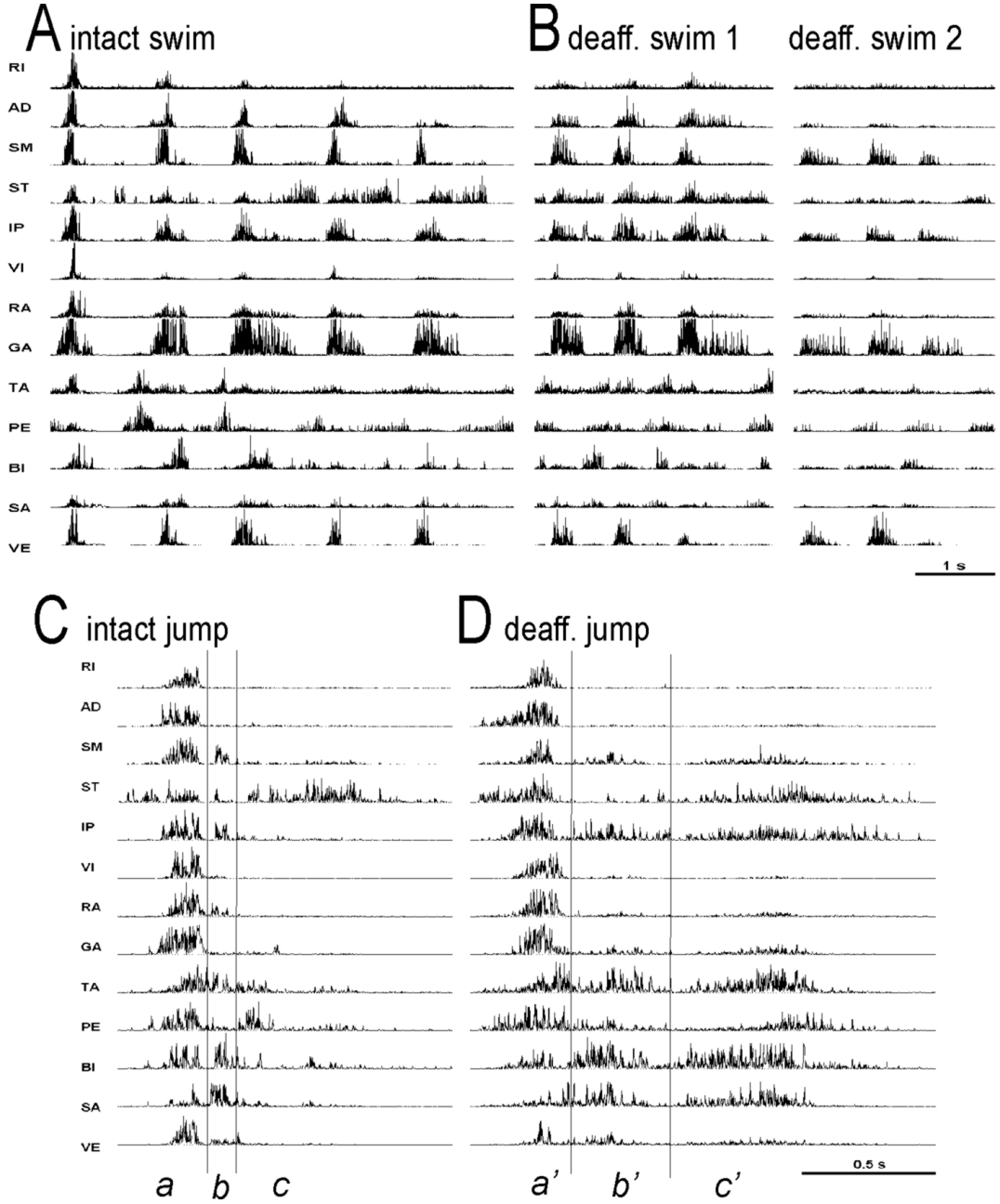


**FIGURE 3.2.** Examples of EMG data collected from intact and deafferented locomotor behaviors. Shown are EMG data collected from 13 hindlimb muscles of frog 1, high-pass filtered (50th-order FIR, cutoff = 50 Hz) to remove motion artifacts, and subsequently rectified. *A*, EMGs of 5 consecutive swimming cycles before dorsal root transection. *B*, Two different swimming episodes

after deafferentation, each of which comprises three consecutive cycles. *C*, EMGs of a representative jump before deafferentation. *D*, EMGs of a deafferented jump. *C* and *D* are divided into three phases for ease of visual inspection. Notice that the deafferented EMGs appear to involve the same muscle groups embedded within the intact EMGs. Comparison of the onset times of AD, ST, IP, and PE in phase *a* of *C* with those in phase *a'* of *D* suggests that there may be synergies specific to the intact or deafferented state. See Results for more detailed descriptions.

A more detailed comparison between phase *a* (Fig. 3.2C) and phase *a'* (Fig. 3.2D) shows that the relative onset times of some muscles were altered after dorsal root transection. In phase *a*, ST activity precedes that of all other muscles; in phase *a'*, however, the onset times of ST, AD, IP, and PE seem to be the same. Thus, it is possible that the structures of some muscle synergies are changed after deafferentation.

The above observations motivated us to hypothesize that swimming and jumping EMGs can be generated by linear combination of muscle synergies represented as time-invariant activation profiles across the 13 muscles, and to expect that most of these synergies are preserved after feedback deprivation. We further hypothesized that the structures of the muscle synergies, as well as their corresponding time-varying activation coefficients, can be identified by applying the NMF algorithm (Lee and Seung, 1999; Tresch *et al.*, 1999) to the EMG data. As explained in Materials and Methods, for each of the swimming and jumping behaviors, we systematically assessed the number of synergies preserved after deafferentation and identified the structures of the preserved synergies in two stages of analyses. In stage I, we extracted synergies from the intact and deafferented data sets separately, and assessed similarity between the two synergy sets. Our comparison in stage I led us to realize some limitations of extracting synergies from individual data sets separately, prompting us to analyze our data in a second analytical stage in which we extracted synergies from pooled intact and deafferented data. We will first illustrate our two-stage method using the swimming EMGs as an example. The swimming synergies will then be presented, followed by the analytical results of the jumping EMGs.

## Muscle synergies underlying swimming before and after deafferentation

### Analysis stage I: intact and deafferented swimming EMGs have low and similar dimensionalities.

We first estimated the number of synergies in the intact and deafferented data sets by extracting 1 to 10 synergies from each of them. Extraction results at each number of

synergies were cross-validated (see Methods). The quality of fit in the validation step was quantified as an $R^2$ value.

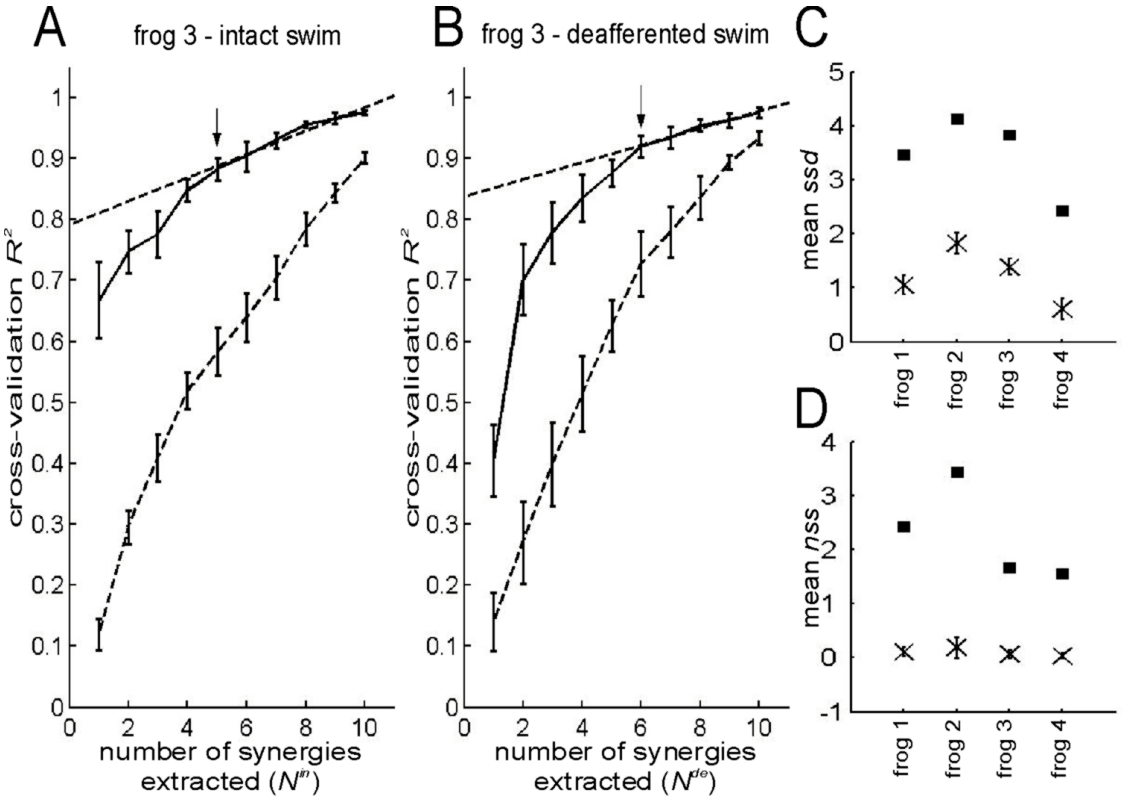


**FIGURE 3.3.** Stage-I analysis of swimming EMGs before and after deafferentation. *A, B,* In analysis stage I, we extracted and cross-validated 1 to 10 synergies from the intact and deafferented data sets, respectively, and the quality of fit of the synergies to the validation data was quantified as $R^2$ values. To assess the $R^2$ expected by chance, we also repeated the extraction and validation procedures on the same training and testing data sets, but with the samples of each muscle in both independently and randomly shuffled. We then estimated the correct number of intact and deafferented synergies by fitting decreasing portions of the actual $R^2$ curve to straight lines, and the first point on the curve whose portion approximates a straight line (as indicated by a small mean squared error in the linear fit) was selected as the correct number of synergies. *A*, Cross-validation $R^2$ curves for the intact swimming data set of frog 3. Solid curve, $R^2$ curve from original data (mean ± s.d.; $n$=20). Dotted curve, $R^2$ curve from shuffled data (mean ± s.d.; $n$=20). Black arrow indicates the correct number of intact synergies estimated by our procedure, and the dotted straight line is its corresponding linear fit. *B,* Cross-validation $R^2$ curves for the deafferented swimming data set of frog 3. Same key as *A*. *C, D,* Assessing similarity between the intact and deafferented synergies using two approaches. *C,* The degree of overlap between the subspaces respectively spanned by the intact and deafferented synergy sets is indicated by the average shared subspace dimensionality (*ssd*) values (■; $n$ =20×20=400). The average *ssd*'s expected by chance were computed by calculating principal angles between shuffled synergy sets (×; mean ± 5×s.d. after 20 trials of shuffling). *D,* The number of stage-I intact synergies whose actual structures were preserved after deafferentation was indicated by the average *nss* (number of shared synergies) values (■; $n$ =20×20=400). The average *nss*'s expected by chance were computed by calculating scalar products between shuffled synergy sets (×; mean ± 5×s.d. after 20 trials of shuffling).

Figures 3.3A and 3.3B show plots of $R^2$ against the number of swimming synergies extracted for both the intact and deafferented data sets of frog 3 (solid curve; mean ± s.d.; $n$=20), along with the $R^2$ levels expected if the data sets were not generated by muscle synergies (shuffled data: dashed curve; mean ± s.d.; $n$=20). It is clear that in both the intact and deafferented conditions, about 90% of variance in the original swimming EMGs is explained by 5-6 synergies (i.e., $R^2 \approx 90\%$) whereas by chance, the same amount of variance is explained only when 10 synergies are employed. This result indicates that both the intact and deafferented swimming data sets possess low and similar dimensionalities. Similar results were obtained from the other three frogs.

To systematically compare synergies of intact swimming with those of deafferented swimming, the numbers of synergies present in the intact and deafferented data sets (denoted by $N^{in*}$ and $N^{de*}$, respectively) need to be determined. Ideally, the point on the $R^2$ curve at which the slope changes sharply indicates such a number. As exemplified by the $R^2$ curve of Fig. 3.3A, however, the slopes of most of our $R^2$ curves decrease gradually as the number of synergies extracted increases, making estimation of $N^{in*}$ and $N^{de*}$ by visual inspection of the $R^2$ curves difficult.

Nonetheless, all of our $R^2$ curves do seem to approach a straight line as the number of synergies extracted increases (Fig. 3.3A-B). This observation prompted us to estimate the correct number of synergies by fitting decreasing portions of each $R^2$ curve to straight lines, and choosing the first point at which a straight line fits the portion of the $R^2$ curve well (see Materials and Methods for more details). In Fig. 3.3A-B, the point of the best estimate of the number of synergies on the $R^2$ curve is indicated by an arrow; its corresponding linear fit is shown as a dotted straight line. For frog 3 swimming (Fig. 3.3A-B), then, $N^{in*}$ and $N^{de*}$ are 5 and 6, respectively, confirming that the intact and deafferented dimensionalities are similar for the swimming EMGs.

Table 3.1 summarizes our estimates of the numbers of synergies in frogs 1-4. With the exception of frog 1 (the frog with the least amount of swimming data collected), in all frogs $N^{in*}$ and $N^{de*}$ are either the same or differ only by one, further suggesting that the number of synergies underlying intact swimming is similar to that underlying deafferented swimming. Note also in Table 3.1 that in all frogs, a high percentage of data variance

(~90%) is explained by the chosen numbers of synergies, indicating that our estimates of $N^{in*}$ and $N^{de*}$ provide a good description of the observed data.

**TABLE 3.1. Estimating the number of synergies shared between the intact and deafferented synergy sets in two stages of analyses.**

In analysis stage I, we compared the intact and deafferented synergies using two approaches: by assessing the degree of overlap between the subspaces respectively spanned by the intact and deafferented synergies (shared subspace dimensionalities, or *ssd*), and by calculating scalar products to estimate the number of shared synergies (*nss*) before and after deafferentation. In analysis stage II, the number of synergies preserved after deafferentation is reflected by the $N^{sh*}$ value at our estimates of the correct total numbers of intact and deafferented synergies ($N^{in*}$ and $N^{de*}$). The $R^2$ values listed refer to the percentage of data variance explained by the listed numbers of synergies (averaged across 20 extraction repetitions). The abbreviation CV stands for cross-validation.

| Frog/ Behavior | Stage I | | | | | | Stage II | | | | | | |
|---|---|---|---|---|---|---|---|---|---|---|---|---|---|
| | $N^{in*}$ | $N^{de*}$ | *ssd* | *nss* | CV $R^2$ (%) | | $N^{in*}$ | $N^{de*}$ | $N^{sh*}$ | $N^{insp*}$ | $N^{desp*}$ | $R^2$ (%) | |
| | | | | | int-act | deaff | | | | | | int-act | deaff |
| frog 1-swim | 6 | 4 | 3.46 | 2.43 | 89.0 | 91.3 | 6 | 4 | 4 | 2 | 0 | 88.4 | 91.5 |
| frog 2-swim | 6 | 6 | 4.13 | 3.44 | 91.2 | 89.7 | 6 | 6 | 6 | 0 | 0 | 91.1 | 90.2 |
| frog 3-swim | 5 | 6 | 3.83 | 1.66 | 88.3 | 92.0 | 5 | 6 | 5 | 0 | 1 | 87.4 | 91.5 |
| frog 4-swim | 4 | 4 | 2.43 | 1.56 | 86.3 | 91.7 | 5 | 4 | 4 | 1 | 0 | 87.0 | 92.4 |
| frog 1-jump | 4 | 4 | 2.18 | 1.45 | 91.3 | 90.4 | 4 | 5 | 4 | 0 | 1 | 90.6 | 90.0 |
| frog 2-jump | 4 | 4 | 2.10 | 1.01 | 90.3 | 90.6 | 4 | 5 | 4 | 0 | 1 | 89.6 | 89.9 |
| frog 3-jump | 4 | 5 | 2.06 | 1.01 | 90.1 | 91.1 | 4 | 5 | 3 | 1 | 2 | 89.2 | 90.9 |
| frog 4-jump | 5 | 4 | 2.00 | 0.95 | 90.9 | 89.7 | 6 | 4 | 4 | 2 | 0 | 91.1 | 88.8 |

**Analysis stage I: assessing similarity between the intact and deafferented swimming synergies.**

To assess whether the intact and deafferented swimming synergies are similar, we first assessed the degree of overlap between the subspaces spanned by the sets of $N^{in*}$ intact synergies and the $N^{de*}$ deafferented synergies (shared subspace dimensionality, or *ssd*), respectively, by computing principal angles (Golub and Van Loan, 1983).

Figure 3.3C shows the mean *ssd* between the intact and deafferented swimming synergies of each frog (■; $n = 20 \times 20 = 400$), and the corresponding mean baseline *ssd* between random synergies (×; mean ± 5×s.d. after 20 trials of shuffling). It is clear that in all four frogs, the actual *ssd* lies well above the baseline *ssd* ($p < 0.01$), suggesting that there is a non-trivial degree of intersection between the intact and deafferented synergy subspaces. Rounding the mean *ssd* values, we see that on average, 3 of 6, 4 of 6, 4 of 5, and 2 of 4 dimensions of the intact synergy subspaces of frogs 1 through 4, respectively, are shared with their corresponding deafferented synergy subspaces. Our analyses thus far indicate that NMF succeeded in identifying swimming synergies before and after deafferentation sharing a common subspace, even though the two subspaces do not completely overlap each other.

We then directly compared intact and deafferented synergies by calculating scalar products between the intact and deafferented synergy sets, estimating the number of shared synergies (*nss*) between the intact and deafferented synergy sets.

Figure 3.3D shows the mean *nss* values of frogs 1 through 4 (■; $n = 20 \times 20 = 400$) together with their baseline *nss* values computed by matching randomly shuffled synergies (×; mean ± 5×s.d. after 20 trials of shuffling). In all frogs, the *nss* value is clearly above its baseline ($p < 0.01$), indicating that the sharing of synergies is well above that expected by chance. Rounding the mean *nss* of each frog, we see that on average, 2 of 6, 3 of 6, 2 of 5, and 2 of 4 synergies extracted from the intact data sets of frogs 1 through 4, respectively, are similar to those extracted from deafferented data sets. Note that in all frogs except frog 4, the mean *nss* is smaller than the mean *ssd*. Therefore, extracting intact and deafferented swimming synergies separately, NMF found synergies sharing a common subspace, but the shared synergies themselves do not span the entire shared subspace, as illustrated in the following example.

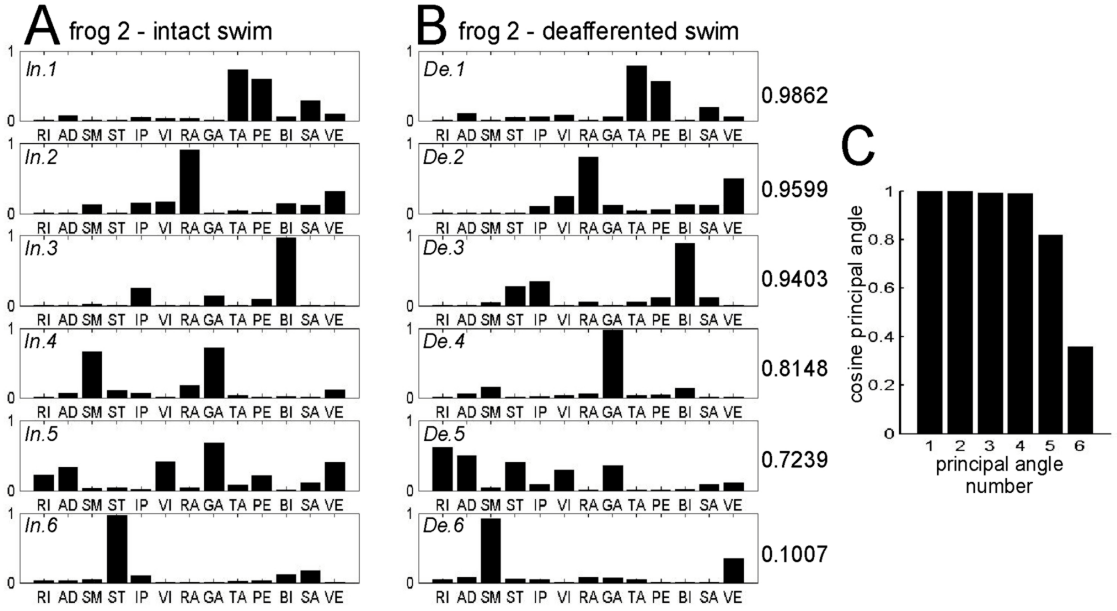


**FIGURE 3.4.** Examples of swimming synergies from analysis stage I. *A, B,* A pair of intact and deafferented swimming synergy sets of frog 2. Each of the 6 intact synergies was matched to the deafferented synergy giving the best-matching scalar product, its actual value shown between the two panels. *C,* The cosines of the 6 principal angles between the intact and deafferented subspaces defined by the synergies shown in *A* and *B*. Notice that while only 3 of 6 best-matching scalar products are greater than 0.90 in *A* and *B*, the cosines of 4 of 6 principal angles are greater than 0.90. This indicates that although only 3 synergies are apparently similar to one another, the two subspaces actually share a 4-dimensional common subspace. Therefore, the *nss* by itself potentially underestimates the degree of similarity between the intact and deafferented synergies. See Results for further discussion.

**The shared stage-I synergies do not span the entire shared subspace – illustrative examples.**

Shown in Fig. 3.4A-B is an example of intact and deafferented synergy sets identified for frog 2 swimming. The top-most synergy pair, *In.1*/*De.1*, is the pair with the highest scalar product (value shown between panels), and the bottom-most pair, *In.6*/*De.6*, the pair with the smallest. As can be seen, synergies *In.1* and *In.2* are almost identical in structure to *De.1* and *De.2*, respectively. Synergy *In.6*, with its prominent ST component, is not found in the deafferented synergy set, even though both *De.3* and *De.5* have more ST activation than *In.3* and *In.5*, respectively. Similarly, although synergy *De.6* (SM and VE) is not found in the intact synergy set, *In.4* has more prominent SM and VE than its corresponding *De.4*. These observations already suggest that even though only 3 of the 6 scalar products are greater than 0.90, the degree of similarity between the two sets of synergies shown in Fig. 3.4A-B

may well be more than three. Examination of the cosines of the six principal angles between the two synergy sets of Fig. 3.4A-B is consistent with such a possibility. As illustrated in Fig. 3.4C, the cosines of the first four angles are close to one, suggesting that the intact and deafferented synergy subspaces defined by the synergies in Fig. 3.4A-B share a 4-dimensional common subspace. In other words, while *In.1-In.3* (or *De.1-De.3*) are three of the synergies spanning this common subspace, there is at least one more common synergy embedded within the subspace defined by *In.4-In.6*, or that defined by *De.4-De.6*.

Taken together, the results in Fig. 3.3C-D and the examples in Fig. 3.4 suggest strongly that (1) there are shared synergies underlying both the intact and deafferented swimming data sets, and (2) at this analytical stage, NMF uncovers synergies sharing a common subspace, but is unable to find an explicit set of non-negative synergies spanning this shared space. Moreover, as described in Materials and Methods, combinations of synergies within one data set would be expected to result in stage I underestimating the number of intact or deafferented synergies, as well as the number of synergies preserved across deafferentation. This underestimation is a consequence of the fact that stage I identifies muscle synergies by extracting them separately for each data set. In the stage II analysis described below, we attempted to overcome these limitations to better assess the number of shared synergies underlying both the intact and deafferented EMG data sets.

**Analysis stage II: Extracting shared and data set-specific swimming synergies.**

In the second stage of our analyses, we used a different synergy extraction method to obtain an explicit set of synergies spanning the subspace shared by intact and deafferented EMGs. In stage II, we pooled these two data sets together, and exploited the NMF update rules to search for synergies common to both data sets while simultaneously allowing the algorithm to isolate any synergies specific to either data set.

In stage II, three parameters – the number of intact, deafferented, and shared synergies – have to be specified before application of the NMF algorithm. Figure 3.5A is an example from frog 2 swimming illustrating our method of estimating the correct number of shared synergies ($N^{s/d*}$), given particular numbers of intact and deafferented synergies (both of which were set to be 6 in this example). As the number of shared synergies ($N^{s/d}$) was progressively increased, the dimensionality of the subspace shared between the specific synergies also decreased as expected. As can be seen, the shared dimensionality fell below

our pre-defined threshold of 0.25 only when six shared synergies were extracted. Thus, in this example if there were 6 intact and 6 deafferented swimming synergies, all six intact synergies were preserved after deafferentation.

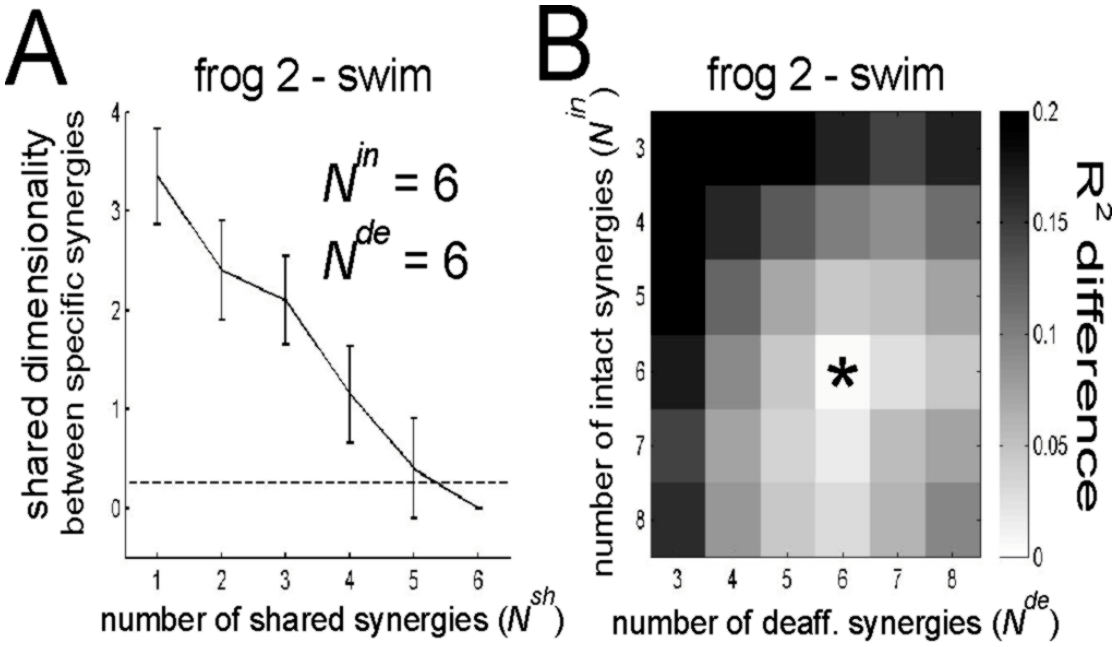


**FIGURE 3.5.** Determining the numbers of synergies in analysis stage II. In our stage II model, three numbers of synergies – $N^{in*}$, $N^{de*}$, and $N^{sh*}$ – need to be specified. Our strategy for estimating the correct values of these three parameters was to extract synergies with $N^{in}$, $N^{de}$ = 3…8 (i.e., 6×6=36 combinations of $N^{in}$ and $N^{de}$), and at each of these combinations, estimate $N^{sh*}$ for that particular combination of $N^{in}$ and $N^{de}$. We then proceeded to estimate $N^{in*}$ and $N^{de*}$ by examining the difference between the stage-II and stage-I $R^2$ values. *A,* Estimating the correct number of shared synergies in frog 2 swimming given $N^{in}$, $N^{de}$ = 6. As $N^{sh}$ was progressively increased, the dimensionality of the subspace shared between the specific synergies decreased. The correct number of shared synergies can be estimated by noting the point at which the specific synergies do not share a common subspace. Shown in *A* is the mean shared dimensionality between the specific synergies (mean ± s.d., $n$=20). The shared dimensionality at the maximum $N^{sh}$ was defined to be zero, for at this point there are no specific synergies to be compared. The smallest $N^{sh}$ with a shared dimensionality falling below 0.25 was selected to be $N^{sh*}$. *B,* Estimating the correct total numbers of intact and deafferented synergies (frog 2 swimming). For each of the intact and deafferented data sets, we computed an $R^2$ value for the stage-II solution at each combination of $N^{in}$ and $N^{de}$, and calculated the absolute difference between the stage-I cross-validation $R^2$ and the stage-II $R^2$. The intact and deafferented differences were then summed together. We reason that the correct stage-II estimates of $N^{in*}$ and $N^{de*}$ is the combination whose $R^2$ values come closest to the stage-I values. In *B*, this $R^2$ difference across the 36 combinations of $N^{in}$ and $N^{de}$ is depicted as a grayscale map – the darker the color, the more $R^2$ difference at a combination. The combination with the minimum $R^2$ difference is marked with an asterisk (*).

On the other hand, the correct total numbers of intact ($N^{in*}$) and deafferented ($N^{de*}$) synergies for stage II, each of which comprises both shared and specific synergies, were estimated by comparing the stage-II $R^2$ values at different combinations of total numbers of

intact and deafferented synergies with the $R^2$ values obtained in stage I (see Materials and Methods and legend to Fig. 3.5). Figure 3.5B illustrates the difference between the stage-I and stage-II $R^2$ values as the total numbers of intact and deafferented synergies were respectively varied from 3 to 8. At each of these 36 (=6×6) combinations, the number of shared synergies was estimated using the method illustrated in Fig. 3.5A. For frog 2 swimming (Fig. 3.5B), the stage-II $R^2$ values came closest to the stage-I $R^2$ values when 6 intact synergies and 6 deafferented synergies were extracted. Taken together, results of Fig. 3.5A and Fig. 3.5B thus suggest that for frog 2 swimming, the stage-II estimates of $N^{in*}$, $N^{de*}$ and $N^{sh*}$ are 6, 6, and 6, respectively – that is, there are 6 synergies underlying both the intact and deafferented swimming data sets, all 6 of which are preserved after feedback deprivation.

We applied the above methods to all frogs to determine the number of total and shared synergies, and our results are shown in the right column of Table 3.1. In all frogs, the degree of sharing between the intact and deafferented synergy sets suggested by stage II (as indicated by $N^{sh*}$) is greater than that suggested by stage I (as indicated by *ssd*) by 1-2 synergies. More importantly, if we compare the total numbers of intact and deafferented synergies ($N^{in*}$ and $N^{de*}$) determined in stage I to those estimated in stage II (Table 3.1), we see that the stage-I numbers are the same as the stage-II numbers in all but one instance ($N^{in*}$ of frog 4 swimming). Therefore, the increased sharing discovered in stage II is *not* a consequence of explaining the data sets with more synergies. This observation further supports that the shared synergies identified in stage II represent underlying structures shared by the intact and deafferented data sets, rather than being just the result of the algorithm averaging out structures specific to each data set.

**Most swimming synergies are preserved after deafferentation.**

Figure 3.6 shows all the shared and data set-specific synergies from the extraction repetition with the highest overall $R^2$ in each frog. As can be seen, for frogs 1 through 4, respectively, 4 of 6, 6 of 6, 5 of 6, and 4 of 5 synergies appear as shared synergies, suggesting that most synergies underlying intact swimming are preserved after deafferentation. Therefore, the swimming EMGs are predominantly generated by centrally encoded synergies accessible by spinal and/or supraspinal commands.

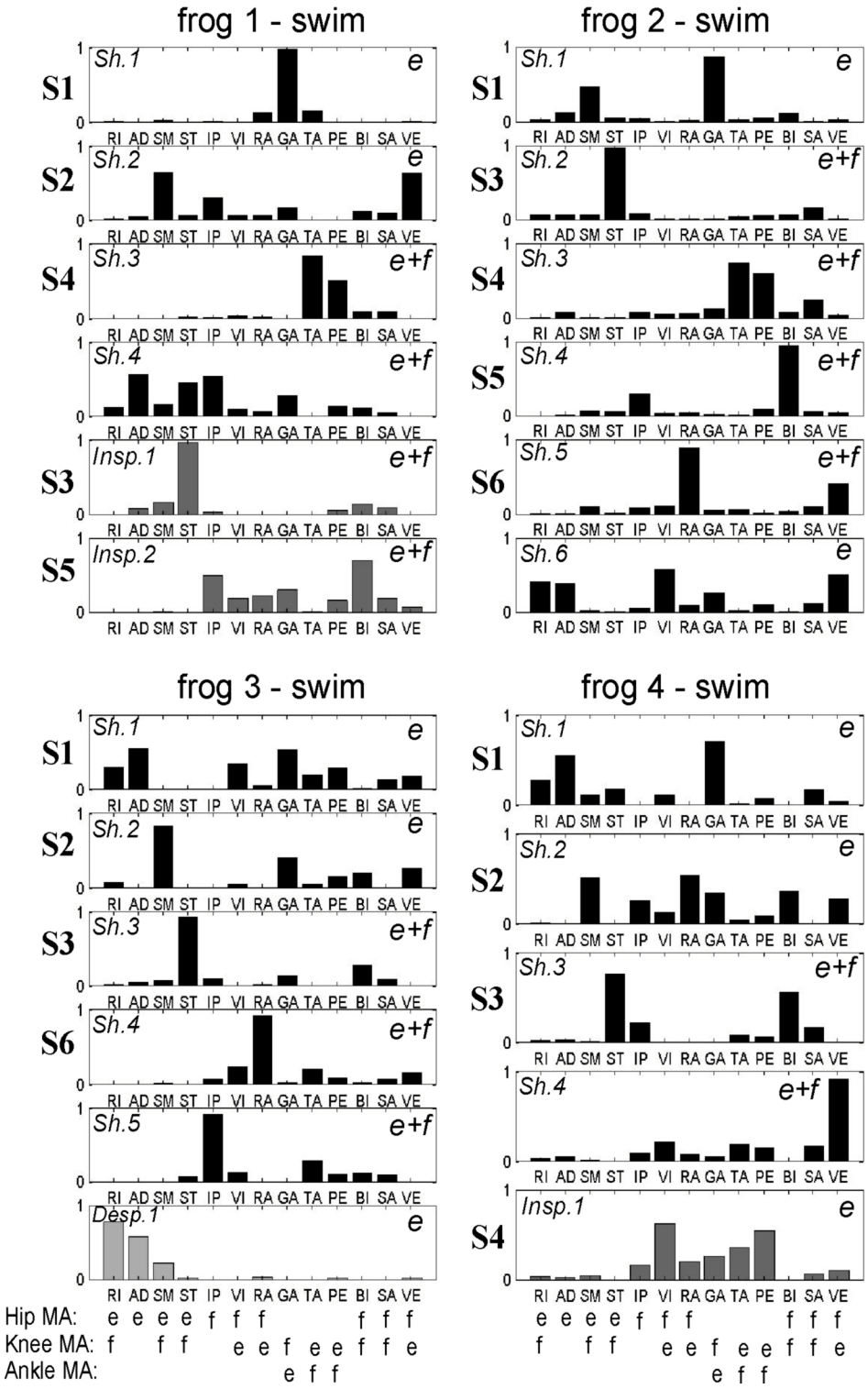


**FIGURE 3.6.** Swimming synergies of all frogs (analysis stage II). Shown in this figure are the stage-II synergies of the extraction repetition with the highest $R^2$ of the four frogs. The synergies shared between the intact and deafferented data sets are labeled *Sh*; synergies specific to the intact data set, *Insp*; and synergies specific to the deafferented data set, *Desp*. Synergies active only during the extension phase of the swimming cycle are marked with *e* on their right sides, and those active in

both the extension and flexion phases, *e+f*. All synergies shown in this figure were clustered into 6 classes (S1-S6), and the class of each synergy is marked on its left side. The sign of the moment arms (MA) around the hip, knee, and ankle joints of the 13 muscles included in this study are listed below the synergies of frog 3 and frog 4 (e = extensor action; f = flexor action). Moment arm signs are based on results of Kargo and Rome (2002), and Cajigas-González (2003).

Inspection of synergies in Fig. 3.6 further suggests that many of the swimming synergies are similar across frogs. For instance, in both frog 1 and frog 2, a shared synergy with TA and PE activation can be seen, and all frogs possess a shared synergy with a prominent ST component. Some synergies appear to be frog-specific, however. For instance, synergy *Sh.4* of frog 4, with its prominent VE component, does not resemble any synergy from the other three frogs.

In light of the similarity of the swimming synergies across frogs, we proceeded to group them into classes by cluster analysis. We progressively increased the number of clusters until no two synergies in each cluster were from the same frog. Six clusters of shared swimming synergies (denoted by S1 to S6) were identified; four of them (S1 to S4) were found in at least three of the four frogs. The principal muscles involved in these 6 groups of synergies are summarized below. Refer to Fig. 3.6 for a summary of the functions of each muscle listed (as reflected by the signs of the moment arms).

*Synergy S1* is an extension synergy comprising the ankle extensor GA (all frogs), and the hip extensors RI and AD (frogs 3 and 4).

*Synergy S2* is another extension synergy comprising SM, VE, and GA – extensors of the hip, knee, and ankle, respectively (frogs 1, 3, and 4).

*Synergy S3* includes the hip extensor/knee flexor, ST (all frogs) and the hip-knee flexor BI (frogs 3 and 4).

*Synergy S4* includes two knee extensors/ankle flexors – TA and PE (frogs 1, 2 and 4), as well as the hip-knee flexor SA (frog 2).

*Synergy S5* features the hip flexor IP and the hip-knee flexor BI (frogs 1 and 2).

*Synergy S6* features two hip flexors/knee extensors – RA and VE (frogs 2 and 3).

Both S1 and S2 were active only during the extension phase of the swimming cycle. All the rest of the synergies, except the S4 of frog 4, were active in both the extension and flexion phases of the swimming cycle.

To summarize our analyses of the swimming EMGs, in our stage I analysis, we established that both the intact and deafferented swimming data sets possess similar and low

dimensionalities (Fig. 3.3A-B; Table 3.1). The intact and deafferented synergy sets identified in stage I share a common subspace (Fig. 3.3C; Fig. 3.4C), indicating that at least some synergies are preserved after deafferentation. In order to tackle some potential limitations of stage I (see Materials and Methods), we proceeded to our stage II analysis (Fig. 3.5). The degree of sharing was found to be higher in stage II (Table 3.1), suggesting that our stage-II analysis can better assess the degree of sharing through combining information from different data sets. Most of the stage-II synergies were identified as synergies shared between the intact and deafferented data sets (Fig. 3.6), suggesting that most synergies underlying the swimming behavior are centrally-encoded modules activated by spinal and/or supraspinal commands. Six classes of swimming synergies were identified (Fig. 3.6), two of which (S1 and S2) were activated during the extension phase only.

## Muscle synergies underlying jumping before and after deafferentation

We applied the same two-stage method illustrated above for swimming EMGs to the data collected during jumping to assess whether the same conclusions hold for the jumping behavior.

### Stage-I analysis of jumping EMGs: the intact and deafferented data sets possess similar low dimensionalities.

Our stage-I analyses of the jumping EMGs show that like the swimming data sets, the intact and deafferented jumping data sets possess low and similar dimensionalities. Shown in Fig. 3.7A-B are the stage-I cross-validation $R^2$ curves for frog 4 jumping analogous to those shown in Fig. 3.3A-B for frog 3 swimming. We see that in both the intact and deafferented data sets, 4 to 5 synergies are sufficient to explain ~90% of data variance. The $R^2$ curves resulting from extracting synergies from the unshuffled data sets (solid curve; mean ± s.d.; $n$=20) also lie well above those expected by chance (shuffled data: dashed curve; mean ± s.d.; $n$=20), confirming that actual data structures within the data sets are captured by our synergies. By fitting the $R^2$ curves to straight lines, $N^{in*}$ and $N^{de*}$ for frog 4 jumping were determined to be 5 and 4, respectively (arrows in Fig. 3.7A-B). Similar results were obtained from the other three frogs (Table 3.1).

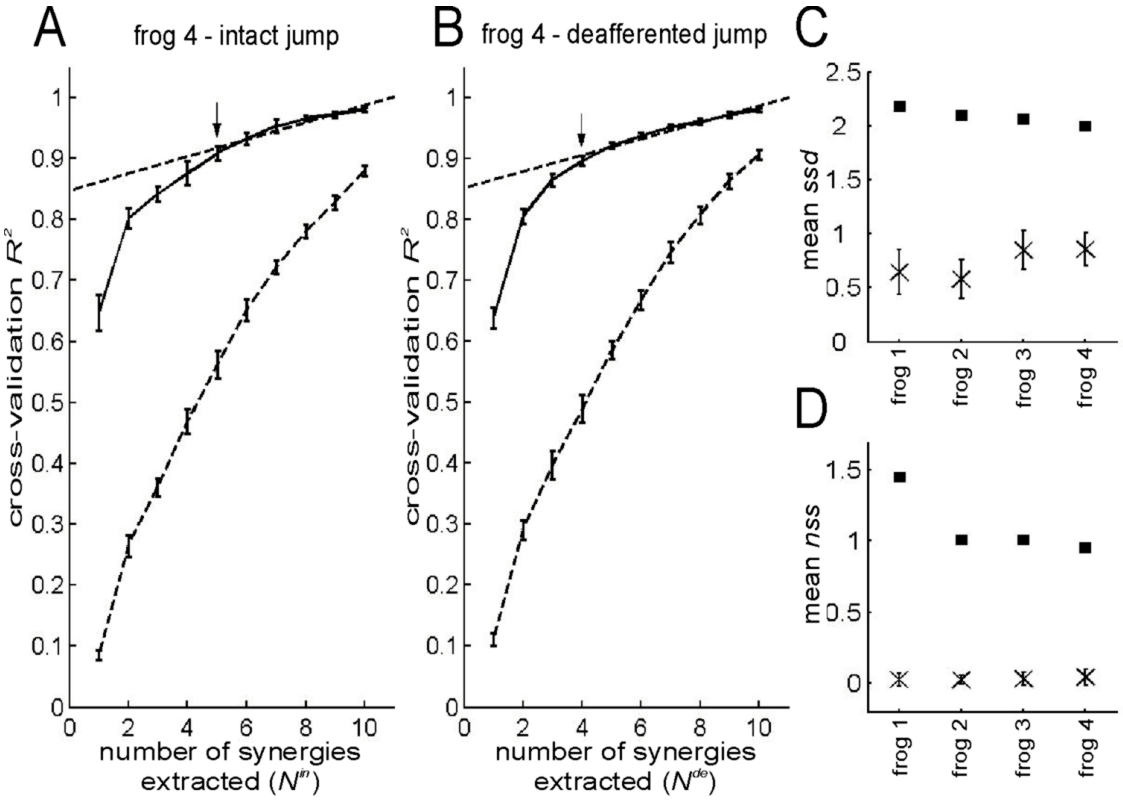


**FIGURE 3.7.** Stage-I analysis of jumping EMGs before and after deafferentation. *A, B,* We applied the same stage-I procedure as applied to the swimming EMGs (described in the legend for Figs. 3.3A-B) to our jumping EMGs. *A*, Cross-validation $R^2$ curves for the intact jumping data set of frog 4. Solid curve, $R^2$ curve from original data (mean ± s.d.; $n$=20). Dotted curve, $R^2$ curve from shuffled data (mean ± s.d.; $n$=20). Black arrow indicates the correct number of intact synergies estimated by our procedure, and the dotted straight line is its corresponding linear fit. *B,* Cross-validation $R^2$ curves for the deafferented jumping data set of frog 4. Same key as *A*. *C, D,* Assessing similarity between the intact and deafferented synergies using two approaches. *C,* The degree of overlap between the subspaces respectively spanned by the intact and deafferented synergy sets is indicated by the average shared subspace dimensionality (*ssd*) values (■; $n$ =20×20=400). The average *ssd*'s expected by chance were computed by calculating principal angles between shuffled synergy sets (×; mean ± 5×s.d. after 20 trials of shuffling). In all frogs, the actual mean *ssd* is well above its corresponding baseline value ($p < 0.01$). *D,* The number of stage-I intact synergies whose actual structures were preserved after deafferentation was indicated by the average *nss* (number of shared synergies) values (■; $n$ =20×20=400). The average *nss*'s expected by chance were computed by calculating scalar products between shuffled synergy sets (×; mean ± 5×s.d. after 20 trials of shuffling). In all frogs, the actual mean *nss* is higher than its corresponding baseline value ($p < 0.01$).

We also compared the similarity between the subspaces defined by each synergy set (*ssd*), and between the actual synergies in each set (*nss*). While the *nss* values indicate that for all four frogs, on average only 1 intact jumping synergy also appears as a deafferented synergy (Fig. 3.7D), our subspace analysis suggests that the intact and deafferented synergy subspaces share a 2-dimensional subspace (Fig. 3.7C). As in swimming, the difference

between the *ssd* and *nss* values implies that in stage I, NMF finds only a common subspace shared between the intact and deafferented jumping synergies, but not all the synergies spanning this shared subspace.

**Stage-II analysis of jumping EMGs: most jumping synergies are preserved after deafferentation.**

We then proceeded to stage II, and determined $N^{in*}$, $N^{de*}$, and $N^{sh*}$ for each frog by pooling the intact and deafferented jumping data sets together. As summarized in Table 3.1, our stage-II analyses suggest that 4 of 4, 4 of 4, 3 of 4, and 4 of 6 intact jumping synergies for frogs 1 through 4, respectively, are preserved after deafferentation, and reconstruction of the original EMGs using these numbers of synergies yields $R^2$ values of ~90%. Therefore, the hypothesis that most synergies underlying the intact EMGs are preserved after feedback deprivation holds not only for swimming, but for jumping as well. All the shared and data set-specific jumping synergies of each frog from the extraction repetition with the highest overall $R^2$ are summarized in Fig. 3.8.

For frog 3, if we compare its intact-specific synergy (*Insp.1*) with one of its deafferented-specific synergies (*Desp.1*), we see that both contain activation of similar muscles (RI, SM, VI, RA, GA, and VE), but in different balances between these muscles. The intact-specific synergy (*Insp.1*) has relatively more GA and VE than its deafferented counterpart (*Desp.1*), but less RI and SM. One interpretation of this observation is that sensory feedback may fine-tune the activation of individual muscles within a synergy, thereby altering the synergy's muscle activation balance profile (Fig. 3.1-A3). A similar interpretation may account for the similarity and difference between frog 4's *Sh.1* and *Insp.1* (Fig. 3.8).

As in our analysis of the swimming synergies, we grouped our jumping synergies into classes by cluster analysis. We found 6 classes of shared jumping synergies (denoted by J1 to J6), 4 of which (J1 to J4) were found in at least three of the four frogs. Their principal muscles are summarized below. Refer to Fig. 3.8 for a summary of the functions of each muscle listed (as reflected by the signs of the moment arms).

*Synergy J1* is an extension synergy found in all frogs comprising all major extensors of the hindlimb – RI, AD, and SM (hip extensors); VI, RA, VE, TA and PE (knee extensors); as well as GA (ankle extensor).

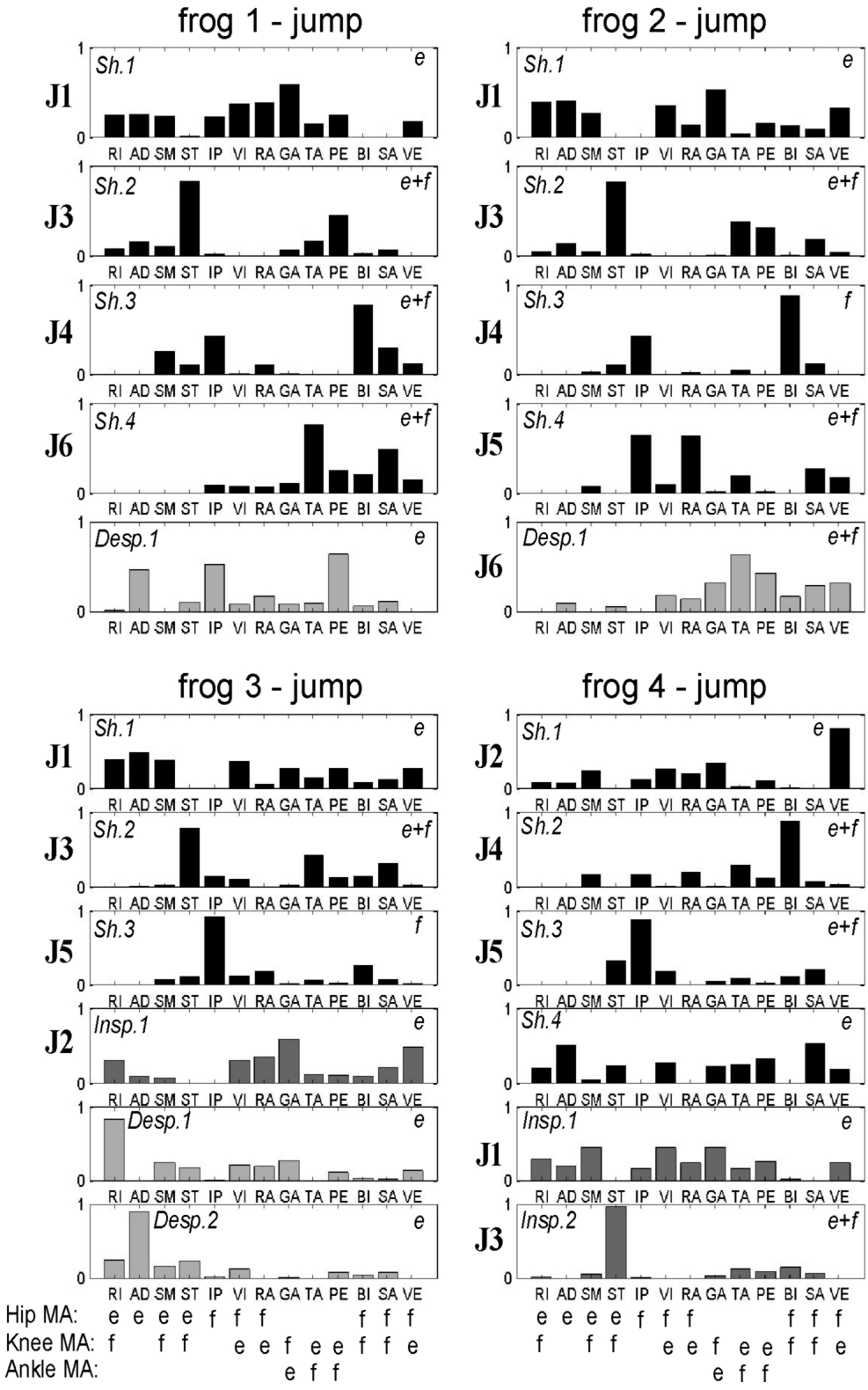


**Figure 3.8.** Jumping synergies of all frogs (analysis stage II). Shown in this figure are the stage-II synergies of the extraction repetition with the highest $R^2$ of the four frogs. The synergies shared between the intact and deafferented data sets are labeled *Sh*; synergies specific to the intact data set, *Insp*; and synergies specific to the deafferented data set, *Desp*. Synergies active only during the

extension phase of jumping are marked with *e* on their right sides; those active only during the flexion phase, with *f*; and those active in both phases, *e+f*. All synergies shown in this figure were clustered into 6 classes (J1-J6), and the class of each synergy is marked on its left side. The sign of the moment arms (MA) around the hip, knee, and ankle joints of the 13 muscles included in this study are listed below the synergies of frog 3 and frog 4 (e = extensor action; f = flexor action). Moment arm signs are based on results of Kargo and Rome (2002), and Cajigas-González (2003).

*Synergy J2* is an extension synergy found only in frogs 3 and 4. It includes RI (frog 3), SM (frog 4), and the extensors VI, RA, GA, and VE.

*Synergy J3* includes the hip extensor/knee flexor ST (all frogs), the knee extensors/ankle flexors TA and PE (frogs 1, 2, and 3) and the hip flexor/knee flexor SA (frogs 2 and 3).

*Synergy J4* includes the hip flexor IP and the hip-knee flexor BI, with more BI than IP (frogs 1, 2, and 4); the hip extensor/knee flexor SM is found in frogs 1 and 4; and the hip-knee flexor, SA, in frogs 1 and 2.

*Synergy J5* features mostly the hip flexor IP (frogs 2, 3, and 4), and also RA (frogs 2 and 3), SA (frogs 2 and 4), and ST (frog 4).

*Synergy J6* contains activation in the two knee extensors/ankle flexors TA and PE, as well as SA, BI, and VE (frogs 1 and 2).

In all frogs, synergies J1 and J2 were active only during the extension phase of jumping. Most of the rest of the synergies were active in both the extension and flexion phases of jumping.

Even though a detailed analysis of the similarities and differences between the swimming and jumping synergies is beyond the scope of this study (see instead, d'Avella and Bizzi, 2005), it is evident from our results (Figs. 3.6 and 3.8) that some synergies are shared between the two behaviors (e.g., compare frog 2's S5 and J4; frog 3's S1 and J1) while some other synergies appear to be specific to swimming (e.g., S2) or jumping (e.g., frog 2's J5). Our results thus support the idea that there are pattern-generating circuitries shared between behaviors so that control is simplified (Grillner, 1985; Soffe, 1993; Stein, 2005), as well as behavior-specific modules adapted to the specific demands of each task (Pratt *et al.*, 1996; Jing *et al.*, 2004).

To summarize our analyses of the jumping EMGs, in stage I we found that both the intact and deafferented jumping data sets possess low and similar dimensionalities (Fig. 3.7A-B). In stage II, most of the synergies were extracted as synergies shared between the intact and deafferented data sets (Fig. 3.8), allowing us to conclude that most synergies

underlying the jumping behavior are centrally organized modules activated by spinal and/or supraspinal commands. Six classes of jumping synergies were identified (Fig. 3.8), two of which (J1 and J2) were activated during the extension phase only. We note also that many jumping synergies appear to be similar to our swimming synergies (Figs. 3.6 and 3.8).

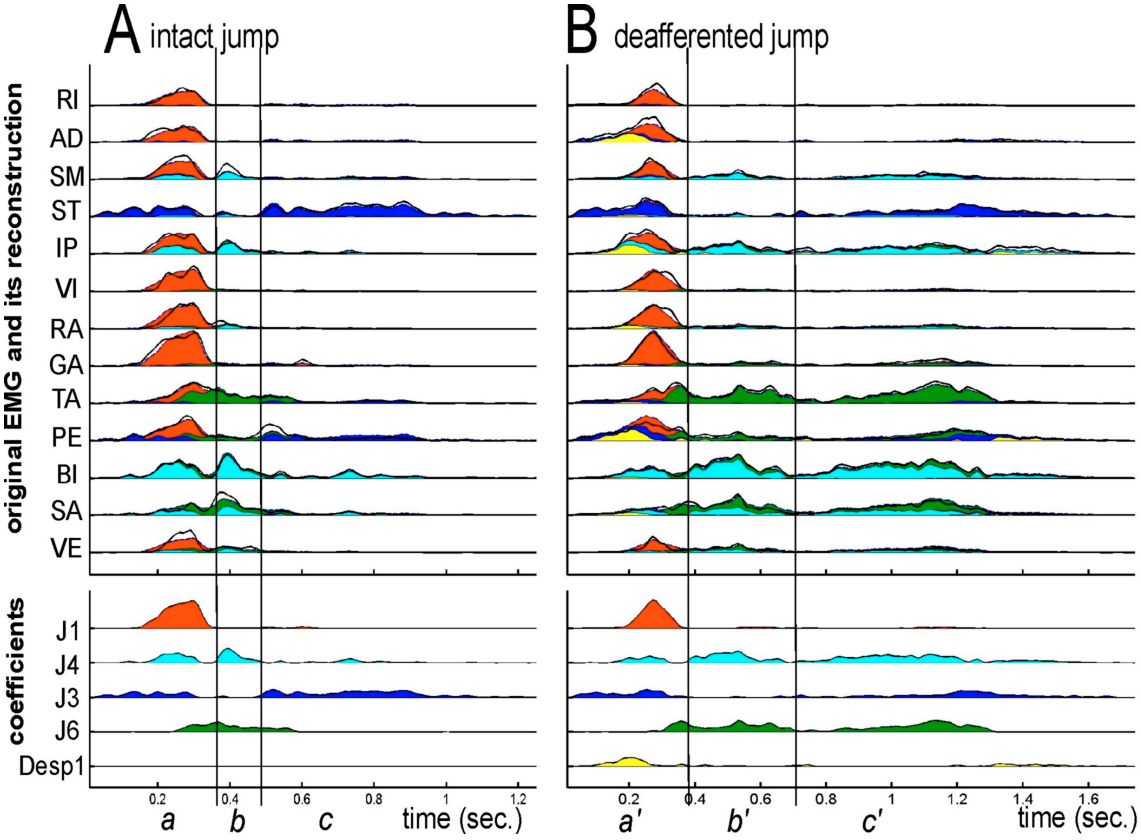


**FIGURE 3.9.** Reconstructing the original EMGs with synergies and their coefficients. The intact and deafferented EMG examples shown in Figs. 3.2C-D are reconstructed using the stage-II synergies extracted from the jumping EMGs of frog 1 (Fig. 3.8). The original EMG data, filtered and integrated (see Materials and Methods for filtering and integration parameters), is shown in thick black lines, and the time varying coefficients of the synergies are shown below the EMGs. The reconstruction of the motor pattern is superimposed onto the original EMGs. The colors composing the reconstruction match the colors of the coefficients such that the colors reflect the respective contribution of each synergy to the reconstruction at each time point. Note that synergy Desp1 (yellow) is deafferented-specific; thus, by definition, it contributes to the reconstruction of only the deafferented EMG episode. See Results for more discussion.

## Effects of deafferentation on the activation of synergies

### Reconstructing EMG data with synergies and their coefficients.

The results of the previous two sections show that for both swimming and jumping, there is a large degree of sharing between synergies before and after deafferentation.

However, as can be seen in Fig. 3.2, there were also substantial changes in the EMGs observed following deafferentation. We therefore investigated how such EMG alterations were produced by examining patterns of synergy activation coefficients used to reconstruct the observed EMGs before and after deafferentation. In Fig. 3.9, the jumping EMG examples shown in Fig. 3.2 are reconstructed from the jumping synergies of frog 1 (Fig. 3.8). We see that activation of SM, IP, BI and SA in phase *c'*, as noted earlier, is explained by prolonged activation of synergy J4 (light blue) in the deafferented example. The increased amplitude and duration of TA and PE after deafferentation, on the other hand, are explained by a prolonged and increased activation of synergy J6 (green) in phase *c'* as compared with phase *c*. Also, the altered relative onset times of AD, ST, IP, and PE in phase *a'* is accounted for by the deafferented-specific synergy (yellow). The examples in Fig. 3.9 therefore suggest that the altered EMG patterns after deafferentation can be characterized by changes in the amplitude and temporal patterns of the shared synergy coefficients, and to a lesser extent, by the data set-specific synergies.

**Deafferentation alters both the amplitude and temporal patterns of synergy activation.**

We proceeded to systematically analyze effects of deafferentation on both the amplitude and temporal patterns of the synergy coefficients.

The percent changes of the extension and flexion peak amplitudes of the different classes of synergies after deafferentation are summarized in the left half of Table 3.2. For the extension synergies (S1, S2, J1, and J2), deafferentation had a much more pronounced effect on the jumping synergies (J1, J2) than on the swimming synergies (S1, S2). As summarized in Table 3.2, for three of the four frogs, there was a 25-44% decrease in the extension peak amplitude of J1 after deafferentation. By contrast, the extension peak amplitude of S1 for frogs 1 and 2, as well as that of S2 for frogs 1, 3, and 4, were not altered by deafferentation. One explanation for this difference is that sensory feedback plays a much more important role in reinforcing the activation of jumping extension synergies than that of the swimming extension synergies. While other interpretations (such as muscle fatigue) are possible, we think that the above interpretation is likely because it makes biomechanical sense (see Discussion). We speculate that the exceptional increase in S1 extension amplitude for frog 4 (Table 3.2) might be due to a more-than-usual denervation supersensitivity to inputs in the spinal interneurons or motoneurons induced by our surgical procedure.

**TABLE 3.2. Effects of deafferentation on the amplitude and temporal patterns of synergy coefficients.** Changes in coefficient peak amplitude and coefficient burst duration after deafferentation for both the extension and flexion phases were quantified as percent changes. Instances for which the null hypothesis that the intact and deafferented means are the same cannot be rejected (t-test; $p > 0.05$) are marked with NC, standing for no change. The abbreviation na, standing for not available, means that the synergy was not activated during that particular phase. Insp and Desp stand for intact- and deafferented-specific synergies, respectively. See Materials and Methods for how burst duration was determined.

| Synergy | Frog | ext. peak amp. (% change) | flex. peak amp. (% change) | ext. burst duration (% change) | flex. burst duration (% change) |
|---|---|---|---|---|---|
| S1 | frog 1 | NC | na | NC | na |
| | frog 2 | NC | na | -14.9 | na |
| | frog 3 | -42.4 | na | +38.3 | na |
| | frog 4 | +266.7 | na | NC | na |
| S2 | frog 1 | NC | na | +29.0 | na |
| | frog 3 | NC | na | NC | na |
| | frog 4 | NC | na | -27.6 | na |
| S3 | frog 1 | Insp | Insp | Insp | Insp |
| | frog 2 | -42.3 | -65.2 | NC | NC |
| | frog 3 | +79.4 | NC | +15.8 | -19.4 |
| | frog 4 | +68.9 | NC | -61.4 | -50.1 |
| S4 | frog 1 | NC | +115.1 | NC | NC |
| | frog 2 | -28.6 | NC | -17.7 | NC |
| | frog 4 | Insp | na | Insp | na |
| S5 | frog 1 | Insp | Insp | Insp | Insp |
| | frog 2 | -24.1 | -29.6 | NC | NC |
| S6 | frog 2 | -26.3 | -25.9 | -16.3 | +57.2 |
| | frog 3 | +90.6 | +128.0 | +65.2 | NC |
| J1 | frog 1 | -25.1 | na | -23.8 | na |
| | frog 2 | -39.7 | na | -19.1 | na |
| | frog 3 | -43.7 | na | +25.1 | na |
| | frog 4 | Insp | na | Insp | na |
| J2 | frog 3 | Insp | na | Insp | na |
| | frog 4 | +50.2 | na | -20.2 | na |
| J3 | frog 1 | -33.6 | -51.4 | -14.5 | +24.6 |
| | frog 2 | -57.9 | -59.4 | -34.6 | -60.4 |
| | frog 3 | NC | NC | NC | NC |
| | frog 4 | Insp | Insp | Insp | Insp |
| J4 | frog 1 | -33.8 | -26.3 | NC | +276.9 |
| | frog 2 | na | -37.1 | na | -50.3 |
| | frog 4 | +32.2 | +44.0 | -25.8 | NC |
| J5 | frog 2 | -37.4 | -58.5 | -27.5 | -64.5 |
| | frog 3 | na | +35.7 | na | -57.9 |
| | frog 4 | NC | NC | NC | NC |
| J6 | frog 1 | -22.3 | +22.2 | NC | +69.6 |
| | frog 2 | Desp | Desp | Desp | Desp |

For the non-extension synergies (S3-S6, J3-J6), except S5 and J3, the effects of deafferentation on the peak coefficient amplitude were much less consistent across animals. For instance, while in frog 2 there was a 59% decrease in flexion peak amplitude of J5, in frog 3 this synergy increased by 36%; and in frog 4, the difference between the intact and deafferented means of the same synergy are not statistically significant ($p > 0.05$).

The right half of Table 3.2 summarizes the percent change of coefficient burst duration for both the extension and flexion phases. Again, results across animals tend not to be very consistent. For example, we have seen in Fig. 3.9 that in frog 1, activation of J4 (SM, IP, BI, SA) during the flexion phase was prolonged after deafferentation. Consistent with this observation, our burst duration analysis indicates that on average, there was a 2.8-fold increase in the flexion burst duration for synergy J4 in frog 1. However, for frog 2 a 58% decrease in flexion burst duration was noted for the same synergy, and for frog 4 no change in flexion burst duration was indicated instead. We thus conclude that deafferentation alters the temporal patterns of the synergy coefficients, but for each synergy, individual frogs might rely on sensory feedback differently to sculpt the temporal profile of synergy activation.

**Sensory feedback can uncouple or couple the activation of synergies.**

To investigate the possible roles of feedback in correlating or de-correlating the activations of two synergies, we calculated the Pearson's correlation coefficient ($r$) between the peak coefficient amplitudes of every pair of shared synergies, for each frog, each behavior, each of the extension and flexion phases, and each of the intact and deafferented data sets. We then compared the intact and deafferented $r$'s to assess whether deafferentation causes an increased or decreased correlation between the peak amplitudes of the synergies. An increase in correlation after deafferentation between two synergies would indicate that while activation of each synergy may be modulated by sensory feedback, activation of both may be correlated and coordinated by central mechanisms. On the other hand, a decrease in correlation after deafferentation would indicate that feedback signals play a role in correlating their activation.

Among all pairs of swimming or jumping synergies, we identified 10 pairs whose extension or flexion peak coefficient amplitudes are well correlated under either the intact or deafferented condition ($r \geq 0.6$ and $p < 0.01$), and whose intact $r$ is smaller than the

deafferented *r* ($p < 0.01$). One such pair – J3 and J6 of frog 1 (flexion peak) – is shown in Fig. 3.10A as an example. We see that while the intact flexion peak coefficient amplitudes (+) between the two synergies are not well correlated ($r = 0.3156$, $p < 0.01$), the deafferented peak amplitudes (O) are strongly correlated ($r = 0.6736$, $p < 0.01$). The difference between the intact and deafferented *r*'s in this case is also statistically significant ($p < 0.01$). Thus, sensory feedback may function to uncouple two centrally coupled synergies by modulating activation of each synergy independently (Fig. 3.10B). Note that in Fig. 3.10A, there are 15 intact jumps (+) whose J3 and J6 activation patterns overlap with those of the deafferented jumps, and appear to be correlated much like the deafferented samples. It is possible that in those jumps, feedback signals were gated (Burke, 1999) or were less effective, thereby causing those jump flexion phases to be similar to the deafferented cases.

The other pairs of shared synergies showing a similar increase in correlation coefficient after deafferentation are: S1/S4 (frog 1, extension); S2/S4 (frog 1, extension); S1/*Sh.4* (frog 1, extension); J1/J3 (frog 1, extension); J3/J4 (frog 1; flexion); S1/*Sh.6* (frog 2, extension); S1/S3 (frog 3, extension); S3/*Sh.4* (frog 4, extension); and S2/S3 (frog 4, extension). It is noteworthy that among these 10 pairs of synergies showing an increase in correlation after feedback deprivation, 6 of them involve J3 or S3, both of which possess a prominent ST component (Figs. 3.6 and 3.8). It therefore appears that the two ST synergies are more likely to be uncoupled from other synergies by sensory inflow.

In addition, we found another 4 pairs of shared synergies whose extension peak coefficient amplitudes are correlated under either the intact or deafferented condition ($r \geq 0.6$ and $p < 0.01$), and for which the intact *r* is greater than the deafferented *r* ($p < 0.01$). Frog 3's S1 and S2 (extension peak) belong to one of these pairs (Fig. 3.10C). In this example, the intact and deafferented *r*'s are 0.7065 ($p < 0.01$) and 0.5011 ($p < 0.01$), respectively, and the null hypothesis that the two *r*'s are the same can be rejected ($p < 0.01$). That the deafferented *r* is relatively small suggests that S1 and S2 are controlled as two relatively independent modules by feed-forward commands (Fig. 3.10D), but the high correlation observed under the intact state implies that sensory afferents might help to couple the activation of these two synergies during swimming extension (Fig. 3.10D). Hence, sensory feedback might function to couple two independently organized synergies.

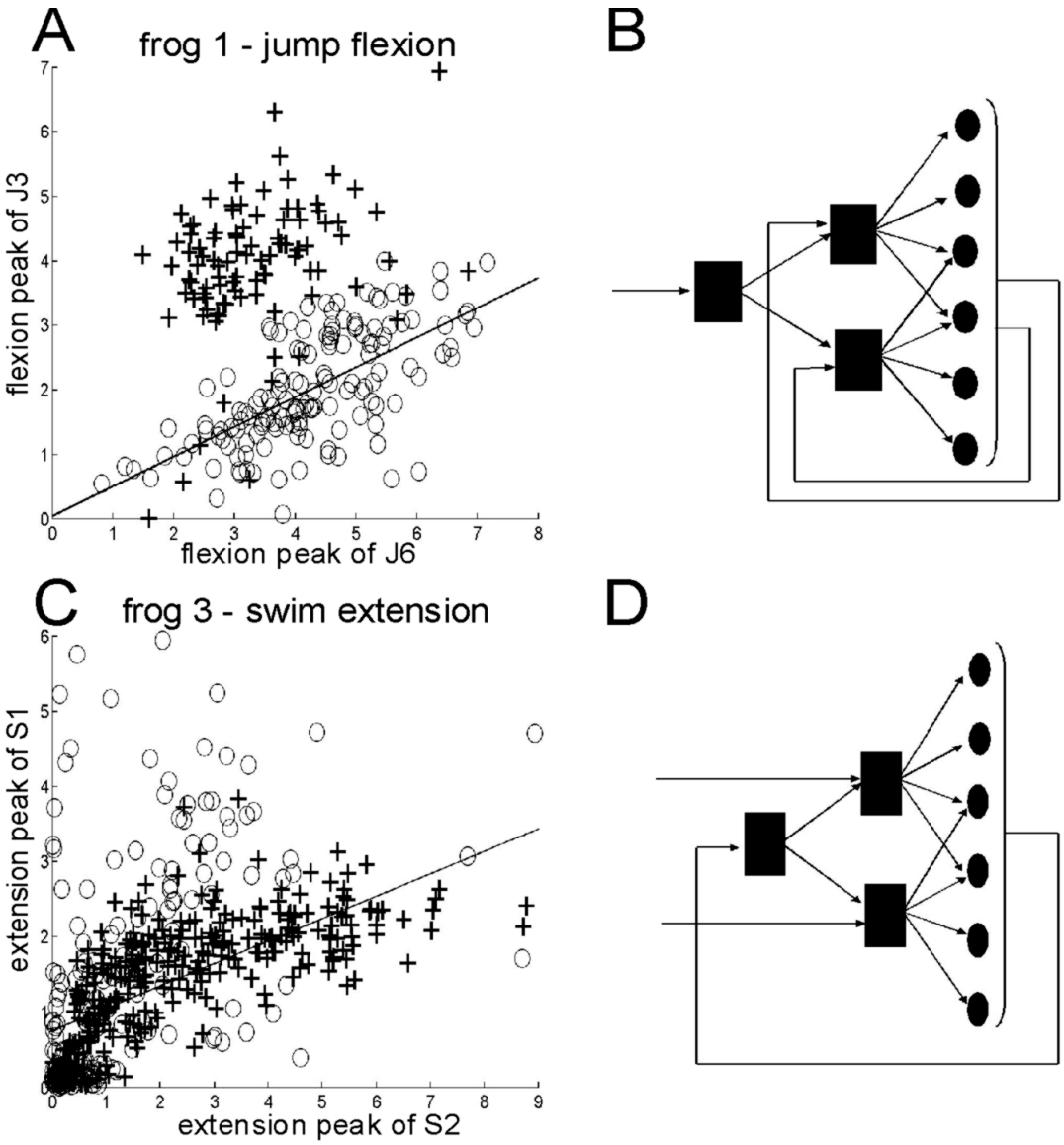


**FIGURE 3.10.** Sensory feedback can uncouple or couple the activation of synergies. We calculated the Pearson's correlation coefficient (*r*) peak coefficient amplitudes of every pair of shared synergies, for each behavior, each of the extension and flexion phases, and each of the intact and deafferented conditions. *A,* The flexion-phase peak coefficient amplitudes of synergies J3 and J6 (frog 1). The intact samples are shown in crosses (+), and the deafferented samples, in circles (O). This is an example of a pair of synergies showing an increase in correlation after deafferentation (intact $r$ = 0.3156; deafferented $r$ = 0.6736). The straight line represents the least-squares fit to the deafferented samples. *B,* Interpretation of the results shown in *A*. Each black square represents a central neuronal network coding for a muscle synergy, or a network coordinating the activation of multiple synergies; each black circle represents the motoneuronal pool of a particular muscle. The finding that the deafferented samples are highly correlated suggest that J3 and J6 (frog 1) are coordinated by central mechanisms upstream of the synergies. On the other hand, the smaller correlation with afferents intact suggests that one or both synergies might be modulated by sensory feedback. See Results for more discussion. *C,* The extension-phase peak coefficient amplitudes of synergies S1 and S2 (frog 3). Again, the intact samples are shown in crosses (+), and the deafferented samples, in circles (O). This is an example of a pair of synergies showing a decrease in correlation after

deafferentation (intact $r = 0.7065$; deafferented $r = 0.5011$). The straight line represents the least-squares fit to the intact samples. *D,* Interpretation of the results shown in *C.* That the deafferented $r$ is relatively small suggests that S1 and S2 are controlled as two relatively independent modules by feed-forward commands, but the high correlation observed under the intact state implies that sensory afferents might help to couple the activation of these two synergies during swimming extension.

The other three pairs of shared synergies showing a similar decrease in correlation coefficient after deafferentation are: S1/S6 (frog 2, extension); J3/J5 (frog 2, extension); and J2/J4 (frog 4, extension).

Finally, we did not observe consistent coupling and uncoupling actions of feedback between the same pairs of synergies across frogs, once again suggesting that the roles of sensory feedback in modifying synergy activation patterns show substantial interanimal variability.

In summary, the results of this section suggest that the differences between the intact and deafferented EMG patterns can be characterized as changes in the amplitude and temporal patterns of the synergy coefficients (Fig. 3.9). Our coefficient analyses further suggest that sensory feedback plays an important role in reinforcing the jumping extension synergy, but not the swimming extension synergies (Table 3.2). For the amplitudes of the non-extension synergies and for the burst duration of the coefficients, effects of deafferentation were not consistent across animals, however (Table 3.2). Finally, our correlation analysis reveals that feedback can either uncouple or couple two centrally organized modules (Fig. 3.10).

## DISCUSSION

In this study, we assess to what extent locomotor EMGs are generated by centrally organized muscle synergies. For both swimming and jumping, we established that EMGs before and after deafferentation possess similar low dimensionalities (stage I), and that most synergies were preserved after feedback deprivation (stage II). Deafferentation also altered the amplitude and temporal patterns of activation of the shared synergies.

### Muscle synergies as centrally organized modules.

The main finding of this study is that both intact and deafferented behaviors are primarily generated by the same set of synergies. Therefore, most, but not all, of the muscle

synergies underlying frog locomotor behaviors are centrally organized modules activated by spinal and/or supraspinal commands. Such a result is similar to previous observations of invariant structures after deafferentation in the newt (Székely *et al.*, 1969), frog (Loeb *et al.,* 1993; Kargo and Giszter, 2000b), and cat (Grillner and Zangger, 1984; Giuliani and Smith, 1987; Koshland and Smith, 1989).

The present study extends these previous results. By recording EMGs from intact, freely moving animals, we have obtained results that might reflect strategies utilized by the CNS to produce natural behaviors, not just features of the isolated spinal cord or of constrained tasks. By systematic and quantitative analyses of EMGs from a large number of muscles, we have established the sufficiency of a small number of synergies to describe both the intact and deafferented data sets well. Thus, our results support the hypothesis that the CNS simplifies the daunting task of deriving appropriate muscle patterns for many behaviors by flexible combination of a small number of synergies (Tresch *et al.*, 1999; Hart and Giszter, 2004; Ting and Macpherson, 2005). Our findings also validate our means of identifying the synergies: the NMF algorithm would have failed to uncover any shared synergies if there had been a gross mismatch between the assumptions of the algorithm (such as linearity) and our conceptual model of synergy combination.

The observation of invariant synergies also suggests that our synergies may reflect what are commonly referred to as central pattern generators (CPGs), circuitries capable of generating motor patterns without sensory input (Grillner, 1981; Rossignol, 1996; Marder and Bucher, 2001). The finding that combination of synergies can explain our data well and the observation of synergies shared between behaviors (see Results) further suggest that our synergies may correspond to building blocks of the CPGs, originally formulated as a mosaic of "unit burst generators" (Grillner, 1985). Our linear combination model of synergies provides not only an *explicit* formulation of how these building blocks can be combined, but also a means of identifying them. Our model can then be seen as a more general formulation of the unit burst generator hypothesis, in which each 'unit' can consist of muscles acting across different joints, and the interconnected 'units' need not be activated in strict alternation with one another. Such a formulation can include experimentally observed synergies such as the mixed knee extensor-ankle flexor synergy of cat paw-shaking (Smith *et al.*, 1985).

We further speculate that each synergy subserves some basic biomechanical functions (Raasch and Zajac, 1999; Ting *et al.*, 1999; Ting and Macpherson, 2005), such as powering jump extension (Olson and Marsh, 1998), or compensating for interaction torque (Zernicke and Smith, 1996; Gribble and Ostry, 1999). An understanding of the principles guiding the composition of locomotor synergies will require further experimental and modeling studies.

**Afferent roles in synergy activation and organization.**

Although we found that most synergies were preserved after deafferentation, the EMGs themselves were changed (Fig. 3.2), similar to some previous findings that the intact and deafferented muscle patterns could be quite different (Grillner and Zangger, 1984; Hiebert and Pearson, 1999). Our coefficient analyses indicate that such changes could be characterized primarily as alterations in the amplitude and temporal patterns of activation of shared synergies (Fig. 3.9; Table 3.2). Therefore, one important role of feedback might be to shape behaviors by modulating recruitment of centrally organized synergies (Fig. 3.1-A1), consistent with the long-standing hypothesis that motor outputs depend on interactions between the coordinative structures within CPGs, supraspinal commands, and sensory inflow (Grillner, 1981; Clarac, 1991; Prochazka, 1996; Rossignol, 1996; McCrea, 2001).

More specifically, sensory inflow during a behavior might adapt recruitment of synergies to the constraints imposed by the task. For instance, we found that during extension, feedback plays a prominent role in enhancing the activation amplitude of the jumping, but not the swimming synergies (Table 3.2). This difference in the importance of feedback might be due to the different biomechanical demands of the two behaviors. During jump extension, the frog needs to generates more power in order to accelerate the body against gravity within the shortest possible time. Power generation might be enhanced by an increased activation of the Golgi tendon organs and Ib interneurons (due to increased extensor tension caused by the frog's weight being borne solely by the hindlimbs; see Fig. 3.5 of Roberts and Marsh, 2003), assisting in maximal activation of the extensor synergies through a positive feedback loop after Ib input onto the extensor motoneurons is reversed from inhibitory to excitatory (Pearson and Collins, 1993). A similar reflex reversal mechanism is believed to contribute to stance-phase reinforcement of the extensors in the walking cat (Whelan, 1996).

Our analysis of coefficient amplitudes also reveals that feedback uncouples multiple synergies that are centrally organized (Fig. 3.10); therefore, afferents might allow for more individuated control of each synergy. The synergies uncoupled by feedback may have distinct and/or opposing functions. For example, in Fig. 3.10A, while J3 includes the knee flexor ST, J6 comprises TA and PE, whose knee extensor action (Cajigas-González, 2003) may oppose the knee flexor action of J3. Conversely, the synergies coupled by feedback may subserve similar biomechanical functions. Both synergies in Fig. 3.10C, for instance, are synergies of extensors.

Among the ten identified pairs of shared synergies that sensory inflow uncoupled (listed in Results), six of them involve J3 or S3 – two synergies dominated by ST. In the frog, ST is both a knee flexor and a hip extensor (Mai and Lieber, 1990; Kargo and Rome, 2002). That the ST synergies seem more likely to be uncoupled from other synergies by feedback is consistent with the proposal that bifunctional muscles like ST are more susceptible to feedback modulation (Perret and Cabelguen, 1980; Pratt *et al.*, 1996; Ting *et al.*, 2000).

**Synergies specific to intact or deafferented behaviors.**

Besides shared synergies, our algorithm also identified synergies specific to the intact or deafferented data sets. The intact-specific synergies may represent CNS modules accessible only by feedback (Fig. 3.1-A2), functioning to compensate for perturbations (Forssberg, 1979; Kargo and Giszter, 2000a). Alternatively, the data set-specific synergies may indicate feedback reorganization of the CNS neuronal assemblies (Pearson, 2004): i.e., the specific synergies reflect the difference between the networks activated under the intact and deafferented conditions (Fig. 3.1-A4). For frogs 3 and 4, the observation that some of the specific and shared synergies involve the same set of muscles, but in different balances (see Fig. 3.8 and Results) suggests that some centrally activated synergies may serve only as templates for motor output generation; activities of individual muscles within those synergies might then be fine-tuned by feedback (Fig. 3.1-A3) (Pearson, 2000). Finally, the possibility of the non-shared synergies being consequences of neuronal plasticity (Goldberger, 1988) cannot be excluded.

**Interanimal variability of feedback actions.**

We have seen that the roles of sensory feedback in modulating the amplitude and temporal patterns of each synergy may vary between animals (Table 3.2), suggesting that how feedback sculpts the activation pattern of each synergy may depend on the prior experiences of each animal. Such a possibility is supported by the proposal that the reflex gain of the rat withdrawal reflex system may be fine-tuned in an experience-dependent manner (Schouenborg, 2002). Also, the architectural heterogeneity of the musculature across animals may necessitate individually tailored recruitment of certain muscles (Loeb, 1993).

**A novel method of identifying common and specific structures.**

Another contribution of this study is our method of exploiting the NMF algorithm to search for shared and specific structures from multiple data sets, introduced in our stage-II analysis. While our stage-I method of applying the algorithm to each data set separately is an obvious way to search for shared and specific synergies (d'Avella *et al.*, 2003; Hart and Giszter, 2004), it has several limitations (see Methods). Our stage-II method overcomes these limitations by taking information from all data sets into consideration. We have focused on using this method to find commonalities and differences between the intact and deafferented data sets, but the same methodology can be extended to extract synergies shared between behaviors (d'Avella and Bizzi, 2005), preparations, or animals.

Almost a century ago, Brown (1911) proposed that "intrinsic factors" within the spinal cord are responsible for generating motor outputs for locomotion. In light of Bernstein's (1967) problem, we propose that a small number of centrally organized muscle synergies, activated by central commands but regulated by sensory inflow, plays a predominant role in the generation of complex, high-dimensional motor patterns for natural behaviors.

*Chapter 4*

# Sensory modulation of muscle synergies for motor adaptation

## INTRODUCTION

In the past several years, there has been a flood of interest within the movement control community in the idea that, organizing the motor system into modules could be a way for the CNS to circumvent the difficulty of controlling many degrees of freedom (Bernstein, 1967). As reviewed in Flash and Hochner (2005), a module, or motor primitive, can be formulated at different levels of the motor system hierarchy, from the behavioral, the kinematic, the muscle, to the neural levels. Here, we focus on how modules at the muscle level are represented, and how they are utilized by the CNS as functional units of activation for motor execution. Many recent studies have provided evidence suggesting that a module at the muscle level can be represented as a muscle synergy, defined as a static activation profile across many muscles, and activated by a time-varying activation coefficient (Tresch *et al.*, 1999; Saltiel *et al.*, 2001; Hart and Giszter, 2004; d'Avella and Bizzi, 2005; Ting and Macpherson, 2005; Tresch *et al.*, 2006). A number of authors have hypothesized that each synergy can be regarded as a low-level feed-forward controller (d'Avella *et al.*, 2006) responsible for producing a torque pattern that can be related to global biomechanical (Torres-Oviedo *et al.*, 2006) or kinematic (d'Avella *et al.*, 2003; Cajigas-González, 2003) variables. Other studies have also argued that a small number of synergies are responsible for constructing the muscle patterns underlying natural motor behaviors (d'Avella, 2000; Cheung *et al.*, 2005; Cappellini *et al.*, 2006).

Whether such a motor control scheme comprising a small number of synergies is compatible with the bewildering capacity of the motor system to compensate for diverse perturbations has remained an open question. While the intrinsic viscoelastic properties of the musculoskeletal apparatus could contribute to perturbation compensation (Bizzi *et al.*, 1992), neural compensation activated by altered sensory stimuli no doubt also plays a critical role in generating compensatory responses (as reviewed in Rossignol *et al.*, 2006). Muscle patterns associated with perturbation compensation can conceivably be generated by modulating the activation pattern of the very same set of synergies used for constructing normal, natural behaviors. Alternatively, compensatory responses might result from built-in corrective patterns organized as centrally encoded synergies but accessible only by sensory afferents, similar to the corrective force fields observed in the frog (Kargo and Giszter, 2000a) or the stumbling corrective reaction in the cat (Forssberg, 1979). A third possibility

is that adaptive muscle patterns are generated by tuning the activations of individual muscles through monosynaptic and/or multisynaptic reflexes; in such a model, synergies are either structures encoded by networks not accessible by sensory afferents, or just mathematical representations of an epiphenomenon contingent upon the specific tasks performed under a specific dynamic condition (Pearson, 2000). It remains unclear which of the above three possibilities underlies the generation of motor patterns for immediate adaptive responses elicited upon limb perturbation.

Recently, Cheung *et al.* (2005) reported that most of the muscle synergies underlying frog locomotor behaviors were observed even after deafferentation; yet, the time-varying activation profile for some of those synergies were altered after removal of sensory feedback, suggesting that many of the synergies underlying natural motor behaviors might be centrally organized structures modulated by sensory afferent signals. These results motivated us to hypothesize that, compensatory muscle patterns observed upon limb perturbations can be generated by modulating the activation pattern of the set of synergies normally used for movement construction. More specifically, this hypothesis predicts that, muscle synergies are structures robust across different dynamic conditions, and that, EMG changes associated with limb perturbations can be explained as alterations in the temporal activation profile of a set of invariant synergies.

In this study, we test the above hypothesis by perturbing the hindlimb of the frog during four natural behaviors, including jumping, stepping, kicking, and swimming. Electromyogram (EMG) data from 13 hindlimb muscles were collected before, during, and after two different types of perturbation involving an additional inertial load and an elastic load to the limb, respectively. We further developed a novel algorithm based on the non-negative matrix factorization method (Lee and Seung, 1999) capable of simultaneously extracting synergies shared by all unloaded and loaded conditions as well as synergies specific to one or multiple conditions. Our results are in general consistent with our hypothesis that sensory modulation of centrally encoded synergies can be a mechanism underlying immediate or short-term motor adaptation (Pearson, 2000), though in the Discussion section we will also describe several interesting exceptions that can be explained only by a more elaborate model of synergy control.

## MATERIALS AND METHODS

### Surgical procedure

Three adult bullfrogs (*Rana catesbeiana*, ~240g) supplied by Connecticut Valley Biological (Southampton, MA; frog 1) and Rana Ranch Bullfrog Farm (Twin Falls, ID; frogs 2-3) were studied. Before all surgeries, the frog was anesthetized with ice, and tricaine (ethyl 3-aminobenzoate methanesulfonate, 0.1 mg/g; Sigma, St. Louis, MO) injected into the left iliac sac. Bipolar EMG electrodes made of teflon-coated stainless steel wires (A-M Systems, Carlsborg, WA) and wax were implanted into the following muscles in the right hindlimb (nomenclature: Ecker, 1971): rectus internus major (RI), adductor magnus (AD), semimembranosus (SM), semitendinosus (ST), iliopsoas (IP), vastus internus (VI), rectus femoris anticus (RA), gastrocnemius (GA), tibialis anticus (TA), peroneus (PE), biceps (or iliofibularis) (BI), sartorius (SA), and vastus externus (VE). The EMG wires were routed subcutaneously to the frog's back, and attached to a 37-pin d-sub connector through crimped pins on the connector. Insulation of each EMG wire was provided, first by sealing each crimp contact with wax after the pin was locked into the connector, and then, by applying a thin layer of epoxy (Devcon, Riviera Beach, FL) across all pins. Subsequently, the position of the connector was stabilized onto the frog's back by suturing the skin incisions around the connector tightly, and by gluing the connector to a custom-made plastic platform, which in turn was attached to the back skin of the frog by Nexaband glue (Veterinary Products Laboratories, Phoenix, AZ). After the surgery, the frog was allowed at least one day for recovery.

For frog 3, an additional surgery was performed to install an additional elastic load to the frog's hindlimb (see below).

### Experimental procedure and delivery of perturbation

Patterns of EMG and kinematics during unrestrained terrestrial behaviors (jumping, stepping, and kicking; frogs 1 and 3) performed in an arena, and aquatic behaviors (in-phase and out-of-phase swimming; frog 2) performed in a tank, were acquired during within-day experimental sessions spread over 7-8 days (frog 1, 4 sessions; frog 2, 5 sessions; frog 3, 6 sessions). In each session, 3-8 trials of data collection, each lasting approximately 10 minutes, were performed. Between trials, the frog was allowed at least 15 minutes of rest to

prevent muscle fatigue. During the arena trials, positions of the acetabulum, knee, and ankle on the dorsal limb were marked by Wite-Out correction fluid (Milford, CT) to facilitate kinematics extraction (see also, "Recording kinematics" below). During all swimming trials, additional insulation of the connector against water was provided by removable light-bodied Permlastic (Kerr USA, Romulus, MI). All movements were video-taped by a digital video camera (Sony DCR-HC46, 29.97 frames/s).

Effects of increasing the limb inertial load on the EMGs were studied in frogs 1 and 2. A weight made of malleable lead was attached to a strap by Elastikon tape (Johnson and Johnson, New Brunswick, NJ). The strap, made of double-layer vinyl electrical tape (7 mil; United Tape, Cumming, GA), was in turn attached to two pieces of industrial strength velcro. In the loaded experimental trials, the weight was attached to the anterior half of the right calf by wrapping the strap around the calf with the strap's position secured by velcro. The load was positioned carefully so that it did not physically obstruct the motion of any joint.

In order to ensure that the EMG changes associated with loading were repeatable and reversible, the load was applied, and then taken off, several times. In frog 1, the same weight (25.9 g, 55% of limb's weight) was applied three times, in sessions 2, 3, and 4, respectively, during terrestrial behaviors. In frog 2, the weight (27.5 g, 85% of hindlimb's weight) was applied two times, in sessions 2 and 3, respectively, during aquatic behaviors. In each of these sessions, data were collected before, during, and after load application.

Effects of elastic loading on the EMGs were studied in frogs 2 and 3. Inspired by a procedure first described by Bouyer (Wolpaw *et al.*, 2006), the elastic load was delivered through a rubber band (Alliance Rubber Band Company, Hot Springs, AR) attached to a strap made of double-layer vinyl tape. In the loaded experimental trials, the rubber band was attached proximally to one end of the EMG connector by a screw, and distally, to either of two different positions of the frog's limb: the posterior end of the calf near the ankle (frogs 2 and 3; Fig. 4.1B, right), or to the thigh near the knee (frog 3; Fig. 4.1B, left). The former configuration affects the motion of both the hip and knee joints directly, and the latter, motion of the hip joint only. This distal attachment was accomplished by wrapping the strap around the limb, with the wrapping secured either by velcro (frog 2; and frog 3, thigh attachment), or by suturing the strap to the skin over a surgery (frog 3, ankle attachment).

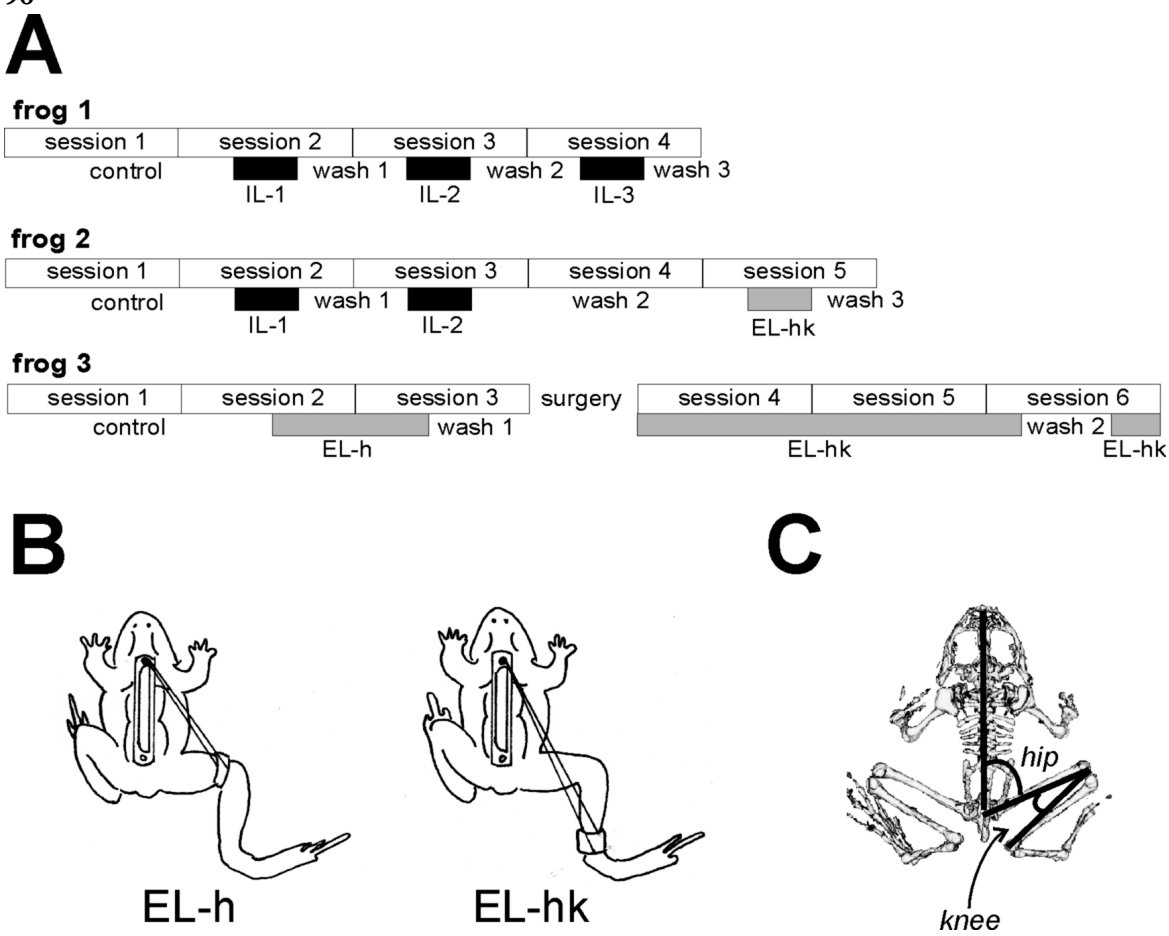


**FIGURE 4.1.** Experimental procedure for inertial loading and elastic loading experiments. *A*, Three frogs were studied. In frog 1, the same inertial load (IL) was wrapped around the frog's right calf 3 times over 4 sessions during terrestrial behaviors. In frog 2, an inertial load was first applied 2 times, followed by an application of an elastic load (EL-hk). Only aquatic behaviors were studied in this frog. In frog 3, 2 different elastic loads (EL-h and EL-hk) were used to perturb the hindlimb during terrestrial behaviors. *B,* Two different elastic loading types were studied. In the first type (EL-h), the rubber band was attached distally to the knee, thus affecting hip joint motion directly. In the second type (EL-hk), the rubber band was attached distally to the ankle, affecting both hip and knee joint motion directly. *C*, Definition of hip joint and knee joint angles in this thesis chapter. The hip joint angle is defined as the angle between the body axis and the thigh, and the knee angle, that between the thigh and the calf.

In frog 2, the elastic load to the ankle (Fig. 4.1B, right) was applied in experimental session 5 through a rubber band with spring constant = 52.92 N $m^{-1}$. Data during aquatic behaviors were collected before, during, and after load application. In frog 3, the elastic load was first applied to the knee (Fig. 4.1B, left) (spring constant = 46.06 N $m^{-1}$). Load application began in session 2, and continued over to the first half of session 3. After session 3, the elastic load was applied to the ankle through another rubber band (60.76 N $m^{-1}$), distally sutured to the skin near the ankle over a surgery. Data of the loaded, terrestrial

behaviors were collected over sessions 4, 5, and 6. In one trial of session 5, an incline with a slope of $14.5^0$ was installed in the arena for studying uphill and downhill stepping under the loaded condition. In one trial of session 6, the rubber band was temporarily taken off for recording washout data. In all frogs, the load did not change the resting posture significantly.

The experimental schedule of the three frogs is summarized in Fig. 4.1A. All procedures were approved by the Massachusetts Institute of Technology Committee on Animal Care before experimentation.

**Recording kinematics**

Video episodes of the different behaviors were captured and digitized as avi files using the software Adobe Premiere (version 6.0). Each frame in the video files was deinterlaced into its upper and lower fields using a custom software written in Matlab (Math-Works, Natick, MA), and the positions of the body axis, acetabulum, knee, and ankle were marked manually on individual video fields using a Matlab graphical user interface. Assuming a planar motion of the frog hindlimb, time sequences of hip and knee joint angles (59.64 Hz) were computed from the marker positions extracted from the video fields.

**EMG data preprocessing and normalization**

Electromyographical (EMG) signals were amplified (gain of 10,000), band-passed filtered (10-1000 Hz) through differential alternating current amplifiers, and digitized (1000 Hz). Using a custom Matlab software, the EMG traces were then manually parsed into segments, each containing the EMG of a single behavioral episode. These episodes were then categorized into different behaviors according to their corresponding video records. The parsed data were then high-passed filtered [window-based finite impulse response (FIR) filter; $50^{th}$ order; cutoff of 50 Hz] to remove motion artifacts, rectified, low-passed filtered (FIR; $50^{th}$ order; 20 Hz) to remove noise, and integrated over 10 ms intervals to capture the envelope of EMG activity.

After integration, the EMG of each muscle was normalized to the maximum EMG value of each muscle recorded in each frog to account for electrode pickup differences across muscles. Then, for each behavior, the variance of each muscle in the data set was

normalized to one, so that the results of the muscle synergy extraction algorithm used in subsequent analyses will not be biased into describing only these muscles with high variance.

**Frog motor behaviors examined and initial EMG characterization**

For each perturbation type, we studied EMGs collected from jumping, stepping, kicking, and swimming. The kicking EMGs included caudal, lateral, and caudal-lateral kicks, and the swimming EMGs included both in-phase and out-of-phase swimming cycles. In all subsequent analyses, EMGs from different behaviors were never pooled together as a joint data set; thus, all muscle synergies extracted (extraction procedure to be described below) were specific only to one behavior, but not necessarily to one condition, as will be described below.

Before extracting muscle synergies, we also characterized how the muscle patterns were altered by loading by comparing both the peak amplitude and duration of the EMG bursts across conditions. The onset and offset times of the activation bursts of the rectified and integrated EMG were detected as follows. First, for each experimental session, and for each muscle, all EMG data points with amplitude exceeding 5% of the maximum EMG amplitude obtained in that muscle during that session were isolated. Any continuous segment of isolated data points was considered to be an activation burst. Calculating this 5% threshold with respect to the session maximum was necessary to account for small fluctuation of EMG amplitude across experimental sessions. Then, for any two bursts within the same EMG episode, if the time difference between the onset of the later burst and the offset of the earlier burst was smaller than 20ms for jump and kick, or 50ms for step and swim, the two bursts were combined into one. Finally, any burst with duration smaller than 40ms for jump and kick, or 100ms for step and swim, were excluded from further analysis.

**The muscle synergy model and two stages of analyses**

A major goal of this study is to characterize the changes in EMG pattern associated with an additional inertial or elastic load to the limb. To this end, for each behavior of each frog, we partitioned the whole data set into data subsets, each comprising data episodes collected under the same condition. For frog 1, there were 7 such conditions: control, inertial load 1 (IL1), wash1, IL2, wash2, IL3, and wash3 (IL1 refers to the first application of

the weight, and IL2, the second application of the same weight, and so on). For frog 2, there were also 7 conditions: control, IL1, wash1, IL2, wash2, hip-knee elastic load (EL-hk) (Fig. 4.1B, right), and wash3. For frog 3, owing to the unequal amount of data collected across sessions, we partitioned the data set into 5 conditions as follows: control, hip elastic-load (EL-h) (Fig. 4.1B, left), wash (including wash1 and wash2), EL-hk from session 4, and EL-hk from sessions 5 and 6.

As in pervious studies (Tresch *et al.* 1999; Saltiel *et al.*, 2001; Cheung *et al.*, 2005), we modeled EMGs collected under different conditions as the linear combination of a set of muscle synergies, each represented as an activation balance profile across the 13 recorded muscles, and activated by a time-varying activation coefficient. In matrix notation, we denote the synergy vectors by $W$, and the time-varying coefficients, by $C$, so that

$$D = WC, \tag{4.1}$$

where $D$ is the EMG data matrix. We used the non-negative matrix factorization (NMF) algorithm (Lee and Seung, 1999, 2001) to extract muscle synergies from each behavioral condition, and then, assessed to what extent the load-associated EMG changes can be described as changes in muscle synergies, or changes in the activation coefficients of invariant synergies. To accomplish this assessment systematically, we divided our analyses into two stages, similar to the analytic paradigm presented in Cheung *et al.* (2005). In analysis stage I, we extracted synergies from each condition separately to determine the data dimensionality of each condition (see next section); in stage II, we pooled data from all conditions together, and applied a generalized version of the method first described in Cheung *et al.* (2005) to search for synergies shared between multiple conditions, and synergies specific to one or several conditions (see Methods, "Analysis stage II …").

In stage I, after determining the number of synergies underlying the control EMGs, we also fit the control synergies to data of each of the other conditions as a first-pass assessment of the degree of synergy sharing across conditions. This fitting was achieved using NMF with the $W$ matrix set to the control synergies and held fixed across all iterations while the $C$ matrix was being updated. The quality of fit was quantified by $R^2$ values, and high degree of synergy sharing would be indicated by the different conditions having similar and high $R^2$ values.

**Analysis stage I: estimating the number of synergies underlying each condition by separate extractions of muscle synergies**

The major purpose of analysis stage I was to estimate the number of synergies underlying EMGs collected from each condition. This step was necessary, because to initiate the NMF algorithm, the number of synergies describing the data set needs to be specified *a priori*. In several previous studies (d'Avella *et al.*, 2003; Cheung *et al.*; 2005; Tresch *et al.*, 2006), this number is chosen based on plotting the EMG reconstruction $R^2$ or the log-likelihood versus against the number of synergies extracted; the number of synergies corresponding to the point on the curve with maximum curvature is presumed to be the "correct" number of synergies. While this *ad hoc* procedure has been shown to be very robust in simulated data composed of synergies with equal amounts of variance contribution (Tresch *et al.*, 2006), its application in experimental data sets obtained from natural behaviors has remained difficult, because the $R^2$ curves obtained often do not show an unambiguous point with abrupt slope change (e.g., see Cheung *et al.*, 2005, their Figs. 3A and 7A).

Here, we attempt to implement a simpler method, based on estimating the $R^2$-95% confidence interval, to ensure both consistency in choosing the number of synergies across conditions and adequate description of the data at the chosen number. For each condition, we first extracted 1 to 10 synergies using the NMF algorithm without pooling data from different conditions. At each number of synergies, extraction was repeated 20 times, each time with different random matrices (uniformly distributed between 0 and 1) initiating the algorithm. Convergence was defined as having 20 consecutive iterations with a change of $R^2$ <0.01%. After convergence, the 95% confidence interval (C. I.) of the EMG reconstruction $R^2$ was estimated by bootstrapping. The data set of each condition was resampled for 300 times with possible replacement of EMG episodes (i.e., the same EMG episode may appear multiple times in the resampled data set), and after each resampling, the $R^2$ was recalculated. After sorting this set of 300 $R^2$ values from the smallest to the largest, the lower and upper bounds of the 95% C. I. were then estimated to be the $8^{th}$ and $293^{rd}$ $R^2$ values, representing the 2.5 and 97.5 percentiles of the $R^2$ distribution, respectively.

Following synergy extraction and $R^2$-C. I. estimation, we selected the numbers of synergies for each condition by first finding an appropriate number for the control EMGs, and then, using the control $R^2$-C. I. at its chosen number of synergies as a reference $R^2$ interval against which the numbers for the other conditions were chosen. The number of

synergies underlying the control condition was estimated to be the minimum number of synergies at which the extraction repetition yielding the highest $R^2$ has a corresponding C. I.-upper bound >90%. Such a criterion seems to us reasonable, given that in previous studies (d'Avella, 2000; Cheung *et al.*, 2005), most of the $R^2$ curves obtained using NMF plateau to a straight line at ~90%. For the other behavioral conditions, the number of synergies was chosen to be the minimum number of synergies at which at least one of the extraction repetitions yields an $R^2$ whose 95% C. I. overlaps with at least half of the $R^2$-C. I. of the control condition. This criterion guarantees that the EMG data from all conditions are described equally well at their chosen numbers of synergies.

**Analysis stage II: an algorithm for finding shared and specific synergies from an arbitrary number of data sets**

In analysis stage I outlined above, we extracted muscle synergies from each condition separately, allowing us to estimate the data dimensionalities of the different conditions using a procedure based on the $R^2$-C. I. We also fit the control synergies to the data of the other conditions as a first-pass examination of synergy sharing across conditions.

However, interpreting of the stage-I results is difficult. In the fitting procedure, it is expected that the $R^2$ values quantifying the fit between the control synergies and EMGs of the other conditions be smaller than the original control $R^2$, and it is not clear what amount of $R^2$ decrease would indicate significant differences in muscle synergies between conditions. Besides, the synergies separately extracted from each condition might be biased towards peculiarities specific to the data structure of that condition, so that differences between the synergies for different conditions could just be a consequence of the limited data variability available within each condition rather than an indication of changes in synergy composition associated with load application.

Other potential shortcomings of extracting muscle synergies separately from each condition are described in detail in Cheung *et al.* (2005, p. 6422; this thesis, chapter 3).

An obvious alternative to separate extraction is to extract synergies from the data set pooling EMGs of all conditions together. However, in such an approach, no prior information on potential differences in data dimensionalities between conditions is provided to the algorithm, and consequently, the extracted synergies and their corresponding coefficients might describe some conditions better than the other. For instance, suppose

that conditions A and B share 5 synergies, and that in condition B, an additional, new synergy not present in A is activated. Suppose further that 6 synergies were extracted from the data set pooling A and B together. The resulting set of synergies is expected to describe A better, for the additional synergy belonging originally only to B is available to A during extraction for explaining noise; consequently, the synergy composition of this B-specific synergy might also be biased or distorted by any noise structure present in A. Interpreting these extraction results then becomes difficult.

In order to account for these problems, we sought to develop an algorithm that utilizes all available data to maximize the data variability considered during extraction, but at the same time, allows the possibility for any condition-specific synergies to be extracted. Such a possibility has been illustrated in chapter 3 of this thesis (Cheung *et al.*, 2005), and also demonstrated in Ajiboye and Weir (2006). However, the formulation in Cheung *et al.* (2005) was designed for comparing only two data sets whereas here, the focus is to compare synergies across 5-7 different conditions. To achieve such a comparison, we generalize the original formulation of Cheung *et al.* (2005) so that synergies shared by all conditions as well as synergies specific to one or several conditions can be extracted from an arbitrary number of data sets or conditions simultaneously.

The problem to be solved by the generalized algorithm can be understood as follows. Suppose there are $N$ data sets, each representing EMG data collected under a specific condition, and further suppose that there exist a pool of $M$ synergies, $W = \{\vec{w}_1, \vec{w}_2, ..., \vec{w}_M\}$. Each data set is generated by linearly combining an arbitrary subset of synergies selected from the pool, so that each synergy may be activated in one, several, or all of the $N$ data sets. The problem is to find (i) $M$, (ii) the structure of each synergy in the synergy pool, and (iii) the actual synergy selection of each data set, by applying an algorithm to the $N$ data sets. Stating the problem formally, we associate each data set with an index set, $I_d$, comprising $M_d$ unique integers:

$$I_d = \{I_d^{(1)}, I_d^{(2)}, ..., I_d^{(M_d)}\},\ d = 1, ..., N,$$

such that

$$I_d \subseteq \{1, 2, ..., M\}.$$

Denote $I_d^{(q)}$ by $I(d, q)$, $q = 1, \ldots, M_d$. Each data set is then generated by linearly combining a set of $M_d$ synergies, such that

$$\vec{D}_d(t) = \sum_{q=1}^{M_d} c^d_{I(d,q)}(t) \bullet \vec{w}_{I(d,q)}, \qquad (4.2)$$

where $\vec{D}_d(t)$ represents the EMG signal of the $d$th data set for all recorded muscles at time $t$, $\vec{w}_{I(d,q)}$ is the $I(d,q)$th synergy vector in the synergy set $W$, and $c^d_{I(d,q)}(t)$ represents the time-varying activation coefficient at time $t$ associated with the synergy vector. The problem is to estimate $M$, the set of synergies $\{\vec{w}_1, \vec{w}_2, ..., \vec{w}_M\}$, and also, $I_d$, $d = 1, \ldots, N$, by applying the NMF algorithm to the $N$ EMG data sets.

Practically, solving the above problem amounts to finding a synergy pool with the smallest possible number of synergies, and finding, for each synergy in the pool, a selection of data sets in which the synergy is activated, such that all $N$ data sets can be described by their corresponding selections of synergies equally well. Equivalently, the algorithm needs to find, for each synergy in $W$, an index set, $J_q$, $q = 1, \ldots, M$, such that

$$J_q = \{J_q^{(1)}, J_q^{(2)}, ..., J_q^{(N_q)}\}, \quad N_q \leq N,$$

and

$$J_q \subseteq \{1,2,...,N\},$$

where $J_q$ specifies a selection of data sets over which the $q$th synergy in the synergy pool is activated.

As pointed out in Cheung *et al.* (2005), the NMF algorithm can extract synergies with any possible combination of data set selections. As a result of its multiplicative update rules, if the initial estimate of any matrix component is zero, the estimate of that component remains zeros for the rest of the iterations. Thus, to extract a synergy with a specific data set selection, the only necessary manipulation is to set the coefficient components corresponding to those non-selected data sets to zero, enforcing that the synergy is not activated in those data sets. This data set selection, however, needs to be specified independently before the NMF can be initiated.

The algorithm proposed here finds this data set selection for each synergy extracted by choosing the selection that results in the extracted synergies describing all data sets

equally well. It requires two parameters to be specified *a priori*: the number of synergies underlying each data set, which was determined in analysis stage I, and a reference $R^2$ interval for evaluating the goodness-of-fit of the synergies to the data sets at each iteration. Here, this reference $R^2$ interval was set to the 95% C. I. of the control $R^2$ obtained in analysis stage I. This algorithm is an iterative procedure. At each iteration, the data set selection of one synergy is found, and carried over to the next iteration for finding the data set selection of another synergy. It goes through the following steps to identify each synergy and its corresponding data set selection:

*Step 1*: A list of all possible data set selections, excluding those selections containing only one data set, is constructed. Let $S(N,k,a)$ be the $a$th $k$-subset of $\{1,2,\ldots,N\}$. This list, arranged in decreasing degree of sharing across data sets, is stated formally as follows:

$$\begin{aligned}
&S(N,N,1),\\
&S(N,N-1,1),\ldots,S(N,N-1,\binom{N}{N-1}),\\
&S(N,N-2,1),\ldots,S(N,N-2,\binom{N}{N-2}),\\
&\vdots\\
&S(N,2,1),\ldots,S(N,2,\binom{N}{2}).
\end{aligned} \qquad (4.3)$$

*Step 2*: The algorithm starts its first iteration by extracting one synergy shared by multiple data sets together with synergies specific to *each* data set, such that the numbers of synergies reconstructing the data sets (including both shared and specific synergies) match the numbers chosen in analysis stage I. The data set selection for this one shared synergy is chosen from the list in equation (4.3). The first selection in the list is tried first, and after convergence, the 95% C. I. of the $R^2$ value of each data set is calculated. If the C. I.-upper bound of any data set drops below the C. I.-lower bound of the reference $R^2$ interval, indicating unequal description of data sets, then synergies are re-extracted with the second data set selection in equation (4.3) assigned to that one shared synergy. Synergy extraction is repeated, each time choosing the next data set selection in (4.3), until a selection is found to result in equal descriptions of all data sets (as indicated by the $R^2$-C. I. of all data sets overlapping the reference $R^2$-C. I.).

*Step 3*: After the first data set selection for the first shared synergy is found, the reference $R^2$-C. I. is updated to be the $R^2$-C. I. of the control data set computed in the last extraction. This is necessary to account for the fact that as the total number of synergies extracted decreases, the $R^2$ of each data set is also expected to decrease, and thus, the reference enforcing equal descriptions across data sets also needs to be updated to account for the expected $R^2$ decrease. We will describe below another necessary step to prevent drastic decrease of this reference $R^2$ interval over iterations.

*Step 4*: In the second iteration of the algorithm, two shared synergies are extracted. Again, synergies specific to *each* data set are extracted at the same time so that the numbers of synergies for the data sets match those estimated in stage I. The data set selection for the first shared synergy has already been found in the previous iteration, and the appropriate selection for the second shared synergy is found using the procedure described in *step 2*. Thus, in the second iteration and all subsequent iterations, the data set selections found in previous iterations are used in the extraction, and for the new shared synergy, the selections listed in equation (4.3) are tried, one by one, until a selection is found to result in equal descriptions of all data sets (as in *step 2*). From iteration 2 onwards, we also enforced that the data set selection found must give a control $R^2$-C. I. (to be used as a reference $R^2$ interval in the next iteration) which overlaps with the original reference $R^2$-C. I. used in the first iteration. This last criterion is necessary to prevent data set descriptions from becoming successively worse across iterations.

Steps 3 and 4 are repeated until no more shared synergies can further be extracted under the numbers of synergies of the different data sets prescribed in analysis stage I.

Figure 4.2 illustrates this algorithm with a concrete, hypothetical example. See the figure's legend for descriptions and explanations of this example.

In all stage-II extractions, the number of EMG episodes used in each condition was chosen so that all conditions were respectively represented by approximately equal numbers of data points. Each extraction was repeated 20 times, and the repetition with the highest overall $R^2$ was used for $R^2$-C. I. comparison. Convergence criterion was the same as that in analysis stage I.

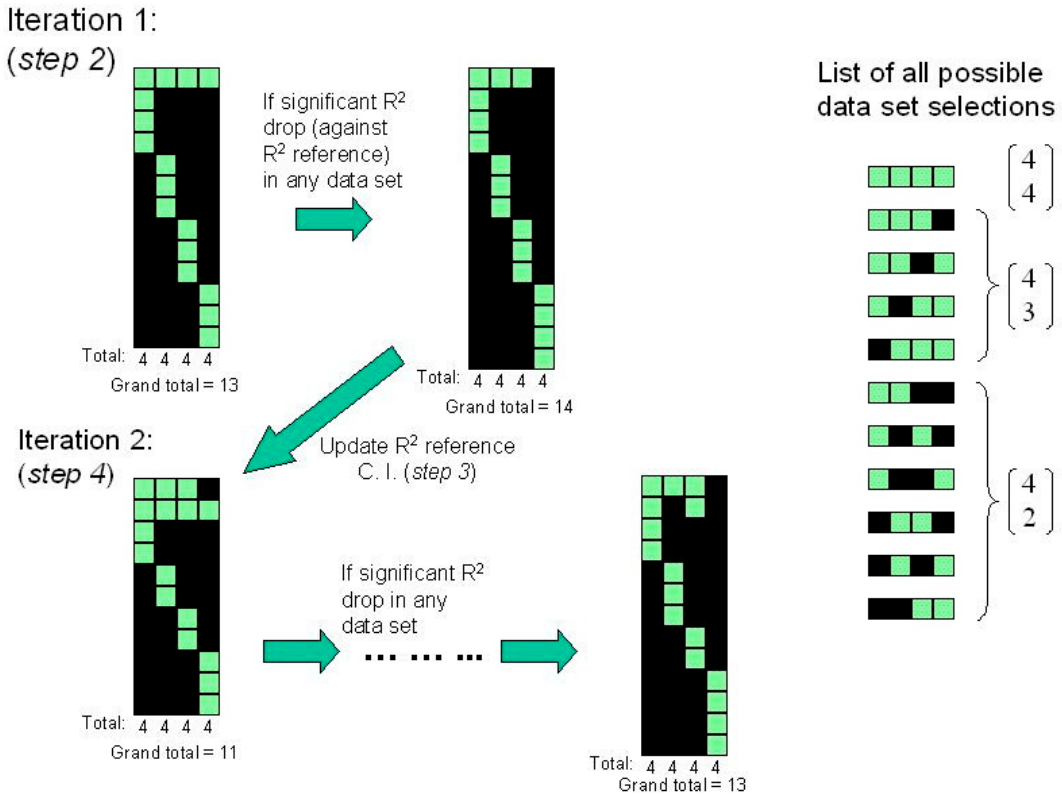


**FIGURE 4.2.** An example illustrating the algorithm used in analysis stage II for finding shared and specific synergies simultaneously from an arbitrary number of data sets. In this example, there are 4 data sets, represented in the figure by a row of 4 square boxes. A black box means that its corresponding data set is not included in a particular data set selection, and a green box if otherwise. In *step 1* of the algorithm, a list of all possible data set selections (excluding those containing only one data set) is constructed. This list, denoted symbolically by equation (4.3) in the text, is graphically represented by rows of boxes on the right side of the figure. The topmost selection ({1,2,3,4}), including all 4 data sets, is the one with the most degree of sharing while the bottom 6 selections ({1,2}, {1,3}, … etc.) are the ones with the least degree of sharing. The left side of the figure shows the data set selection of each synergy extracted in each iteration. Each block of boxes represents an extraction event, with each row denoting the selection of a synergy, and each column, which synergies are relevant to a data set. The total number of synergies for each data set (determined in analysis stage I) is set in this example to be 4, and thus, for each block of boxes, the total number of green boxes along each column is always 4. In the first iteration of the algorithm (*step 2*), extraction starts out by extracting just one shared synergy whose data set selection is chosen to be the first in the list (i.e., {1,2,3,4}). For each data set, an appropriate number of synergies specific just to that data set is included so that the total number for that data set matches the number determined in stage I – in this case, 4. If this set of data set selections results in unequal descriptions of the data sets (as indicated by non-overlapping $R^2$-C. I.'s), then, for the shared synergy, the next data set selection in the list (in this example, {1,2,3}) is tried. Synergies are re-extracted until a data set selection for the shared synergy is found to yield equal descriptions of the 4 data sets (as indicated by overlapping $R^2$-C. I.'s). Suppose that {1,2,3} is such a selection. This data set selection, for the first shared synergy,

is then carried over to all extraction events in the second iteration (*step 4*) during which the same procedure of trying each data set selection in the list on the right for the second shared synergy is carried out. Again, the first selection, {1,2,3,4}, is tried first, and if this does not yield overlapping C.I.'s, then the next is tried. In this example, {1,3} is found to be the right selection for the second shared synergy. As in iteration 1, in iteration 2 (and all subsequent iterations) the total number of synergies for each data set is fixed to be 4. The above-described procedure is then repeated iteratively until no more shared synergies can be extracted.

**Analyzing the activation coefficients of the synergies**

For muscle synergies found to be shared by multiple conditions, we analyzed whether loading changed their patterns of activation by comparing the coefficient time traces [the *C* matrix in equation (4.1)] across conditions. Specifically, we compared the peak amplitude and duration of the activation coefficient bursts of each shared synergy across conditions. The onset and offset times of the coefficient bursts were detected by the same procedure used for detecting EMG bursts (see Methods, "Frog motor behaviors …").

For kicks and jumps, we further divided each episode into two segments, corresponding roughly to the extension and flexion phases, respectively, and isolated bursts within each segment. This parsing was accomplished by a custom graphical user interface written in Matlab. For steps, the extension phase of each cycle was conveniently demarcated by the onset and offset times of each activation burst of muscle AD.

After burst isolation, we compared both the duration and peak amplitude of the bursts of each shared synergy across conditions. For the frogs and behaviors involving inertial loading, in order to account for small day-to-day variations of EMG magnitude, we performed burst comparison after normalizing the burst peak amplitude of each episode with respect to the maximum coefficient amplitude obtained in the session containing that episode. Tests of statistical significance between multiple means were performed using the multiple comparison test function in the statistics toolbox of Matlab ($\alpha = 0.05$; HSD option).

**Clustering muscle synergies of different behaviors**

In order to compare synergies of different behaviors, and to see whether the activations of similar synergies were modulated in a similar way by the same load type, we proceeded to group all extracted synergies into clusters. For each of the two load types, shared and specific synergies of all behaviors were pooled together and grouped into categories by hierarchical cluster analysis (see Johnson and Wichern, 2002, pp. 679-693, for details). In this clustering procedure, we first calculated the Euclidean distance between

every synergy pair in the pooled synergy matrix. Then, using the Matlab function linkage (ward option), a binary hierarchical cluster tree was constructed by linking together synergy pairs that are in close proximity, as indicated by the Euclidean distances calculated. Finally, the cluster tree was divided into clusters using the Matlab function, cluster, which computes, for every link in the cluster tree, an inconsistency coefficient, and then sets those links with inconsistency coefficients greater than a preset threshold as boundaries for cluster division. Here, we used a threshold value of 0.999 for both load types to ensure consistency in determining the number of clusters.

# RESULTS

## Perturbing the limb with an inertial load

In this chapter, we first study how increasing the limb inertia affects motor coordination by recording EMGs of 13 muscles from the right hindlimb before and after loading the limb with a weight wrapped around the frog's calf. In frog 1, the same load was applied three times (IL1, IL2, and IL3; see Fig. 4.1A) during terrestrial behaviors. Electromyogram data (EMG) from 124 jumps (unloaded, 94; loaded, 30), 148 step episodes (94; 54), and 433 defensive kicks (263; 170) were collected over 4 experimental sessions. In IL3 and wash3 of frog 1, only the kick behavior yielded sufficient data for analysis. In frog 2, the load was applied two times during aquatic behaviors; EMGs from 198 swim episodes (141; 57) were collected over 4 experimental sessions (Fig. 4.1A).

### Inertial loading does not significantly change the distributions of jump lengths and kick directions

We first examined how the frog responded to the added inertial load at the behavioral level. Since the frog was not trained to perform each behavior with a specific trajectory prior to perturbation delivery, it is possible, that after loading, the frog adapts by performing each behavior with a different distribution of its varieties (e.g., jumps with shorter distances traversed) in order to attain the same behavioral goal (e.g., escaping from imminent danger). Alternatively, the frog motor system may compensate for the load, through the system's intrinsic mechanical properties and/or altered neural commands, so that in each behavior the distribution of its varieties remains similar after loading. Here, we

investigate which of these two possibilities apply to the frog by comparing the varieties of jump and kick, two non-cyclic motor behaviors, before and after loading.

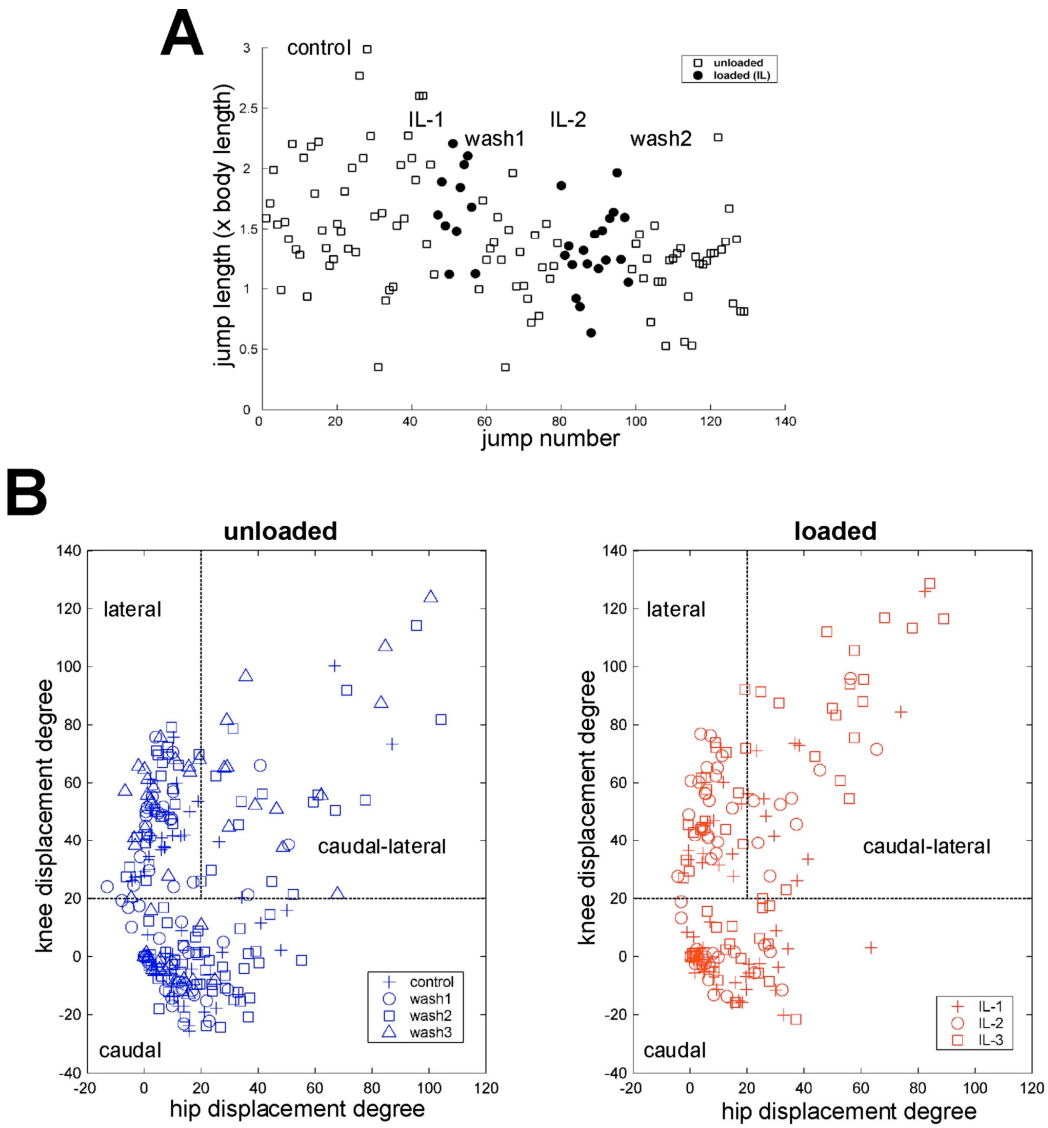


**Figure 4.3.** Variability of jump length and kick direction before and after inertial loading. *A*, The jump length of every jump observed in frog 1 (measured as fraction of the frog's body length) is plotted against jump episode number (#1 means the first jump observed, and #2, the second, and so on). Unloaded jumps, □, and loaded jumps, ●. *B*, Distribution of kick directions before and after inertial loading (frog 1). The kick direction of each kick is defined as the displacement vector from the initial limb position to the maximally extended position during the kick. Under our definitions of hip and knee angles (Fig. 4.1C), the larger the displacement angles, the more extended the limb. The unloaded and loaded kicks are divided into three categories – caudal (knee displacement < 20°), lateral (hip displacement < 20°), and caudal-lateral (all other kicks) – to ease subsequent analyses.

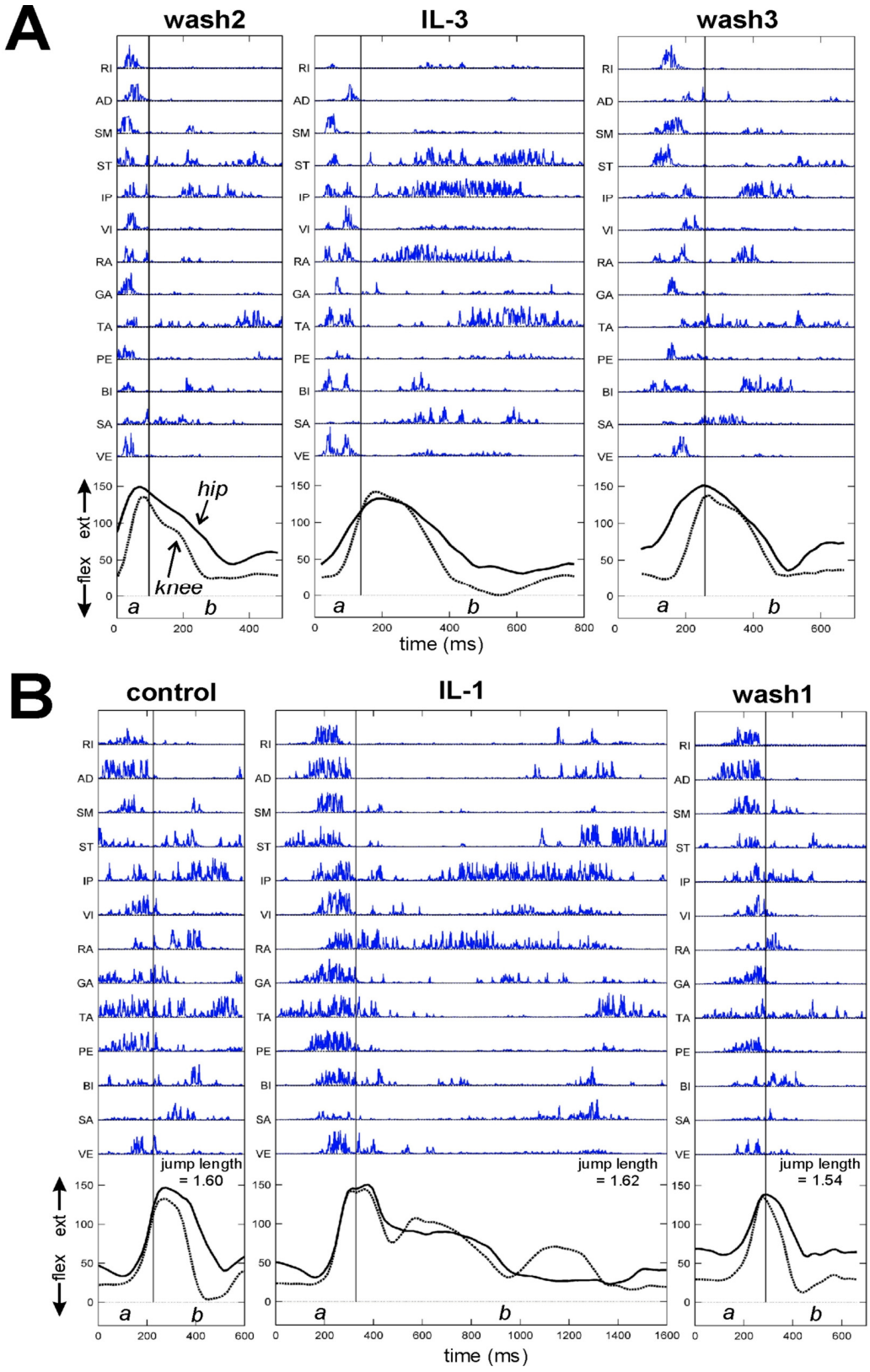


**FIGURE 4.4.** Examples of EMG data and kinematics collected before and after inertial loading. *A*, Three kicking episodes with similar kick directions collected from wash2, IL3, and wash3,

respectively. *B*, Three jumping episodes with similar jump lengths collected from control, IL1, and wash1, respectively. All EMGs displayed here were rectified and high-pass filtered (FIR, 50th order, cutoff = 50Hz) to remove motion artifacts. See Results, "Changes in muscle activation pattern …," for more detailed descriptions of these episodes.

Varieties of jump in each condition was characterized by the distribution of jump lengths, defined, for each jump, as the distance between the initial and final positions of the frog's snout. As shown in Fig. 4.3A, it is evident that inertial loading did not change the distribution of jump lengths despite that there was a noticeable, but small, trend of decreasing jump length over time. This suggests that the frog motor system is capable of adapting to the added weight to achieve the same distribution of jump lengths in the perturbed conditions.

We then proceeded to characterize kick varieties of the loaded and unloaded conditions by plotting their distributions of kick directions. The kick direction of each kick is defined as the displacement vector from the initial limb position to the maximally extended position during the kick. As shown in Fig. 4.3B, the kick direction distribution of the unloaded conditions (control, wash1, wash2, and wash3) is very similar to that of the loaded conditions (IL1, IL2, and IL3). Thus, like jumping, in kicking the frog is able to compensate for the load to achieve the same distribution of kick varieties.

The results shown in Fig. 4.3 support that any load-associated changes in muscle activation pattern are likely to reflect adaptive responses for load compensation rather than shifts in the repertoire of each behavior induced by the perturbation. In the next section, we shall systematically compare, for each behavior, the EMGs across the different conditions to reveal any reversible and repeatable changes in muscle pattern associated with the added inertial load.

**Changes in muscle activation pattern associated with inertial loading: visual inspection of EMG data**

Shown in Fig. 4.4A are EMGs of three kicks with similar kick directions taken from wash2, IL3, and wash3, respectively. For ease of visual inspection and subsequent analyses, each kick is divided into two phases, labeled *a* and *b*, roughly corresponding to the extension and flexion phases of each kick, respectively. We notice that while phase *a* of the loaded kick (IL3) is reasonably similar to those of the unloaded kicks (wash2 and wash3), the loaded

phase *b* is noticeably different from those of the unloaded kicks. In particular, in the loaded kick the duration of the ST, IP, RA, TA and SA bursts in phase *b* are much longer than those in phase *b* of the unloaded examples (Fig. 4.4A). However, in all three kicks, the order of burst appearance in phase *b* seems to remain invariant: activations of ST, IP, RA, BI, and SA are followed by a prominent burst of TA. In phase *b* of all three examples, the IP burst also tends to be coactive with the RA burst, and the TA burst, with the ST burst. Together, these observations point to the possibility that the differences between the loaded and unloaded EMGs can be described as altered activations of invariant muscle groupings, or muscle synergies. Also, the fact that the wash2 and wash3 examples are similar suggest that the EMG changes seen in the loaded example are reversible after load removal, further supporting that those EMG changes are related to load compensation.

The EMGs of three different jumps with similar jump lengths, taken from control, IL1, and wash1, respectively, are shown in Fig. 4.4B. Specifically, the IL1 jumping example shown was the first loaded jump observed in the animal (frog 1). As in the kicking examples, each jump is divided into two phases, *a* and *b*, for ease of inspection and subsequent analyses. Again, the most dramatic difference between the loaded and unloaded EMG patterns occurs in phase *b*: the duration of the IP, RA, and SA bursts in the IL1 example are much longer than their corresponding bursts in the control and wash1 examples. At the same time, despite these differences, in phase *b* there still seem to be muscle co-activation patterns preserved across the three examples: for instance, IP is co-active with RA and BI; TA, with ST; and RA, with SA. Thus, as in the kicking examples (Fig. 4.4A), such EMG differences might possibly be described as altered, but reversible, activations of synergies shared across conditions. Notice also that muscles AD and RI, while active in phase *b* of the loaded jump, were not activated in phase *b* of the two unloaded jumps, raising the possibility that there might be muscle groupings specific to the loaded conditions. We note also that the EMG changes seen in the loaded example were accompanied by slower hip flexion [consistent with observations of decreased limb velocity upon inertial loading reported in, e.g., Happee (1993) and Gottlieb (1996)] as well as exaggerated knee extension.

In Fig. 4.4B, since the loaded EMG presented was recorded during the first jump the animal performed after loading, the EMG alterations seen in the loaded jump represent immediate responses of the motor system to the increased limb inertia, triggered by altered

sensory stimuli, rather than new motor patterns that emerge gradually. This is further illustrated by the EMGs of a swimming episode collected from frog 2 after loading (Fig. 4.5). In this example, there are 5 consecutive swimming cycles, demarcated in the figure by dotted vertical lines. As cycle 4 began, the weight attached to the calf accidentally (or fortuitously) fell off the limb (arrow in figure). Comparing the EMG patterns in cycles 3 and 4, we see that upon load detachment, the prominent bursts of RI, AD, and SM activated towards to the end of cycles 2 and 3 disappeared almost totally in cycle 4; also, muscles IP, RA, and SA had bursts of shorter duration in cycle 4 as compared with those in the preceding cycles. These observations, together with those presented in Fig. 4.4B, indicate that the frog motor system is capable of immediately adjusting motor outputs for load compensation.

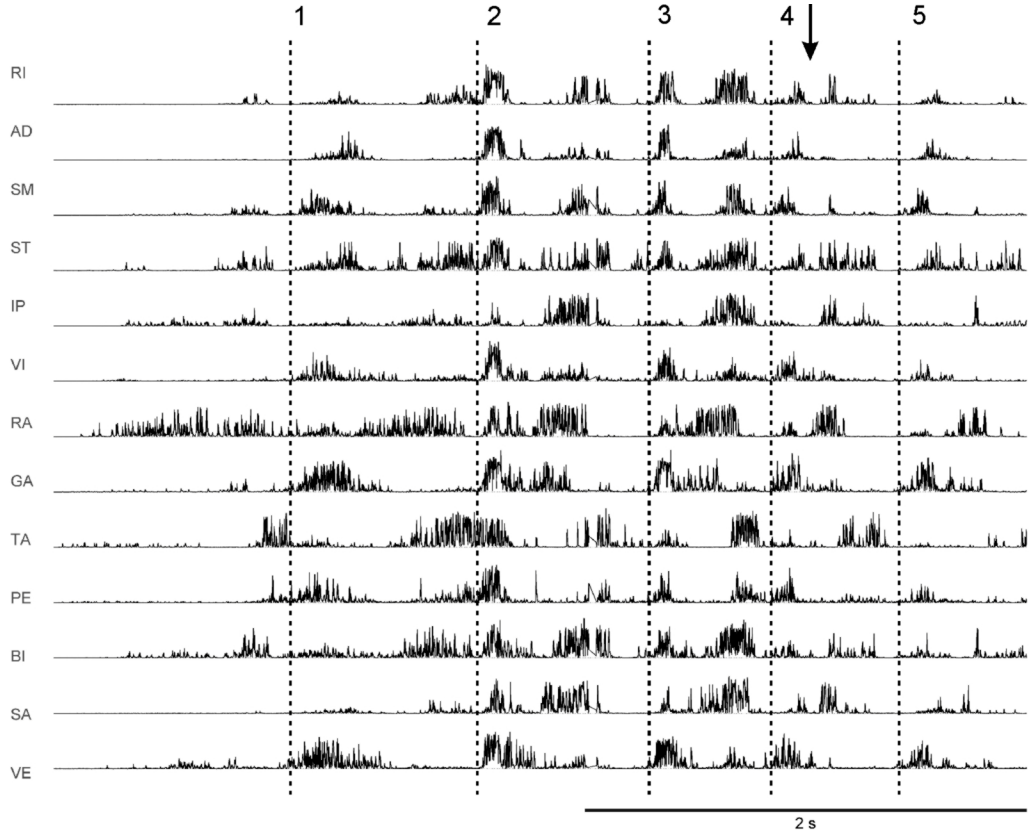


**FIGURE 4.5.** An example of swimming EMGs (rectified and high-pass filtered) collected after inertial loading. Shown here are 5 consecutive swimming cycles. Each cycle is demarcated by vertical dotted lines. The weight providing the additional inertial load was accidentally detached in cycle 4 (arrow). Notice that the duration of the IP, RA, and SA bursts shortened immediately after load detachment.

Up to this point, we have examined EMG changes associated with loading by comparing specific EMG examples collected before and after weight attachment. It is possible, however, that some of the changes described above are muscle patterns peculiar to the examples presented, and hence, are not representative across the entire sample of loaded EMGs. We sought to confirm that at least some of the EMG changes we have noted are representative by performing multiple comparison statistics on both the EMG burst duration and burst peak amplitude of all EMG episodes across all conditions, loaded and unloaded. The EMG bursts in all muscles were detected automatically by a burst detection procedure (see Methods, "Frog motor behaviors …"). For jumping and kicking, bursts activated in phase *a* and those in phase *b* (see Fig. 4.4) were compared separately. For kicking, we further examined whether loading differentially affects the EMGs of different kick types by dividing all kicks into three groups, and compared EMG bursts of each group separately. Kicks with knee displacement angles smaller than 20° are classified as caudal kicks; those with hip displacement angles smaller than 20°, lateral kicks; and the rest, caudal-lateral kicks (see Fig. 4.3B).

Figure 4.6 shows the mean EMG burst duration of three muscles – IP, RA, and SA – across the loaded and unloaded conditions. Data points whose differences are statistically significant (multiple comparison test; $p<0.05$) are connected by solid lines. We see that for both IP and SA, loading caused an increase in burst duration in stepping (Fig. 4.6B), swimming (Fig. 4.6B), lateral kicking and caudal-lateral kicking (Fig. 4.6A), but not in caudal kicking (Fig. 4.6A) and jumping (Fig. 4.6B). Muscle RA, however, showed a reversible increase in burst duration in all behaviors examined except caudal kicking. The statistical results shown here are consistent with some of our observations in the specific EMG examples described earlier, confirming that the increased burst duration seen in Figs. 4.4-4.5 are representative. Furthermore, the EMG changes shown in Fig. 4.6, except for the increase in IP duration in kicks, were repeatable across the 2 (jump, step, swim) or 3 (kick) loaded conditions, and reversible after load removal, suggesting strongly that they represent changes in motor outputs in response to the increased limb inertia rather than, for instance, consequences of muscle fatigue. More interesting is that some of the EMG changes associated with loading were manifested in multiple behaviors (e.g., duration of IP, RA, and SA increased after loading in stepping, swimming, lateral kicking, and caudal-lateral kicking), hinting at the possibility that there exist muscle synergies which not only remain invariant

across conditions, but are also used and modulated similarly in multiple behaviors in response to perturbation.

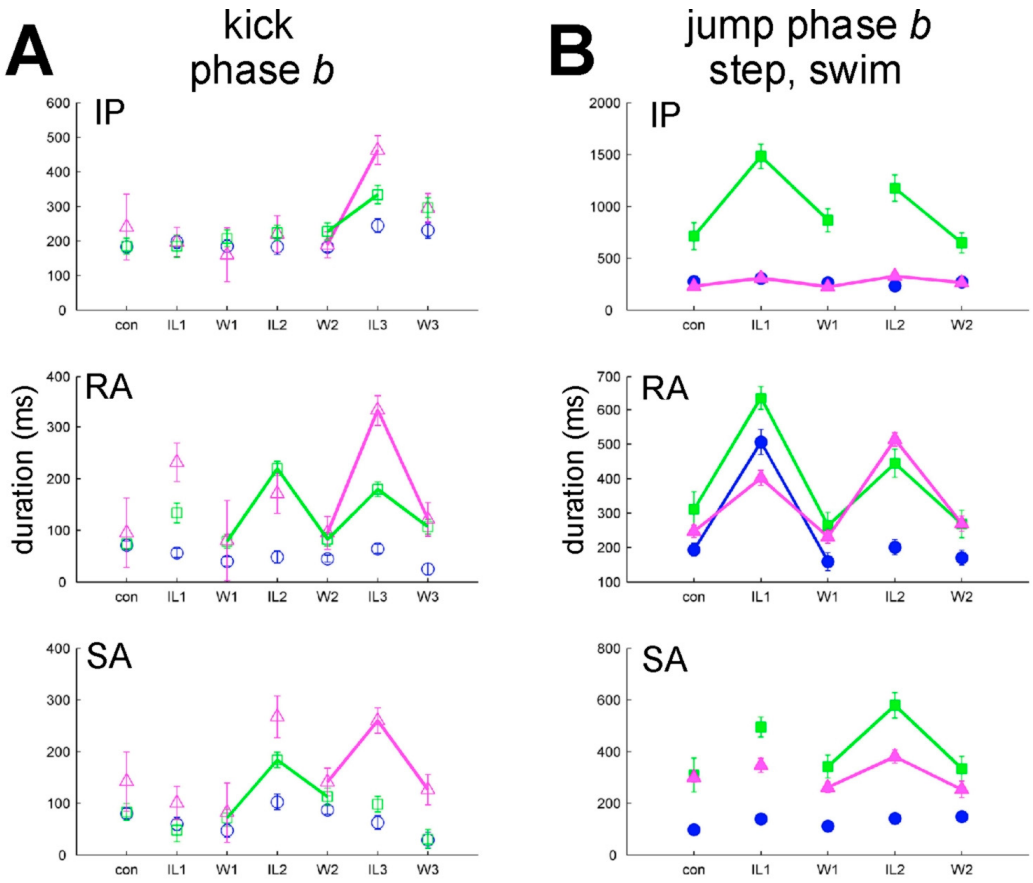


**FIGURE 4.6.** Statistics of EMG burst duration for muscles IP, RA, and SA, across control (con), wash1 (W1), wash2 (W2), wash3 (W3), and all loaded conditions (IL1, IL2, and IL3). *A*, Burst duration of each condition (mean ± SE) during phase *b* of kick (roughly corresponding to the flexion phase of the kick; see Fig. 4.5A). Caudal kicks, blue O; lateral kicks, green □; caudal-lateral kicks, magenta Δ. *B*, Burst duration of each condition (mean ± SE) during phase *b* of jump (blue, •), stepping cycles (green, ■), and swimming cycles (magenta, ▲). For each muscle and each behavior, burst duration values were compared across different conditions using multiple comparison statistics. Means showing statistically significant differences ($p < 0.05$) are connected by solid lines.

These observations of EMG changes motivated us to systematically test the hypothesis, that the altered muscle pattern observed after loading can be generated by modulating the activation pattern of a small set of invariant muscle synergies, identifiable by applying the non-negative matrix factorization (NMF) algorithm (Lee and Seung, 1999) to the EMG data. Following the analytical paradigm outlined previously in Cheung *et al.* (2005)

(this thesis, ch. 3), we divided our analyses into two stages. In stage I, we selected the number of synergies underlying each condition by extracting synergies from each condition separately; in stage II, we pooled all EMGs of each behavior together, and used a reformulated version of the NMF algorithm to identify synergies shared by all conditions, and also, synergies specific to one or multiple conditions. We then examined how the activation coefficients of the shared synergies were modulated across conditions, and compared results obtained from multiple behaviors.

**Analysis stage I: the loaded and unloaded data sets possess similar and low dimensionalities**

The NMF algorithm requires the number of synergies extracted from the EMG data set to be specified *a priori*. A major goal of analysis stage I, then, is to select the number of synergies underlying the EMGs of each condition. As explained in Methods ("Analysis stage I …"), realizing the difficulty of selecting this number based on plotting the $R^2$ against the number of synergies extracted, as pursued in previous studies (d'Avella *et al.*, 2003; Tresch *et al.*, 2006), we estimated the numbers of synergies by first calculating, for each extraction, the 95% confidence interval (C. I.) of the EMG reconstruction $R^2$, and then, selecting the numbers such that the $R^2$ of every condition is approximately 90% (as indicated by the $R^2$-C. I.'s of the different conditions overlapping each other). This way, we ensure that data of all conditions are described equally well at the chosen numbers of synergies.

The numbers of synergies selected by the above procedure for each behavior and condition are listed in Table 4.1 (left column). For most conditions, linearly combining 7 synergies are sufficient to describe the EMG data set comprising data from 13 muscles with an $R^2$ of ~90%. Also, for all behaviors examined, the numbers of synergies across conditions differ at most only by one. These results suggest that both the loaded and unloaded data sets possess similar and low dimensionalities.

When compared with the numbers of synergies published in previous studies of frog natural behaviors involving EMGs of the same 13 muscles, the numbers of synergies found here, ranging from 5 to 8 (Table 4.1, left column), are greater than the previously reported numbers by 1 to 2 [d'Avella and Bizzi (2005), 5 synergies with $R^2 \approx 90\%$; Cheung *et al.* (2005), 4-6 with ~90%; d'Avella (2000), 5-8 synergies but with $R^2 \approx 95\%$]. This is probably because in this study we normalized the EMG variance of each muscle before synergy

extraction, a step not performed in the above-cited studies. Variance normalization seems to us reasonable, because it ensures that the muscles composing the resulting synergies are not biased towards high-variance muscles. The numbers of synergies selected here, nevertheless, are still compatible with the ones found in the EMGs of spinalized frogs, elicited by NMDA iontophoresis (Saltiel *et al.*, 2001, in which 7 synergies are used to reconstruct EMGs of 12 muscles with $R^2 \approx 91\%$).

**TABLE 4.1. Analysis stage I for data from the inertial loading experiment.**

| beha-vior | number of synergies (stage I) | | | | | | | Stage-I $R^2$ of fits (%) | | | | | | |
|---|---|---|---|---|---|---|---|---|---|---|---|---|---|---|
| | con | IL1 | W1 | IL2 | W2 | IL3 | W3 | con | IL1 | W1 | IL2 | W2 | IL3 | W3 |
| frog 1: jump | 5 | 6 | 6 | 6 | 6 | - | - | 91.8 | 85.3 | 88.7 | 82.9 | 89.4 | - | - |
| frog 1: step | 7 | 8 | 7 | 7 | 7 | - | - | 90.1 | 83.7 | 85.9 | 81.7 | 87.4 | - | - |
| frog 1: kick | 7 | 7 | 7 | 6 | 7 | 7 | 7 | 90.9 | 84.9 | 87.2 | 81.4 | 81.9 | 77.9 | 82.5 |
| frog 2: swim | 7 | 7 | 8 | 7 | 7 | - | - | 92.2 | 89.8 | 89.9 | 90.9 | 89.4 | - | - |

As a first-pass assessment of the extent to which synergies are shared across the unloaded and loaded conditions, we next proceeded to fit the synergies extracted from the control data set, at its chosen number of synergies, to the EMG data of the other conditions. The $R^2$ values of this fit for the different conditions are listed in Table 4.1 (right column). In all behaviors, the control synergies can account for >80% of the variance in the EMG data of most of the other loaded (IL1, IL2, and IL3) and unloaded (wash1, wash2, and wash3) conditions, suggesting that many muscle synergies are probably shared between the unloaded and loaded data sets. However, in all behaviors except swimming, fitting the control synergies to the loaded data sets also yielded lower $R^2$ values as compared with fitting the same synergies to the unloaded data sets (e.g., $R^2 \approx$ 83-85% for fits to loaded jumps vs. ~89% to unloaded jumps). This indicates that there may be data structures peculiar to the loaded conditions; alternatively, the synergies extracted from the control data set may possess limited generalizing power owing to the limited data variability present in the control data set. Clearly, a more rigorous procedure is needed to evaluate the degree of synergy sharing across the different conditions.

**Analysis stage II: a novel algorithm for extracting shared and specific synergies, and an example illustrating how it works**

As adumbrated in the stage-I analysis above and explained in Methods ("Analysis stage II …"), it is difficult to assess the degree of synergy sharing across the unloaded and loaded conditions using only results obtained from our stage-I extractions, because any difference observed between the synergies extracted separately from different conditions could potentially be due to the limited data variability within each condition rather than changes in synergy composition across conditions. Thus, to account for this and other possibilities (see Methods, "Analysis stage II …"), we reformulated the NMF algorithm so that synergies shared by all conditions, as well as synergies specific to one or several conditions, can be extracted simultaneously from the pooled data set comprising data of all conditions.

The algorithm used here is essentially a generalization of a method we previously proposed: while the method described in Cheung *et al.* (2005; this thesis, ch. 3) was designed for comparing synergies of only two data sets, the algorithm used here extracts shared and specific synergies from an arbitrary number of data sets (or, in the context of this study, data from an arbitrary number of conditions). For each synergy extracted, the algorithm also returns a data set selection, representing the collection of conditions in which the extracted synergy is activated. Thus, for instance, if the data set selection for a synergy comprises all conditions, then the synergy is shared by all unloaded and loaded conditions; if, on the other hand, the selection comprises only IL1 and IL2, then the synergy extracted is specific only to the loaded conditions.

As described in detail in Methods ("Analysis stage II …"), at each iteration the algorithm finds one synergy and its corresponding data set selection by going through a list of all possible data set selections while keeping the number of synergies (or dimensionality) of each condition (determined in stage I) constant (Fig. 4.2). The data set selection that results in the extracted synergies describing all conditions equally well (as indicated by overlapping $R^2$-C. I.'s) is retained, and carried over to the next iteration. Since the numbers of synergies, determined in stage I (Table 4.1), are held fixed throughout, the *total* number of synergies, shared and specific, used to describe all conditions decreases with each iteration as more data set selections are found. This iterative algorithm thus amounts to finding the minimum *total* number of synergies, with their corresponding data set selections, that

describe the data of all conditions equally well, utilizing in the process the data variability offered by data of all conditions.

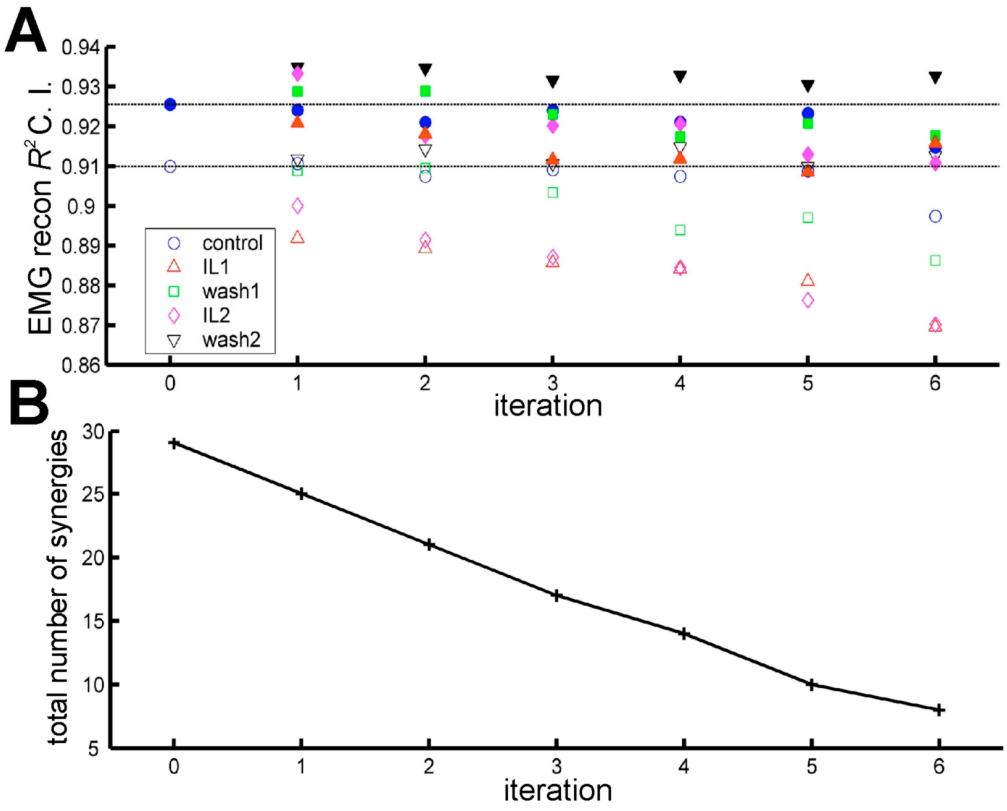


**FIGURE 4.7.** An illustration of how the stage-II algorithm works. Here, the stage-II algorithm described in Methods ("Analysis stage II …") is applied to the jumping data set of frog 1 comprising data from 5 conditions: control, IL1, wash1, IL2, and wash2. For this set of extractions, 6 iterations were performed, each finding the data set selection of one shared synergy. As shown in panel *A*, in each of these 6 iterations, the $R^2$ 95% confidence intervals (C. I.'s) for all conditions overlap with the control-C. I. of the previous iteration (blue O/●) as required by *step 3* of the algorithm. Panel *B* shows how the total number of synergies (shared and specific) used to describe the data set decreases as more shared synergies, and their corresponding data set selections, are found across iterations.

Figure 4.7 illustrates how this algorithm works by showing both the $R^2$-95% C. I. of each condition (Fig. 4.7A) and the total number of synergies used in reconstructing the EMGs of all conditions (Fig. 4.7B) after every iteration in the extraction run for the jumping data of frog 1. In Fig. 4.7A, the interval plotted at iteration 0 denotes the confidence interval obtained from the control data set in stage I, used in the algorithm as a reference C. I. for all subsequent iterations (see Methods, "Analysis stage II …"); in Fig. 4.7B, the number at iteration 0 represents the total number of stage-I synergies across all conditions selected for

the jumping data of frog 1 (5+6+6+6+6=29; see Table 4.1). Thus, while the $R^2$ of every condition was maintained at ~91% at all iterations (Fig. 4.7A), the total number of synergies used decreased from 29 to 8 as more and more data set selections were found across iterations (Fig. 4.7B). It is remarkable, that even though the algorithm only requires, at each iteration, the $R^2$-C. I.'s of all conditions to overlap with the control $R^2$-C. I. of the previous iteration (see *step 3* of the algorithm described in Methods, "Analysis stage II …"), the resulting $R^2$-C. I.'s of all iterations overlap with the original reference C. I. (Fig. 4.7A, dotted lines) very well. This further confirms that the overall quality of data description was not sacrificed as more shared synergies were extracted.

**Analysis stage II: most muscle synergies are shared by all loaded and unloaded conditions**

We applied the synergy extraction algorithm described above to the jumping, stepping, kicking, and swimming EMG data sets, each comprising data collected during all unloaded and loaded conditions. In the extraction run for each behavior, a set of time-invariant muscle synergies and their corresponding data set selections (denoting in which conditions each synergy is activated) were returned by the algorithm. In Fig. 4.8, each muscle synergy is depicted as a bar graph showing the balance of activation across all 13 recorded muscles; to the right of each synergy is a row of colored boxes: those corresponding to the conditions in which the synergy is activated are colored light green, and black otherwise. It is evident, that most of the synergies shown in Fig. 4.8 (23 out of 32) are activated across all conditions. This suggests that in all behaviors, many of the synergies are shared between the EMGs of the unloaded and loaded conditions, consistent with our observations of the raw EMG data (Fig. 4.4-4.5) described above (see Results, "Changes in muscle activation pattern …").

In Fig. 4.8, there are also pairs of similar synergies whose data set selections are complementary – that is to say, their selections together comprise all conditions, even though in none of the condition are both synergies activated. Jumping synergies J6 and J7 (Fig. 4.8A) and kicking synergies K7 and K8 (Fig. 4.8C) are two such complementary pairs. While the similarity between the synergies in each pair suggest that the two synergies might represent the same synergy, it is also possible, that they reflect how the composition of a synergy is slightly altered across conditions. In subsequent analysis of synergy activation

coefficients (see below), each of these pairs will be analyzed together as a single unit of activation.

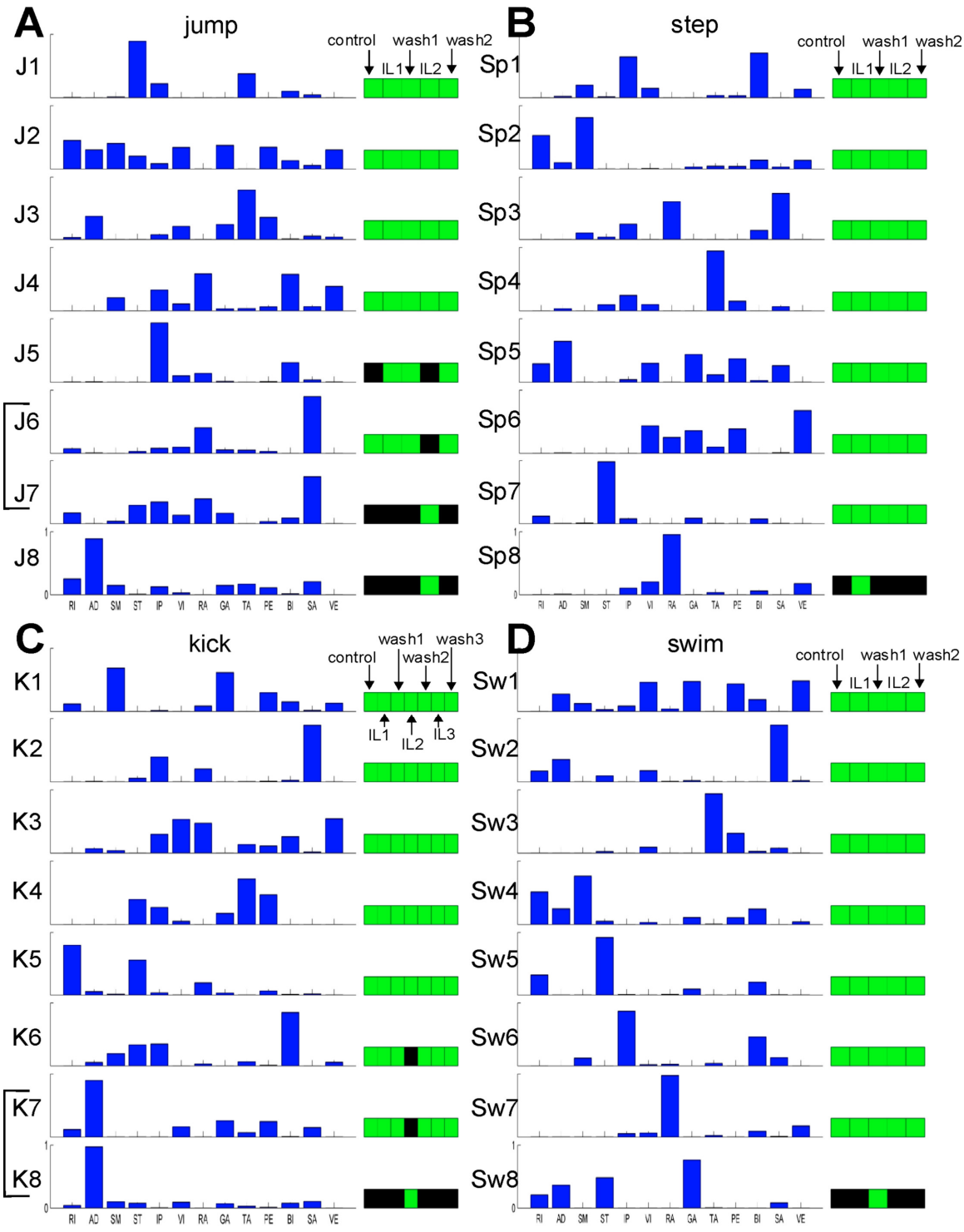


**FIGURE 4.8.** Muscle synergies and their corresponding data set selections extracted from the EMGs of the inertial loading experiments using our stage-II algorithm. The data set selection of each synergy is represented by a row of colored boxes analogous to those shown in Fig. 4.2. A green box

means that its corresponding data set is included in the selection, and a black box if otherwise. *A*, Jumping synergies (J1-J8). *B*, Stepping synergies (Sp1-Sp8). *C*, Kicking synergies (K1-K8). *D*, swimming synergies (Sw1-Sw8). The two pairs of synergies grouped by brackets (J6/J7, and K7/K8) show complementary data set selections.

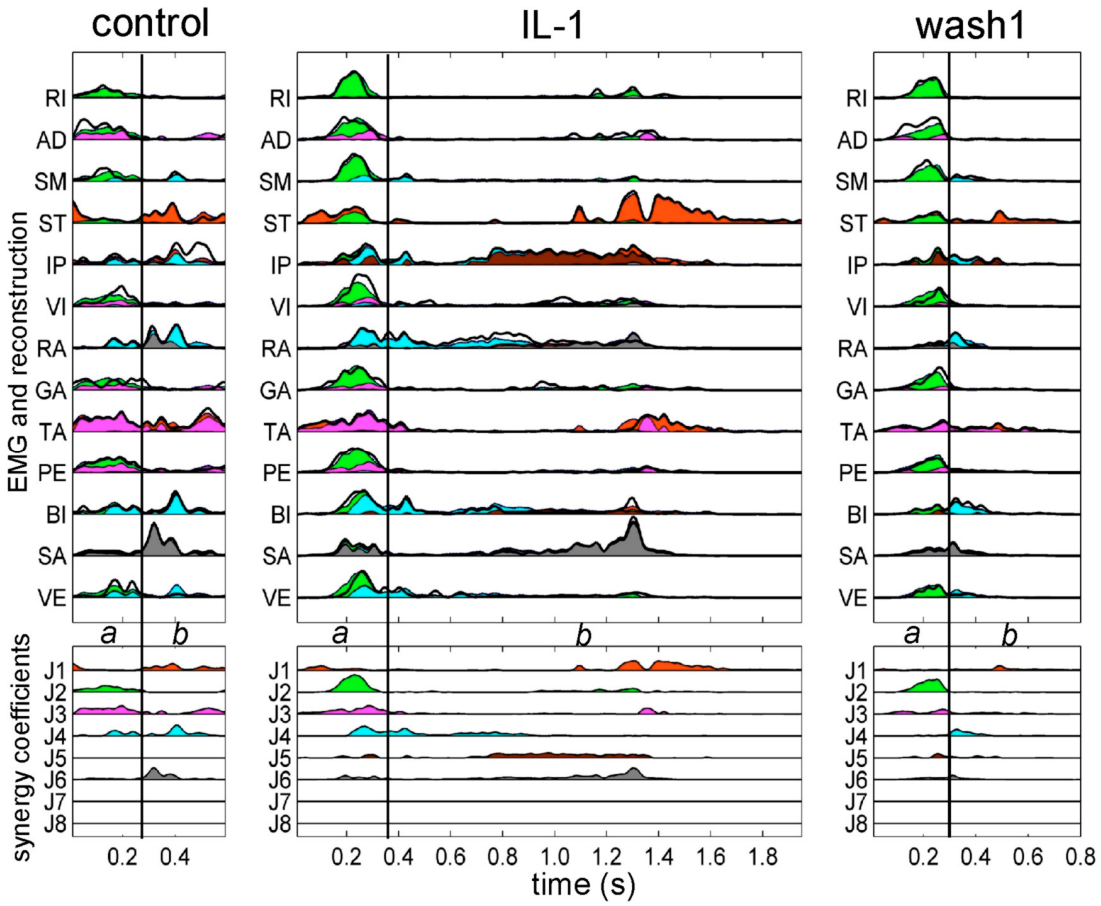


**FIGURE 4.9.** Reconstructing unloaded and loaded EMGs using the extracted synergies and their corresponding activation coefficients. The jumping episodes depicted in Fig. 4.4B are reconstructed in this figure using synergies J1-J8 (Fig. 4.8A). In the top panels, the actual EMG data (rectified, filtered, and integrated) are depicted in thick black lines. The reconstructed EMGs are shown in colors matching those shown in the coefficient time traces (bottom panels) in such a way that, at any time point, the colors reflect the respective contribution of each synergy to the reconstruction. As described in Results ("EMG changes observed …"), the prolonged RA burst in phase *b* observed after loading is described by prolonged activations of both synergy J4 (blue) and synergy J6 (gray). This figure demonstrates clearly that, the altered EMG pattern seen after inertial perturbation can be explained as altered activations of invariant synergies.

Excluding the complementary synergy pairs, there are two synergies in Fig. 4.8 activated only in loaded conditions – the jumping synergy J8 (active only in IL2), and the stepping synergy Sp8 (active only in IL1). These two synergies might represent modules activated specifically for load compensation (Kargo and Giszter, 2000a). However, since

neither of them is activated in both IL1 and IL2, the possibility that they arise due to incorrect dimensionality estimation in analysis stage I cannot be entirely excluded. The kicking synergy K6, on the other hand, is active in all conditions but IL2 (Fig. 4.8C); this finding is consistent with the observation that the amplitude of activation of this synergy decreased in caudal-lateral kicks in both IL1 and IL3 (see Table 4.2, cluster 7). Hence, activation of this synergy is inhibited by loading.

The data set selections of synergies J5 (Fig. 4.8A) and Sw8 (Fig. 4.8D) are more difficult to interpret. The former is activated in IL1, wash1, and wash2, and the latter, only in wash1. In fact, the amounts of EMG data variance explained by these synergies are relatively small (J5: 4.37%, 4.31%, and 6% in IL1, wash1, and wash2, respectively; Sw8: 3.56% in wash1). Thus, again, it is possible, that they arise due to inconsistent dimensionality estimation in analysis stage I.

**EMG changes observed after inertial loading explained as altered activations of shared synergies**

The finding of the previous section, that most synergies extracted are invariant across conditions, and the fact that linear combination of those synergies can describe the data of all conditions well (with $R^2 \approx 90\%$, as constrained by the algorithm; Fig. 4.7) anticipate that the EMG changes described previously (Figs. 4.4-4.6) can be attributed largely to changes in the activation pattern of invariant synergies. We demonstrate this by first reconstructing the EMGs using the extracted synergies and their corresponding activation coefficients. Figure 4.9 shows reconstruction of the jumping EMG episodes shown in Fig. 4.4B, along with the coefficient time traces of all jumping synergies (J1-J8) for these episodes. We see that the prolonged RA burst in phase *b* after loading is described by prolonged activations of both synergy J4 (blue) and synergy J6 (gray). The latter synergy also explains the increased SA burst duration in phase *b*. The prolonged phase-*b* IP burst in the IL1 episode, on the other hand, is described by a long coefficient burst of J5 (brown), a synergy activated in IL1 and wash1 but not in control. The RI and AD bursts recorded in phase *b* after loading are described by activations of J2 (green) and J3 (magenta), respectively, both of which have a data set selection comprising all conditions. Thus, except for the change seen in IP, all other EMG changes in phase *b* – observed in muscles RA, SA, RI, and

AD – can be attributed to altered activations of invariant synergies, confirming our earlier anticipation.

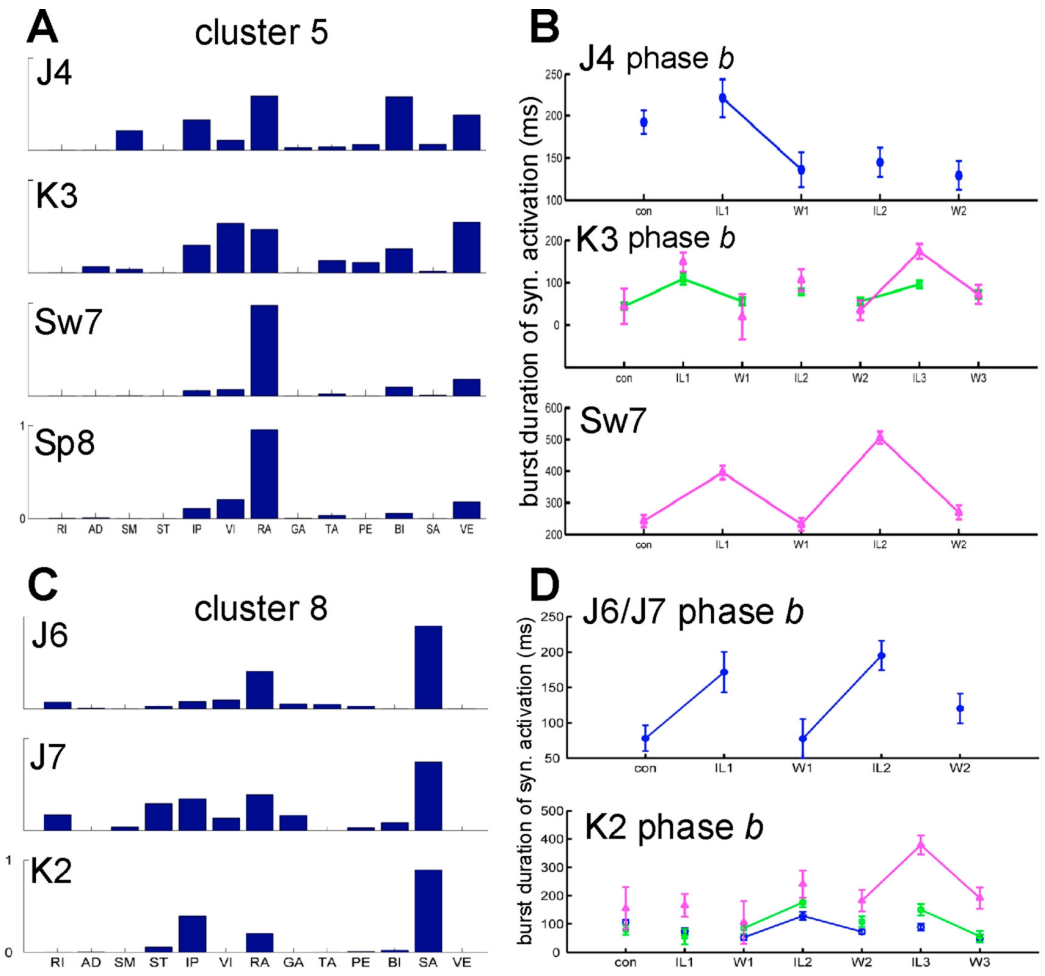


**FIGURE 4.10.** Clusters of muscle synergies used for different behaviors, and how the burst duration of their activation coefficients changed across conditions. Synergies extracted from the jumping, stepping, kicking, and swimming EMGs were categorized into groups using hierarchical cluster analysis (see Methods, "Clustering muscle synergies …"). For the inertial loading experiment, eight clusters were found (see Table 4.2). Two of the clusters are shown in this figure. *A*, Four of the synergies grouped under cluster 5, used for jumping (J4), kicking (K3), swimming (Sw7), and stepping (Sp8), respectively. The synergy labels here match those shown in Fig. 4.8. All of them comprise activation components in IP, VI, RA, BI, and SA. *B*, The burst duration of the time-varying activation coefficients for the synergies shown in *A* across different unloaded and loaded conditions (mean ± SE). The different means were compared using multiple comparison statistics, and those with statistically significant differences ($p < 0.05$) are connected by solid lines. For results of synergy K3, duration statistics was performed for lateral kicks (□, green) and caudal-lateral kicks (Δ, magenta) separately. Duration statistics for synergy Sp8 is not shown since it was found by the stage-II algorithm to be specific only to the IL1 condition. *C*, Three of the synergies in cluster 8, featuring activation components in muscles IP, RA, and SA. Synergies J6/J7, used for jumping, constitute a synergy pair with complementary data set selections (see also Fig. 4.8A). Synergy K2 is

used for kicking. *D*, The burst duration of the time-varying activation coefficients for the synergies shown in *C* (mean ± SE; multiple comparison, $p < 0.05$). For results of synergy K2, duration statistics of caudal kicks (O, blue), lateral kicks (□, green), and caudal-lateral kicks (Δ, magenta) are shown separately. Abbreviations: con, control; W1, wash1; W2, wash2; W3, wash3.

We proceeded to analyze how loading changed the amplitude and temporal patterns of synergy activation by performing multiple comparison statistics on the duration and peak amplitude of the coefficient bursts isolated from all episodes. The onset and offset times of the coefficient bursts were detected by the same burst detection procedure used for EMG analysis. In general, results of this population analysis agree well with the conclusions drawn from comparison of individual EMG episodes. For instance, as plotted in Fig. 4.10D, synergies J6/J7 showed reversible and repeatable increase in burst duration after weight attachment (IL1>con, and IL2>wash1, $p<0.05$), as demonstrated also in the individual examples of Fig. 4.9. The phase-*b* duration of J4, increased after loading in the examples of Fig. 4.9, also showed some load-related increase in duration at the population level (Fig. 4.10B; IL1>wash1, $p<0.05$), albeit less obviously than that of J6/J7 (Fig. 4.10D). These statistical results confirm that the activation patterns of synergies shared between unloaded and loaded conditions are altered by the added inertial load.

Table 4.2 summarizes how the duration and peak amplitude of the activation coefficient bursts of each muscle synergy were altered by an added inertial load (↑, increase; ↓, decrease). We see that the activation pattern of a synergy might be altered only during a specific phase of the movement (e.g., J2, of cluster 3, showed an increase in burst duration only in phase *b*), or only in a subset of a behavior (e.g., K5, of cluster 1, showed an increase in duration only in caudal-lateral kicks, but not in caudal or lateral kicks). For synergy K6 (cluster 7), the decrease in the duration and peak amplitude of its coefficient bursts over IL1 and IL3 is consistent with the finding that its data set selection does not include IL2 (Fig. 4.8C). Overall, the results listed in Table 4.2 support the conclusion that the additional inertial load of the limb modulates the activation pattern of invariant muscle synergies for adaptation during natural motor behaviors.

**TABLE 4.2. Characterizing changes in burst duration and amplitude of shared synergies associated with inertial loading.**

| cluster | major muscles | behavior | duration | peak amplitude | remarks |
|---|---|---|---|---|---|
| cluster 1 | RI, **ST**, (GA) | J1 | | | |
| | | Sp7 | | | |
| | | K5 | caud-lat phase *b*: ↑ | | |
| | | Sw5 | | | |
| | | Sw8 | | | active W1 only |
| cluster 2 | IP, (VI), **TA, PE**, (SA) | J3 | | phase *a*: ↓ | |
| | | Sp4 | | | |
| | | K4 | | caud phase *a*: ↓<br>lat phase *b*: ↑ | |
| | | Sw3 | | | |
| cluster 3 | **RI**, **SM**, VI, **GA**, PE, BI, VE | J2 | phase *b*: ↑ | | |
| | | Sp2 | | | |
| | | K1 | | | |
| | | Sw4 | ↑ | | |
| cluster 4 | RI, **AD**, VI, GA, (TA), PE, SA | J8 | | | active IL2 only |
| | | Sp5 | ↑ | | |
| | | K7 + K8 | lat phase *b*: ↑ | lat phase *b*: ↑ | |
| cluster 5 | (IP), **VI**, **RA**, (GA), (TA), BI, **VE** | J4 | phase *b*: ↑ | phase *b*: ↓ | |
| | | Sp6 | | | |
| | | Sp8 | | | active IL1 only |
| | | K3 | caud-lat phase *a*: ↑<br>caud-lat phase *b*: ↑<br>lat phase *b*: ↑ | caud-lat phase *a*: ↑<br>caud-lat phase *b*: ↑ | |
| | | Sw1 | | | |
| | | Sw7 | ↑ | | |
| cluster 6 | **IP**, **BI**, SA | J5 | | | active IL1, W1, W2 only |
| | | Sw6 | ↑ | | |
| cluster 7 | SM, **IP**, **BI**, VE | Sp1 | ↑ | | |
| | | K6 | caud-lat phase *b*: ↓ | caud-lat phase *b*: ↓ | not active IL2 |
| cluster 8 | (RI), IP, (VI), **RA**, **SA** | J6 + J7 | phase *a*: ↑<br>phase *b*: ↑ | | |
| | | Sp3 | | | |
| | | K2 | caud phase *b*: ↑<br>lat phase *b*: ↑<br>caud-lat phase *b*: ↑ | | |
| | | Sw2 | | | |

**Synergies, similar across behaviors, modulated similarly after loading**

We next proceeded to compare synergies, and their load-related changes in activation pattern, across different behaviors. All synergies extracted from the EMG data of all four behaviors studied (jumping, stepping, kicking, and swimming) were pooled together and clustered into groups. The number of clusters was determined objectively by finding the natural divisions in the synergy pool, quantified by the inconsistency coefficients of the links in the cluster tree (see Methods, "Clustering muscle synergies …").

The clustering algorithm we used grouped the 32 synergies of all behaviors (Fig. 4.8) into 8 clusters (Table 4.2). It is remarkable, that 5 of the 8 clusters comprise synergies of all four behaviors (clusters 1, 2, 3, 5, and 8 in Table 4.2). One cluster include synergies of 3 behaviors (cluster 4), and two clusters contain synergies of 2 behaviors (clusters 6 and 7). This result suggests that some of the muscle synergies are shared between behaviors, for the synergies within a cluster are, by definition, similar to each other.

As shown clearly in Table 4.2, some of the synergy clusters include synergies of different behaviors showing similar patterns of change in their activation coefficients after loading. For instance, the jumping synergy J3 and the kicking synergy K4, both of which include muscles TA and PE in their compositions, were classified into the same cluster, and both synergies were activated with decreased coefficient burst amplitudes in phase *a* after loading. Two other examples are illustrated in Fig. 4.10. As shown in Fig. 4.10A-B, 3 synergies from cluster 5 – J4 (jumping), K3 (kicking), and Sw7 (swimming) – all showed an increase in coefficient burst duration in one or both of the loaded conditions; another synergy in the same cluster, Sp8 (stepping), was even found to be active only in IL1 (Fig. 4.8B), consistent with the increase in burst duration seen in other synergies of the same cluster. Similarly, cluster 8, comprising synergies with components in muscles IP, RA, and SA, includes two synergies, used for jumping (J6/J7) and kicking (K2), respectively, whose coefficient bursts showed an increased duration in phase *b* after loading. These results, shown in Table 4.2 and Fig. 4.10, together suggest that there exist muscle synergies that are shared between different motor behaviors, and are modulated similarly when the limb is perturbed by an increased inertial load.

**Summary: main results of the inertial loading experiments**

In two frogs, we collected EMG data from four natural behaviors before and after the limb was perturbed by an additional inertial load. In analysis stage I, we applied the NMF algorithm to extract synergies for each behavior from data of each condition separately. Our procedure based on calculating the 95% confidence interval of the $R^2$ value found that, for all behaviors, the data of the different conditions possess similar and low dimensionalities (number of synergies ≈ 7, Table 4.1). Fitting the control synergies to the data of the other conditions also yielded high $R^2$ values (Table 4.1). In analysis stage II, we developed a reformulation of the NMF algorithm to extract synergies and their corresponding data set selections from the pooled unloaded and loaded data sets. Most synergies extracted were found to be activated in all conditions (Fig. 4.8), indicating that there is a high degree of synergy sharing between the unloaded and loaded conditions. Our statistical comparison of the coefficient burst duration and peak amplitude across conditions further suggest that loading altered the activation pattern of many synergies (Table 4.2, Figs. 4.9-4.10). Results from our clustering analysis also reveal that there are similar synergies used for different behaviors whose activations were modulated similarly by loading (Table 4.2, Fig. 4.10).

## Perturbing the limb with an elastic load

The second type of perturbation we have tried involves putting an elastic load on the limb provided by a rubber band, proximally attached to a fixed position on the frog's back, and distally, to either the knee (EL-h; Fig. 4.1B, left) or the ankle (EL-hk; Fig. 4.1B, right). The former attachment position (EL-h) directly affects motion of the hip joint, and the latter (EL-hk), motions of both the hip and knee joints. Both EL-h and EL-hk were applied to frog 3 during terrestrial behaviors (Fig. 4.1A), including jumps (unloaded, 149 episodes; EL-h, 43; EL-hk, 76), stepping episodes (98; 52; 117), and kicks (70; 25; 80). In frog 2, however, only EL-hk was applied during aquatic behaviors after the animal was previously exposed to an added inertial load (Fig. 4.1A). A total of 72 swimming episodes performed with elastic load perturbation were collected from frog 2.

Our analyses of these sets of EMG data involving elastic loading shall follow the strategies outlined in the previous section for analyzing data involving inertial loading. We

shall begin with inspection of the EMG data, followed by separate extractions of muscle synergies to determine the dimensionality of each condition (stage I), and then, simultaneous extractions of shared and specific synergies from the pooled EMG data sets (stage II). Finally, we analyze how the synergy activation coefficients were changed by loading, and compare synergies as well as any load-related changes of synergy activations across different behaviors.

**Jumping with an elastic load: an inserted phase with additional bursts of muscle activations**

Three examples of jumping EMGs and kinematics from frog 3 are depicted in Fig. 4.11A. As before, every jump was divided into two phases – *a* and *b* – for ease of inspection. In the example recorded under the control condition (Fig. 4.11A, left), jump extension was achieved in phase *a* through intense activations of many muscles, including RI, AD, SM, VI, GA, PE, and VE. The ensuing jump flexion in phase *b* was achieved first by activating 5 flexor muscles together, including SM, IP, RA, BI, and SA, and then, by activating another 2 muscles, ST, and TA. This jumping muscle pattern from frog 3 is similar to the jumping EMG record published previously (Cheung *et al.*, 2005, their Fig. 2), and to the pattern from frog 1 described earlier (Fig. 4.4B).

Elastic loading to the hip joint (EL-h) produced noticeable changes in both the EMGs and kinematics of jumping. Shown in the middle panel of Fig. 4.11A is the EMG record of the second jump observed after installation of the EL-h load. In phase *a*, jump extension after loading was achieved through activations of the same set of muscles seen in phase *a* of the control example. However, immediately after this initial phase, we see a new, additional phase over which there was limited motion in both the hip and knee joints, and in which long bursts of activation were observed in many muscles, including RI, AD, ST, VI, GA, PE, BI, SA, and VE. During the jump flexion that follows, we see again activations of the SM-IP-RA-BI-SA group (indicated by the 2$^{nd}$ vertical line in the panel) followed by the ST-TA group, the same pattern observed in phase *b* of the control episode. Thus, in jumping, elastic loading seems to result in a new phase of muscle activations inserted between the usual extension and flexion EMG phases. This inserted pattern could well represent a load-specific muscle synergy not normally utilized in the construction of the jumping behavior.

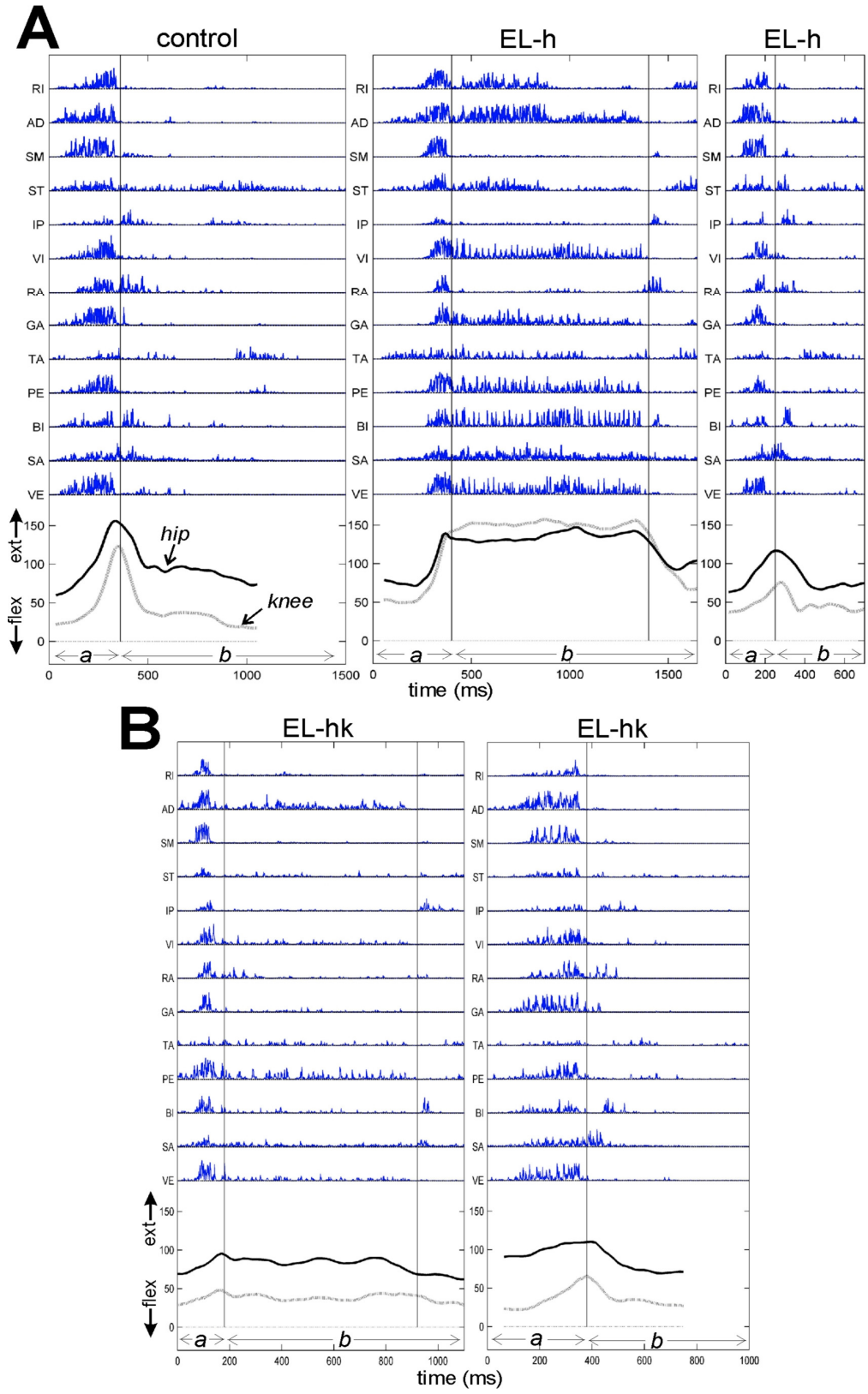


**FIGURE 4.11.** Examples of jumping EMG and kinematics data collected before (control) and after (EL-h; EL-hk) elastic loading. Each jumping episode here is divided into 2 phases, *a*, and *b*, roughly

corresponding to jump extension and flexion, respectively, for ease of visual inspection. The EMGs displayed here are rectified and high-pass filtered (FIR, 50th order, cutoff of 50 Hz). See Results, "Jumping with an elastic load, …", for detailed descriptions of these EMG episodes. Also, see Fig. 4.1C for definitions of hip and joint angles.

Not every jump observed under EL-h exhibited the EMG pattern exemplified in the middle panel of Fig. 4.11A, however. Among the 43 jumps from frog 3 observed under the EL-h condition, 18 jumps showed EMG patterns without the new inserted phase, similar to the pattern of the control jumps. One such example is shown in the right panel of Fig. 4.11A, in which the inserted phase seen in the middle panel is clearly absent. But at the same time, the extent of limb extension in this loaded jump (Fig. 4.11A, right) is also smaller than that recorded in the other two jumping examples in the figure. It is possible, that the inserted phase shown in the middle panel can only be elicited by a sufficiently large retraction force resulting from the rubber band having been sufficiently stretched by a much extended hip. A rigorous demonstration of this hypothesis, however, requires a more detailed study of the relationship between the EMGs and kinematics which is beyond the scope of the present analysis.

Elastic loading to both the hip and knee joints (EL-hk) resulted in EMG changes similar to those observed under EL-h. For instance, in the left panel of Fig. 4.11B, showing the first jump observed under EL-hk, there is also an inserted phase, analogous to that shown in the middle panel of Fig. 4.11A, in which we find activations of AD, VI, PE, and VE. As in EL-h, in EL-hk some of the jumps (48 out of 76 jumps) exhibited EMG patterns without the inserted phase (Fig. 4.11B, right), similar to the unloaded EMG pattern. Overall, the similarity in muscle groupings between the control, EL-h, and EL-hk jumps suggests that there are synergies shared between the unloaded and loaded conditions, but the synergies underlying the EMGs of the inserted phase could be shared synergies, and/or new synergies specific to the loaded conditions.

To confirm that the inserted EMG phases described above are not peculiar just to the individual jumping examples shown in Fig. 4.11, we calculated the total EMG activity of each muscle in phase *b* of each jump (after rectification, filtering, and integration of the raw EMG data, as described in Methods, "EMG data preprocessing …"). Figure 4.12 plots the total EMG activity of two muscles, AD and PE, during phase *b* of jumping across all the unloaded and loaded conditions. Clearly, in both muscles, the distributions of total activities

for both loaded conditions (EL-h and EL-hk) lie above those for the unloaded conditions (control, wash1 and wash2) ($p<0.05$), consistent with the earlier observation that many loaded jumping episodes contain an inserted phase in phase *b* with additional activations of AD and PE (Fig. 4.11). At the same time, the loaded distributions also overlap substantially with the unloaded distributions, again consistent with the observation that many loaded jumps have EMG patterns similar to the normal, unloaded muscle pattern.

Other muscles showing a statistically significant increase ($p<0.05$) in phase-*b* total EMG activity during jumping in EL-h include RI, VI, GA, BI, SA, and VE.

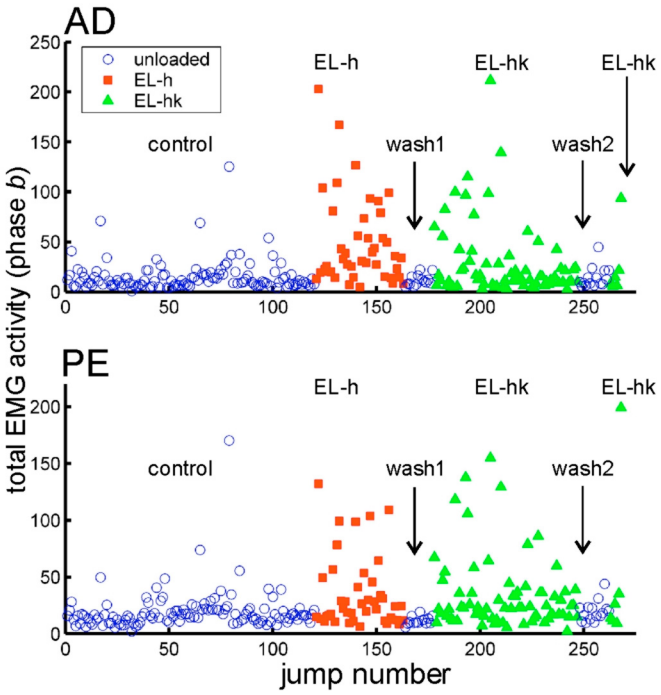


**FIGURE 4.12.** Total EMG activities of muscles AD and PE during phase *b* of jumping across the different unloaded and loaded conditions. Here, total EMG activity refers to the sum of all EMG data points in phase *b* after rectification, filtering, and integration of the EMG data. Notice that for both muscles, the distributions of total activities for both loaded conditions (EL-h, red ■; and EL-hk, green ▲) lie above those for the unloaded conditions (blue O), consistent with the observation in Fig. 4.11 that many loaded jumping episodes contain an inserted EMG phase within phase *b*.

**Stepping with an elastic load: altered amplitude relationship between the flexors and extensors**

We next proceeded to examine how elastic loading influenced the EMG pattern of stepping cycles. Since limb extension was resisted by the rubber band's elasticity, and limb flexion, assisted by its recoil, we expected the muscle patterns of both the extension and flexion phases of the cycle to be affected by loading.

Shown in Fig. 4.13 are four episodes of stepping, each containing multiple consecutive walking cycles. Cycle boundaries within each episode are demarcated by vertical straight lines. In the control episode (Fig. 4.13A), step extension was executed by activations of RI, AD, SM (hip extensors), VI, PE, VE (knee extensors), GA (ankle extensor), and BI (hip-knee flexor); step flexion was initiated by bursts in IP, RA (hip flexors), BI, and SA (hip-knee flexors), and then, followed by bursts in ST (knee flexor), TA, and PE (ankle flexors). Remarkably, these muscle groupings underlying step extension and flexion remained unchanged after the hip-joint elastic load (EL-h) was installed. As exemplified by Fig. 4.13B, extension and flexion were carried out by the same sets of muscles, but after loading the amplitude of RA during flexion was much attenuated. These observations indicate that elastic loading probably does not change the compositions of the stepping synergies, but the recoiling force exerted by the rubber band may decrease the activation amplitude of the synergies underlying limb flexion.

Such reductions of flexor activations during flexion were more obvious when the elastic load directly affected both the hip and knee joints (EL-hk). In Fig. 4.13C, we notice that while step extension is accompanied by bursts in AD, VI, TA, PE, BI, and VE, throughout the episode there is hardly any activation in IP, RA, and SA, the flexors activated during step flexion of the control episode. The amplitude of ST, a knee flexor, is also much reduced in Fig. 4.13C as compared with those in Fig. 4.13A-B. Moreover, under EL-hk the ranges of motion in both joints were much reduced as well. In particular, there was very little cyclic knee motion as it was constantly flexed by the rubber band throughout the episode.

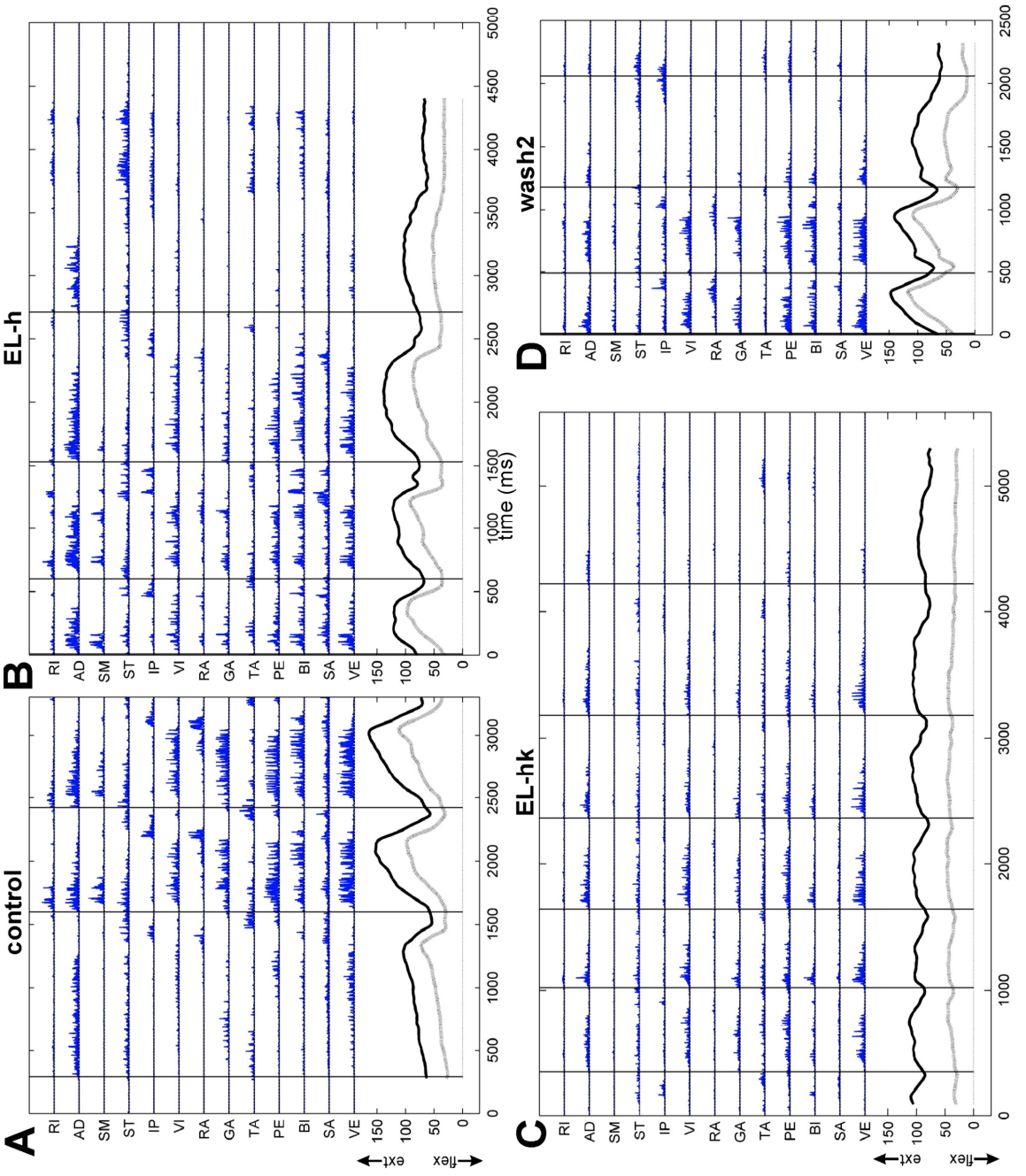


**FIGURE 4.13.** Examples of stepping EMG and kinematics data collected before (control, *A*) and after (EL-h, *B*; EL-hk, *C*) elastic loading, as well as after load removal (wash2, *D*). Each stepping episode here contains multiple consecutive stepping cycles, each of which is demarcated in the figure

by vertical lines. See Results, "Stepping with an elastic load, …", for detailed descriptions of these EMG episodes. Also, see Fig. 4.1C for definitions of hip and joint angles.

The changes highlighted in Fig. 4.13B-C were reversible after load removal, as the washout EMG pattern (Fig. 4.13D) is similar to the control EMG pattern (Fig. 4.13A). This confirms that the decrease in flexor burst amplitude is unlikely to be a result of degraded recording quality or deceased muscle fibers.

In order to further examine whether loading affects the relationship between the extensor and flexor amplitudes, and to better understand the source of variability of the flexor amplitude during stepping, we proceeded to divide each step cycle into two phases, corresponding to step extension and flexion, respectively. Burst amplitudes in each phase can then be related to those of the other phase. The boundary between the two phases is defined to be the offset time of the AD burst in each cycle. Fig. 4.14A plots, for the control episodes, the relationship between the cycle peak amplitude of RA (hip flexor) during the flexion phase, and that of AD (hip extensor) during the extension phase. We see that the amplitudes of these two muscles are directly proportional to each other. This observation suggests that in the unloaded condition, the variability of the amplitude of RA (a flexor) during the flexion phase can be attributed in part to the variability of the amplitude of AD (an extensor) in the preceding extension phase.

We next sought to examine whether elastic loading affected the relationship depicted in Fig. 4.14A by computing, for every loaded and unloaded step cycle, the ratio between the amplitude of a flexor during flexion, and that of an extensor during extension. We then averaged this flexor-to-extensor amplitude ratio across all cycles within every stepping episode, and plotted it against time. As shown in Fig. 4.14B, the RA(flex)-to-AD(ext) ratio decreased substantially during both EL-h (■) and EL-hk (♦), consistent with our earlier observation that the flexor amplitude decreased after loading (Fig. 4.13B-C). Interestingly, when the frog stepped up an incline with the elastic load on (▲) so that it needed to work against both an increased gravitational load and the added elastic load, this RA-to-AD ratio increased back up to the control level. Also, such changes in the amplitude ratio were reversible after load removal, as attested by the return of this ratio back to the control level during both washout periods (O). Together, these observations suggest that the relationship between the amplitudes of both the extensors and flexors during stepping is constantly

subject to modulation by sensory stimuli to accommodate changes in the external dynamic environment.

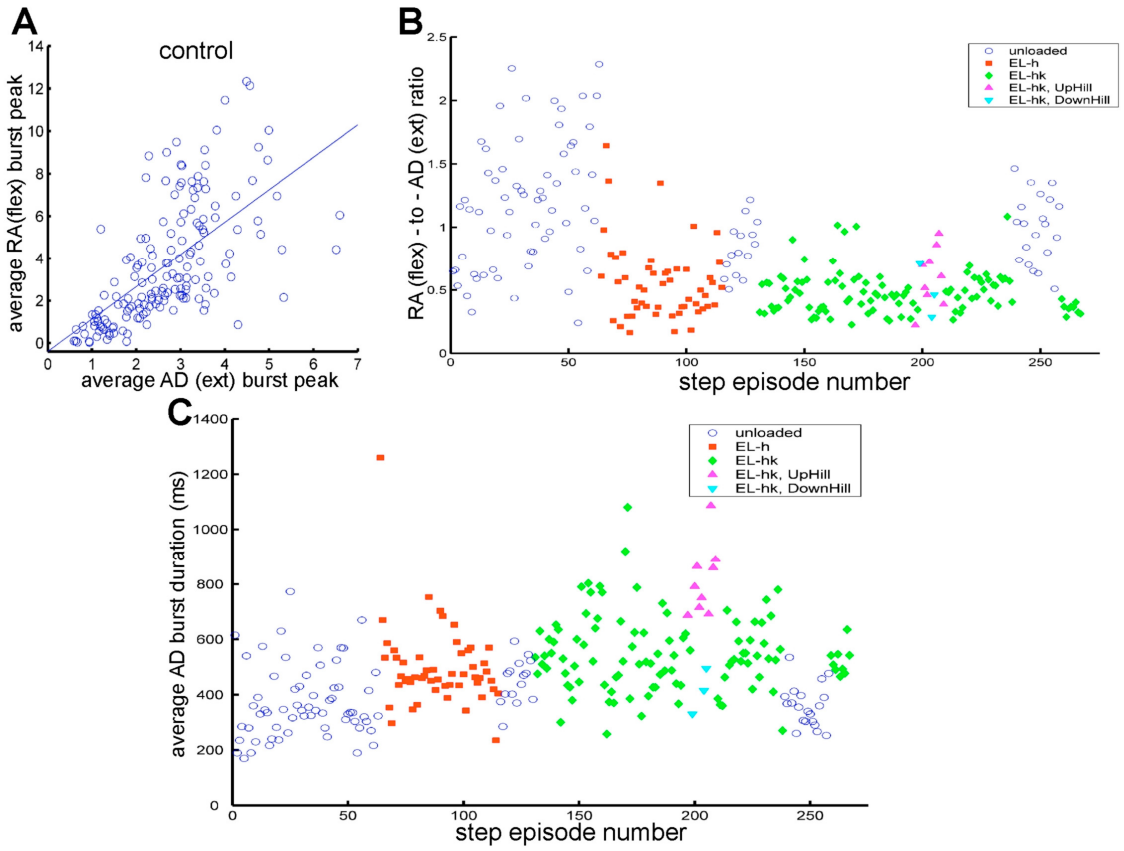


**FIGURE 4.14.** Relationship between the extensor and flexor EMG amplitudes in stepping before and after elastic loading. To obtain the relationship between the EMG amplitude of the extensor during step extension, and that of the flexor during step flexion, each step cycle was divided into the extension and flexion phases. The boundary of the two phases within each cycle was defined to be the offset time of the AD EMG burst. For each stepping episode, the average extensor or flexor peak amplitude was then calculated across all cycles within that episode. *A*, Even before loading, the amplitude of AD (hip extensor) during extension was observed to be directly proportional to that of RA (hip flexor) during flexion. *B*, The observation in panel *A* prompted us to characterize the amplitude variability of the extensors and flexors by calculating, for each stepping episode, the ratio between the flexor amplitude during flexion and the extensor amplitude during extension, averaged across all cycles within an episode. In this panel, we see that, elastic loading (EL-h, red ■; EL-hk, green ♦) caused a decrease in this ratio as compared with the unloaded conditions (blue O). *C*, The burst duration of muscle AD across different unloaded and loaded conditions. The distributions of burst duration for both EL-h (red ■) and EL-hk (green ♦) tend to lie above those for the unloaded conditions (blue O). Also, uphill stepping along with the added elastic load (magenta ▲), but not downhill stepping (blue ▼), increased AD duration further above the EL-hk level. These suggest that the duration of the extensor is continuously being adjusted by sensory afferents to accommodate different external dynamic requirements.

Elastic loading also increased the duration of the AD bursts during step extension. As shown in Fig. 4.14C, the distributions of burst duration for both EL-h (■) and EL-hk (♦) tend to lie above those for the unloaded conditions (O). Also, uphill stepping along with the added elastic load (▲) increased AD duration further above the EL-hk level. Multiple comparison statistical tests ($\alpha$=0.05) confirmed that such increases in duration are statistically significant (EL-h>control and wash2; EL-hk-session 4>control, wash1 and wash2; EL-hk-session 5>control and wash2; EL-hk-uphill>all other groups). These results hint at the possibility that elastic loading may also change the burst duration of the synergy activation coefficients, as observed after inertial loading.

To summarize before the next section: inspection of the stepping EMG data collected before and after elastic loading suggests that the synergies underlying unloaded stepping are likely to remain unchanged after loading (Fig. 4.13). But the amplitude relationship between the extension and flexion synergies is expected to be modulated by the elastic load (Fig. 4.13B-C, Fig. 4.14A-B). Finally, loading may also change the activation duration of certain synergies (Fig. 4.14C). In the next section, we follow the two-stage analytic paradigm outlined above in our analyses of data involving inertial loading to extract muscle synergies systematically, and to test rigorously whether these intuitive conclusions based on visual inspection of EMG data are valid.

**Analysis stage I: robustness of the low-dimensionality conclusion across the elastic loading conditions**

As described before, in stage I we extracted muscle synergies from each condition separately, and then, selected the number of synergies underlying each condition so that the $R^2$ describing the quality of EMG reconstruction using the selected number of synergies is approximately 90% for every condition. Listed in Table 4.3 (left column) are the numbers of synergies for each behavior estimated using our procedure. The estimated number ranges from 4 to 8 with most of them being equal to 5, 6, or 7. Also, for jump, step, and kick, the numbers of synergies across conditions differ only by 1, and for swim, by 2. Thus, the earlier conclusion that EMG data of the different natural behaviors possess low dimensionalities is also robust across both types of elastic loading conditions (EL-h and EL-hk).

**TABLE 4.3. Analysis stage I for data from the elastic loading experiment.**

| beh-avior | number of synergies (stage I) | | | | | | | | Stage-I $R^2$ of fits (%) | | | | | | |
|---|---|---|---|---|---|---|---|---|---|---|---|---|---|---|---|
| | con | EL-h | EL-hk (s4) | EL-hk (s5-6) | W1 + W2 | W4 | EL-hk | W5 | con | EL-h | W1 | EL-hk (s4) | EL-hk (s5-6) | W2 | EL-hk (s6) |
| frog3 jump | 4 | 5 | 4 | 5 | 4 | - | - | - | 90.3 | 80.9 | 87.9 | 83.2 | 85.7 | 83.0 | 68.4 |
| frog3 step | 7 | 7 | 6 | 6 | 7 | - | - | - | 91.5 | 85.7 | 90.6 | 87.1 | 83.7 | 89.2 | 84.3 |
| frog3 kick | 6 | 5 | 5 | 5 | 5 | - | - | - | 91.2 | 88.5 | 88.3 | 87.3 | 85.3 | 85.3 | 84.2 |
| frog2 swim | 7 | - | - | - | - | 7 | 8 | 6 | 92.2 | - | 89.0 | 89.3 | - | 87.9 | - |

It is noteworthy, that for jump (frog 3), the numbers of synergies selected for EL-h and EL-hk (sessions 5-6) are greater than those selected for control and wash by 1; similarly, for swim (frog 2), the number of synergies underlying EL-hk is also greater than those underlying control and wash4 by 1. These results are consistent with the earlier illustration that there may be an additional, load-specific muscle synergy activated under the EL-h and EL-hk conditions (Fig. 4.11; Fig. 4.12). On the other hand, for step (frog 3), our analysis shows that the EL-hk condition may possess 1 less synergy than the unloaded conditions, indicating that the much attenuated flexor amplitudes during step flexion after loading (Fig. 4.13C; Fig. 4.14B) may correspond to a load-specific deletion of a synergy normally activated during step flexion.

As before, we performed a first-pass assessment of the degree of synergy sharing across conditions by fitting the control synergies (at the number of synergies selected in stage I for the control condition) to the EMG data of the other conditions. All $R^2$ values describing the quality of these fits, save one, are above 80% (Table 4.3, right column), suggesting that many muscle synergies are shared across conditions. The exceptionally low $R^2$ for EL-hk-session 6 in jump (frog 3) might be related to the fact that only a small amount of jumping data was collected under this condition.

**Analysis stage II: shared, additional, and deleted muscle synergies**

After stage I, we proceeded to extract shared and specific synergies for each behavior using our stage-II reformulated NMF algorithm to rigorously assess the extent of synergy sharing across the unloaded and loaded conditions, and to isolate synergies that were expressed only in one or several of the conditions. To reiterate, in stage II, the algorithm searches for synergies from the pooled data set comprising EMG data of all conditions while the number of synergies of each condition is fixed at the number determined in stage I. It returns, for each synergy found, a data set selection specifying the subset of conditions in which the corresponding synergy is activated.

The stage-II muscle synergies extracted from the pooled unloaded and loaded data sets are shown in Fig. 4.15. In each of the four behaviors, there are several synergies whose data set selections span all conditions: 3 synergies for jump (J1-J3), 3 for step (Sp1-Sp3), 4 for kick (K1-K4), and 3 for swim (Sw1-Sw3). This confirms our earlier intuition from visual examination of the EMG data that there are invariant synergies activated in both the unloaded and loaded conditions. At the same time, there are also groups of synergies having similar structures, and also, complementary data set selections that together comprise all conditions. In Fig. 4.15, these complementary synergies are grouped together by brackets. For instance, for jump (Fig. 4.15A), synergies J4 and J5 are complementary; for step (Fig. 4.15B), there are 3 complementary synergy groups: Sp4 + Sp5, Sp6 + Sp7, and Sp8 + Sp9 + Sp10. Since synergies within each complementary group have very similar structures, they may together represent a single, invariant synergy activated across all conditions. Counting both the complementary synergy groups, as well as the synergies with data set selections spanning all conditions, as representations of invariant synergies, we see, in Fig. 4.15, that for all behaviors, most of the synergies extracted are indeed shared across all unloaded and loaded conditions. For jump, 5 of 7 synergies are shared across all conditions; for step, 10 of 13; for kick, 6 of 7; and for swim, 11 of 12. These results support that the muscle synergies extracted are robust across the elastic loading conditions.

It is noteworthy that some of the synergies in Fig. 4.15 are specific to the loaded conditions, thus representing modules activated only when the limb was perturbed by the elastic load. For example, for jump (Fig. 4.15A), synergy J6 was found to be specific to EL-h. It accounts for 19.9% of the jumping EMG data variance in EL-h, and such a high percentage indicates that this load-specific synergy is highly significant. Similarly, synergy J7,

accounting for 15.4% of jumping EMG data variance, was found by the algorithm to be specific to EL-hk (sessions 5-6). These extraction results are consistent with our earlier speculation, based on visual examination of the jumping EMGs (Fig. 4.11), that a new synergy not normally utilized in the unloaded condition underlies the inserted EMG phase seen after elastic loading. Another load-specific synergy is seen in the set of swimming synergies (Fig. 4.15D): Sw12, specific to EL-hk. Remarkably, the major muscles composing this synergy – AD, VI, and PE – are also active in the jumping load-specific synergies, J6 and J7. Thus, for the jumping and swimming EMGs, some of the EMG changes associated with elastic loading might be attributed to additional muscle synergies whose expressions are elicited specifically by the elastic perturbation.

Also interesting are three of the stepping synergies – Sp11, Sp12, and Sp13, all involving activations of RI and ST, two muscles with knee flexor and hip extensor functions. While the similarity of these three synergies suggests that they might represent a single synergy, their data set selections together comprise only three of the five conditions – control, EL-h, and wash. Normally activated during step flexion (see Fig. 4.13A), this RI-ST synergy was hence not expressed in the EL-hk conditions, consistent with our observation in Fig. 4.13C that ST activity was much attenuated when the elastic load affected both the hip and knee joints. Thus, for the stepping EMGs, some of the EMG changes associated with elastic loading might be due to deletion of a flexor synergy.

In Fig. 4.15 there are two synergies whose data set selections are more difficult to interpret. The kicking synergy K7 was found to be active only in control. This synergy is likely to be not significant, however, as it only explains 5.6% of the control data variance. The swimming synergy Sw4 was determined to be active in control, wash2, and EL-hk, but not in wash3, explaining 7.5%, 7.5% and 10.6% of the data variances of the above-listed conditions, respectively. We speculate that its absence in wash3 might be attributed to behavioral variability across conditions, or incorrect dimensionality estimation in our stage-I analysis.

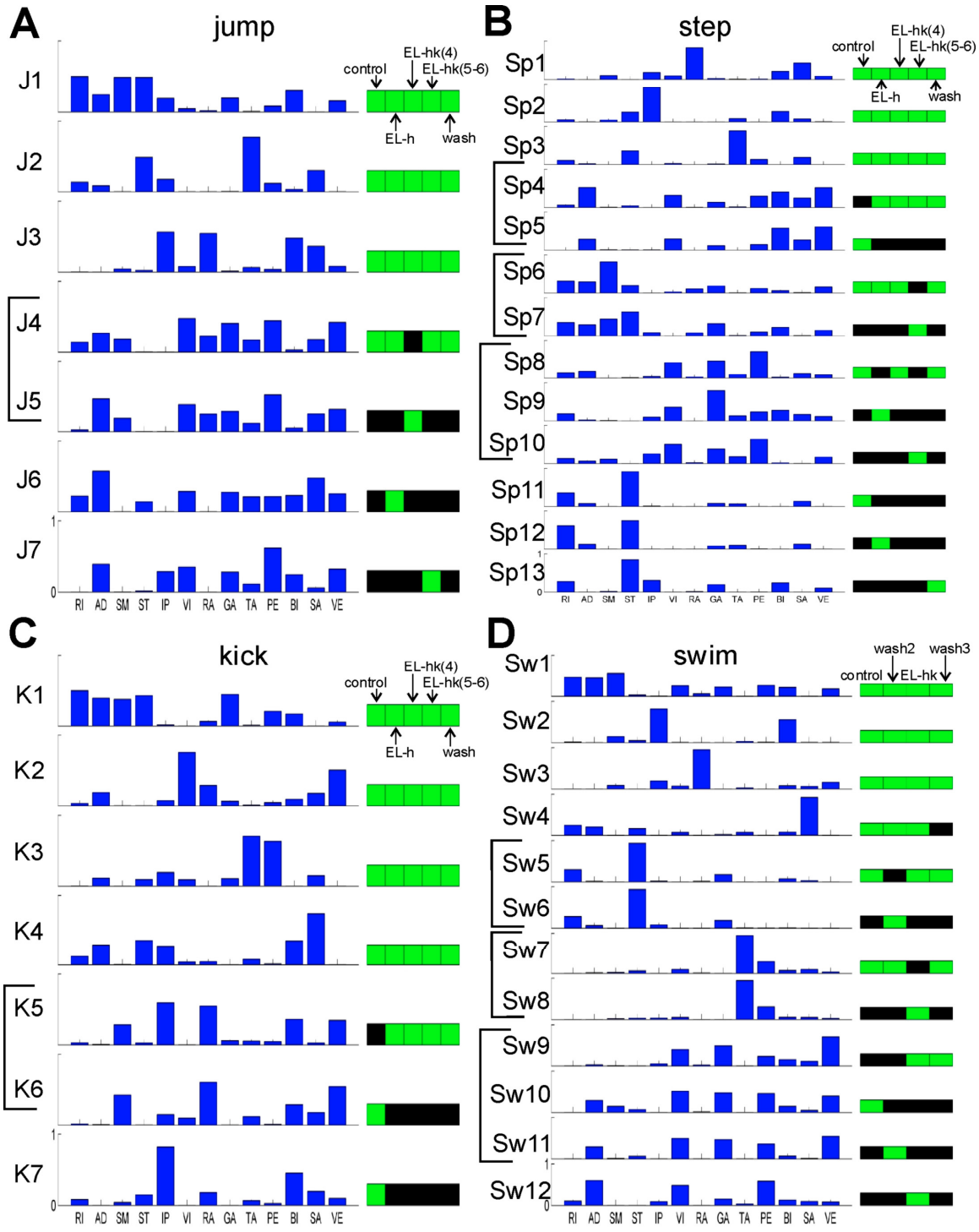


**FIGURE 4.15.** Muscle synergies and their corresponding data set selections extracted from the EMGs of the elastic loading experiments using our stage-II algorithm. The data set selection of each synergy is represented by a row of colored boxes analogous to those shown in Figs. 4.2 & 4.8. A green box means that its corresponding data set is included in the selection, and a black box if otherwise. *A*, Jumping synergies (J1-J7). *B*, Stepping synergies (Sp1-Sp13). *C*, Kicking synergies (K1-K7). *D*, swimming synergies (Sw1-Sw12). Groups of synergies marked by brackets (e.g., J4/J5; or Sw9/Sw10/Sw11) show complementary data set selections.

**Describing EMG changes observed after loading using the extracted synergies and their coefficients**

We next proceeded to examine how the EMGs collected before and after elastic loading can be reconstructed using the extracted synergies and their coefficients so as to visualize how the load-related EMG alterations are described by the synergy coefficients. Reconstructions of two of the jumping episodes described earlier (Fig. 4.11A, left and middle), collected from control and EL-h, respectively, are shown in Fig. 4.16. We see clearly that the muscle pattern within the inserted phase of phase *b* in Fig. 4.16B – the most noticeable difference between the control and the loaded examples – is mostly contributed by activation of synergy J6 (gray), and less importantly, by activations of synergies J1-J4. As shown earlier, synergy J6 was extracted by our stage-II algorithm as a synergy specific only to the EL-h condition (Fig. 4.15B). These observations thus confirm that in jumping, a synergy activated after loading, and not utilized in the construction of the unloaded muscle pattern, plays a prominent role in describing the EMG changes observed after perturbation delivery.

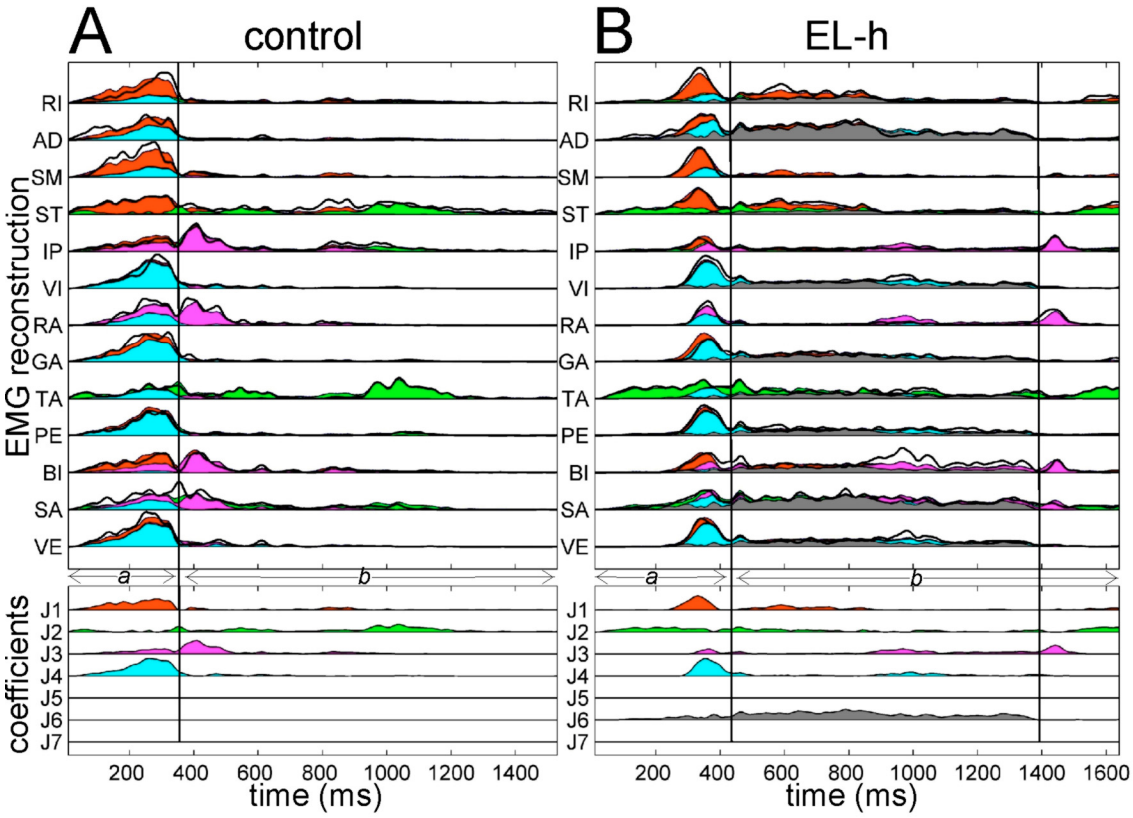


**FIGURE 4.16.** Reconstructing unloaded (control) and loaded (EL-h) EMGs using the extracted synergies and their corresponding activation coefficients. The jumping episodes depicted in Fig. 4.11A are reconstructed in this figure using synergies J1-J7 (Fig. 4.15A). In the top panels of both *A*

and *B*, the actual EMG data (rectified, filtered, and integrated) are depicted in thick black lines. The reconstructed EMGs are shown in colors matching those shown in the coefficient time traces (bottom panels) in such a way that, at any time point, the colors reflect the respective contribution of each synergy to the reconstruction. Notice that in *B*, the additional EMG phase in phase *b* is largely explained by the activation of synergy J6 (gray), a synergy specific to EL-h (Fig. 4.15A).

As in our previous analysis of data involving inertial loading, we also examined how the peak burst amplitude and burst duration of the coefficients for the shared synergies varied across conditions (Table 4.4). The coefficients of those synergies with complementary data set selections (marked by brackets in Fig. 4.15) were compared together as a single unit of activation. Some of the shared synergies showed a reversible increase in their activation burst peak amplitude after loading – for instance, the swimming synergy Sw7/Sw8, whose composition comprises TA and PE, two muscles with ankle flexor and knee extensor functions (Fig. 4.17B, bottom). For the terrestrial behaviors with data collected under both elastic loading conditions (EL-h and EL-hk), some synergies showed changes only in one of the two elastic loading conditions – for instance, the stepping synergy Sp8/Sp9/Sp10, showing a reversible increase in burst amplitude only in EL-h but not in EL-hk. One stepping synergy, however, exhibited increases in burst duration in both EL-h and EL-hk – synergy Sp4/Sp5, comprising muscles AD, VI, GA, BI, SA, and VE, and activated mostly during step extension. As shown in Fig. 4.18B, not only did the burst duration of these complementary synergies increase reversibly after EL-h and EL-hk ($p<0.05$), but stepping uphill under EL-hk also further increased the burst duration ($p<0.05$). These statistical results support strongly that the duration of activation of this stepping extension module is regulated constantly by changing sensory stimuli so that stepping can be accomplished even with an altered dynamic environment. Also, these changes in duration shown in Fig. 4.18B, and the fact that these complementary synergies include a prominent AD component in their compositions (Fig. 4.18A), are consistent with our earlier observation that the duration of the AD muscle was prolonged by both EL-h and EL-hk during stepping (Fig. 4.14C). Therefore, EMG changes associated with loading can also be described as altered activations of muscle synergies shared across the unloaded and loaded conditions.

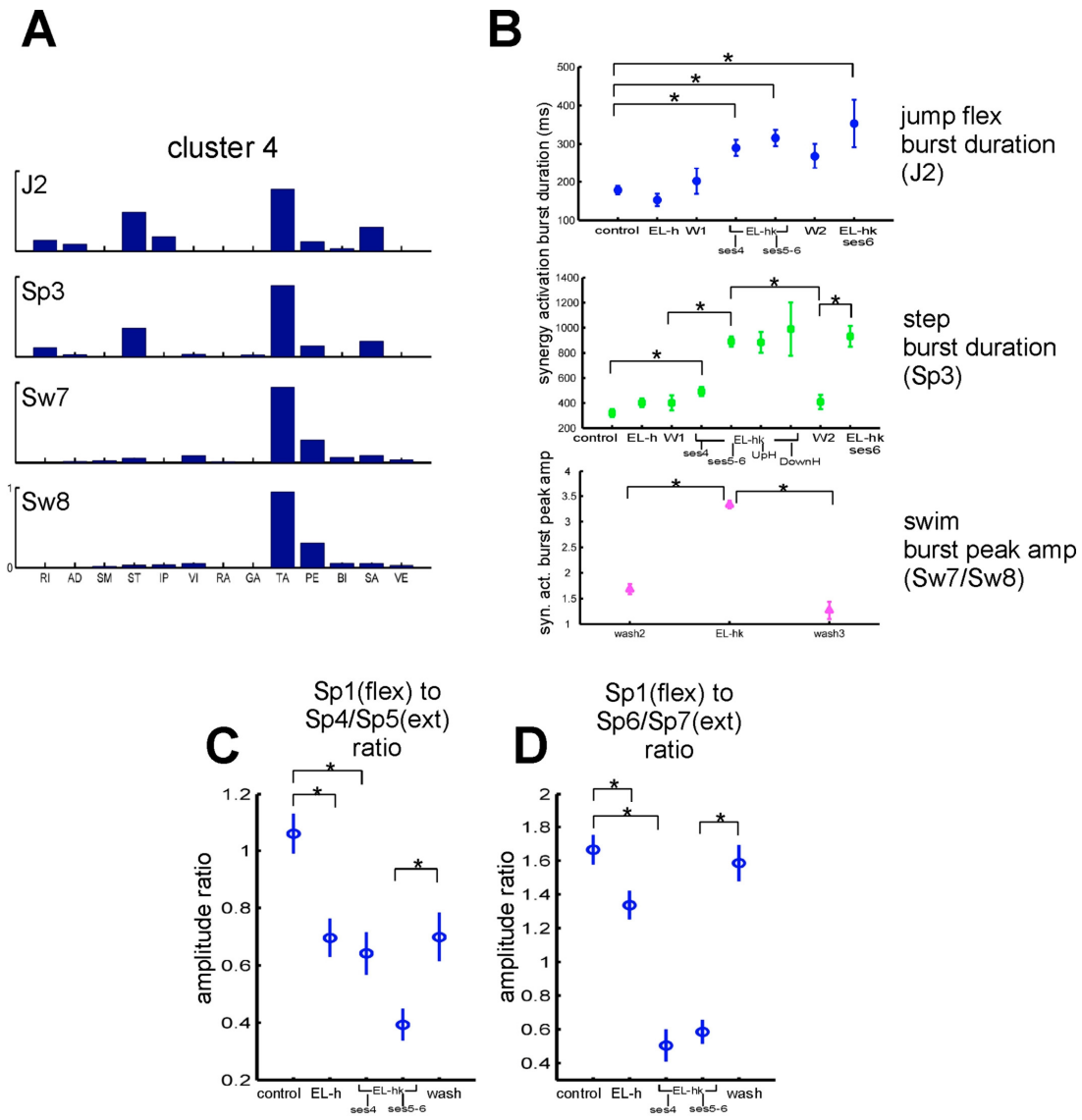


**FIGURE 4.17.** Clustering synergies of different behaviors obtained from the elastic loading experiment. *A*, Muscle synergies from cluster 4, featuring activation components in muscles ST, TA, PE, and SA (see also Table 4.4). Synergy labels here match those shown in Fig. 4.15. *B*, Statistics of burst peak amplitude and duration of the time-varying coefficients for the synergies shown in *A* (mean ± SE). Means were compared using multiple comparison statistics, and statistically significant differences ($p < 0.05$) are marked in the figure by *. *C*, *D*, The flexion-to-extension peak amplitude ratio for the coefficient bursts of two synergy pairs. The decrease in amplitude ratio under the loaded conditions corresponds well to the decrease in EMG amplitude ratio observed in Fig. 4.14B. See Results, "Describing EMG changes observed …" for more detailed descriptions.

The changes in flexor-to-extensor amplitude ratio we noticed earlier (Fig. 4.14B) also prompted us to calculate, for every step cycle, the ratio between the peak coefficient amplitude of a synergy during step flexion, and that of another synergy during step extension. Our observations in Fig. 4.14B predict that elastic loading decreases the flexion-to-extension amplitude ratio of certain synergy pairs. Indeed, we identified two pairs exhibiting such decreases in amplitude ratio: Sp1-flexion and Sp4/Sp5-extension, and Sp1-flexion and Sp6/Sp7-extension. As shown in Fig. 4.17C-D, for both pairs, the ratio between the coefficient peak amplitude of the flexion synergy during flexion, and that of the extension synergy during extension, decreased after both EL-h and EL-hk ($p<0.05$). Importantly, the flexion synergy of both pairs (Sp1) includes RA activation, and the extension synergies of both pairs (Sp4/Sp5 and Sp6/Sp7) include AD activation. Thus, these results concerning amplitude ratio of synergies (Fig. 4.17C-D) are consistent with the results described earlier concerning EMGs (Fig. 4.14B), further suggesting that some of the EMG changes associated with elastic loading can be attributed to alterations in the activation coefficients of invariant synergies.

Table 4.4 lists how the duration, peak amplitude, and the flexion-to-extension amplitude ratio of the coefficient bursts of each synergy were altered by either type of elastic loading. To summarize, our synergy and coefficient analyses together suggest that the EMG alterations observed after elastic loading can be described by (i) activation of an additional, load-specific module (Fig. 4.16); (ii) deletion of module, in the case of stepping (Fig. 4.15B); (iii) alterations in either the amplitude and/or duration of the coefficient bursts of invariant synergies (Table 4.4); and (iv) decreases in the flexion-to-extension amplitude ratio of synergy pairs (Fig. 4.17C-D).

**TABLE 4.4. Characterizing changes in burst duration and amplitude of shared synergies associated with elastic loading.**

| cluster | major muscles | behav. | duration | peak amplitude | remarks |
|---|---|---|---|---|---|
| cluster 1 | **RI**, **AD**, **SM**, **ST**, **GA**, PE, BI, (VE) | J1 | | | |
| | | Sp7 | EL-hk: ↑ | EL-hk: ↑ | paired w/ Sp6 |
| | | K1 | | | |
| cluster 2 | **RI**, **AD**, **SM**, VI, RA, **GA**, PE, BI, **VE** | Sp6 | EL-hk: ↑ | EL-hk: ↑ | paired w/ Sp7 |
| | | Sw1 | | EL-hk: ↑ | |
| cluster 3 | **RI**, **ST**, (GA) | Sp11 + Sp12 + Sp13 | | | not active in EL-hk |
| | | Sw5 + Sw6 | | | |
| cluster 4 | (ST), **TA**, **PE**, **SA** | J2 | EL-hk: phase *b*: ↑ | | |
| | | Sp3 | EL-hk: ↑ | | |
| | | K3 | | | |
| | | Sw7 + Sw8 | | EL-hk: ↑ | |
| cluster 5 | SM, **IP**, **RA**, **BI**, SA, **VE** | J3 | | EL-hk: flex-to-J1(ext) ratio ↓ | |
| | | Sp1 | | EL-h: flex-to-Sp4/5(ext) ratio ↓<br>EL-hk: flex-to-Sp6/7(ext) ratio ↓ | |
| | | K5 + K6 | | | |
| | | Sw3 | | | |
| cluster 6 | (ST), **IP**, **BI**, SA | Sp2 | EL-hk: ↑ | EL-hk: flex-to-Sp6/7 (ext) ratio ↓ | |
| | | K7 | | | in control only |
| | | Sw2 | | EL-hk: ↑ | |
| cluster 7 | **RI**, **AD**, ST, BI, **SA** | K4 | | | |
| | | Sw4 | | | |
| cluster 8 | **AD**, SM, **VI**, RA, **GA**, **PE**, SA, **VE** | J4 + J5 | | | |
| cluster 9 | **AD**, **VI**, **GA**, **PE**, BI, VE | J7 | | | active in EL-hk only |
| | | Sw12 | | | active in EL-hk only |
| cluster 10 | AD, **VI**, **GA**, PE, **VE** | Sp8 + Sp10 | | EL-h: ↑ | paired w/ Sp9 |
| cluster 11 | AD, **VI**, **GA**, **PE**, **VE** | Sp9 | | EL-h: ↑ | paired Sp8/10 |
| | | Sw9 + Sw10 + Sw11 | EL-hk: ↑ | | |
| cluster 12 | **AD**, **VI**, PE, **BI**, SA, **VE** | J6 | | | active in EL-h only |
| | | Sp4 + Sp5 | EL-h: ↑<br>EL-hk: ↑ | EL-h: ↑ | |
| | | K2 | | | |

**Clustering muscle synergies from different behaviors**

As before, in order to see whether similar synergies from different behaviors were also modulated similarly after loading, we grouped all synergies from the four behaviors into clusters, and compared the synergies, and their coefficient changes, within each cluster.

Our clustering algorithm classified all synergies shown in Fig. 4.15 into 12 clusters, summarized in Table 4.4. Three of the clusters contain synergies of different behaviors showing similar changes in the pattern of their activation coefficients after loading: cluster 2 (↑ in peak amplitude under EL-hk, in step and swim), cluster 4 (↑ in burst duration under EL-hk, in jump and step; Fig. 4.17A-B), and cluster 5 (↓ in flexion-to-extension amplitude ratio in EL-hk, in jump and step). These results indicate that the elastic load perturbation may elicit similar adaptive motor responses in different behaviors by modulating the same muscle synergy in a similar way.

It is also noteworthy, that one of the clusters (cluster 9) comprises two synergies, for jumping and swimming, respectively, both of which were extracted by our stage-II algorithm as synergies specific only to the EL-hk condition. That two similar load-specific synergies from two different behaviors and two different frogs were grouped under the same cluster further confirms that the finding of load-specific synergies is unlikely to be just a result of random chance.

More remarkably, another load-specific jumping synergy, J6, activated only in EL-h, was classified by the clustering algorithm as belonging to a cluster (cluster 12) comprising other synergies, for other behaviors, that are shared between the unloaded and loaded conditions. Shown in Fig. 4.18A are three synergies from this cluster, including the EL-h-specific jumping synergy J6, and the shared stepping synergies Sp4/Sp5. Synergies Sp4 and Sp5 constitute a complementary synergy pair whose data set selections together comprise all unloaded and loaded conditions. As described above, they were activated during step extension, and the burst duration of their coefficients was prolonged by both types of elastic loading (Fig. 4.18B). The similarity between the load-specific J6 and the shared Sp4/Sp5, as is evident in Fig. 4.18A, raises the possibility that the motor system may achieve motor adaptation in one behavior by activating another synergy normally utilized in another behavior. The fact that the burst duration of this stepping synergy was increased by loading during stepping (Fig. 4.18B) suggests that possibly, activating this set of muscles produces forces that can compensate for the elastic load well, so well that its activation during loaded

jumping might also compensate for the load despite that it is not normally used for constructing the jumping muscle pattern.

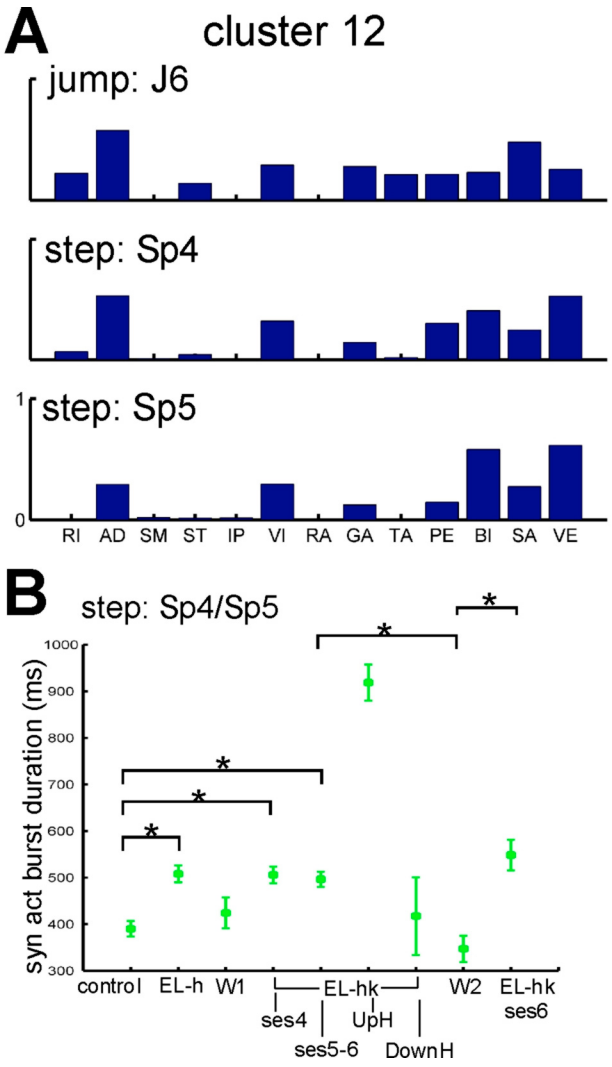


**FIGURE 4.18.** Similarity between a load-specific jumping synergy and a stepping extension synergy. *A*, Shown in the panel are three of the synergies grouped under cluster 12 by our hierarchical clustering analysis. All of them comprise activation components in muscles AD, VI, GA, PE, BI, SA, and VE. As depicted in Fig. 4.15, synergy J6 was found by our stage-II algorithm to be specific to the EL-h condition (Fig. 4.15A) while synergies Sp4/Sp5 constitute a synergy pair with complementary data set selections (Fig. 4.15B) activated in all unloaded and loaded conditions. Stepping EMG reconstruction (not shown) has shown that Sp4/Sp5 are responsible for explaining the EMGs of stepping extension. Their similarity to synergy J6 suggests that it might be possible for the motor system to compensate for perturbation in one behavior by activating another synergy normally used for another behavior. *B*, Statistics of burst duration of the activation coefficients for synergies Sp4/Sp5 (mean ± SE). Means were compared using multiple comparison statistics, and statistically significant differences ($p < 0.05$) are marked in the figure by *. The increase in coefficient burst duration after loading corresponds well to the observation of AD duration increase shown in Fig. 4.14C.

**Summary: main results of the elastic loading experiments**

Hindlimb movements of two frogs were perturbed by an elastic load provided by a rubber band attached distally to either the knee (EL-h) or the ankle (EL-hk) (Fig. 4.1B). As in our analyses of EMG data from the inertial loading experiments, we divided our analyses here into two stages. In analysis stage I, we show that the low-dimensionality conclusion is robust across the different elastic loading conditions (Table 4.3). Fitting the control synergies to the data of the loaded and washout conditions also yielded high $R^2$ values (Table 4.3). In analysis stage II, our reformulated NMF algorithm found many synergies with data set selections comprising all conditions as well as synergy groups with complementary data set selections (Fig. 4.15), suggesting that the muscle synergies extracted are robust across the different loading conditions. Reconstructions of EMGs using the extracted synergies and their coefficients reveal that the inserted EMG phase observed in some of the loaded jumping episodes (Fig. 4.11) can be explained largely by the activation of a load-specific synergy not normally utilized in the construction of the unloaded jumps (Fig. 4.16). Furthermore, elastic loading altered the temporal activation pattern of many shared synergies (Table 4.4, Fig. 4.17B, Fig. 4.18B), and decreased the flexion-to-extension amplitude ratio between some of the synergy pairs during stepping (Fig. 4.17C-D). Finally, cluster analysis reveals that a jumping load-specific synergy is very similar to a stepping synergy normally activated in step extension (Fig. 4.18A), raising the intriguing possibility that during one behavior, load compensation may sometimes be achieved by activating a synergy used normally for another behavior.

## DISCUSSION

**Muscle synergies are robust across different dynamic conditions**

One major result of the loading experiments reported in this study is that most of the muscle synergies underlying the natural motor behaviors examined (jumping, stepping, kicking, and swimming) remained invariant across the different loading and washout conditions. This conclusion is supported in analysis stage I by the finding that fitting the control synergies to the data sets of the other loaded and washout conditions resulted in high $R^2$ values (Tables 4.1 & 4.3), and more strongly, in analysis stage II in which our reformulated NMF selected data set selections including all conditions for many of the

extracted synergies (Figs. 4.8 & 4.15). This finding of muscle grouping invariance is surprising, given that the perturbations delivered in this study altered the systems dynamics in many different ways. In our inertial loading experiment, the additional weight not only increased the rotational moment of inertia, but also increased the calf's gravitational load; as a result of these increases, the interaction torques exerted onto the different joints during movements were likely changed as well (Sainburg *et al.*, 1999). In our elastic loading experiment, limb extension was resisted by the stiffness of the rubber band whereas limb flexion was assisted by the rubber band's elastic recoil; thus, the pattern of sensory inflow during movements was almost certainly altered by the load. The observation that many of the extracted muscle synergies remained invariant across these varying dynamic conditions suggests strongly that, the extracted synergies are likely to reflect some fundamental structures utilized by the CNS for movement construction rather than just features contingent upon specific patterns of sensory inflow during a particular behavior performed under a particular dynamic environment. This is consistent with the conclusions of a number of recent studies (Saltiel *et al.*, 2005; d'Avella *et al.*, 2006; Torres-Oviedo *et al.*, 2006; Tresch *et al.*, 2006).

From the perspective of the CNS, generating muscle activation patterns by combining synergies might simplify motor coordination in several ways. First, the number of synergies used is smaller than the number of recorded muscles, as observed in this study (Tables 4.1 & 4.3) and many others (e.g., d'Avella and Bizzi, 1998; Tresch *et al.*, 1999; Saltiel *et al.*, 2001). Using a small number of synergies with activation balance profiles spanning many muscles to organize muscle patterns could be a way for the CNS to circumvent the difficulty of controlling a large number of degrees of freedom (Bernstein, 1967) without losing too much flexibility. Second, activation of a synergy produces a particular joint torque pattern and/or a net endpoint force towards a specific direction. If such forces are related to some behaviorally relevant kinematic or biomechanical variables [such as the kick direction in the frog (d'Avella *et al.*, 2003), or forces for maintaining postural balance in the cat (Ting and Macpherson, 2005)], then using synergies to generate the appropriate joint torques for a given behavioral goal obviates the need to explicitly solve the inverse dynamics problem, which could be computationally complex (Mussa-Ivaldi and Bizzi, 2000).

**Sensory modulation of muscle synergies for motor adaptation**

Although it is clear from our results that many muscle synergies underlying the EMGs remained invariant across different dynamic conditions, both inertial and elastic loading elicited changes in the EMG pattern. For instance, inertial loading caused reversible and repeatable increases in the duration of RA in lateral kicks, caudal-lateral kicks, steps, swimming cycles, and jumps (Figs. 4.4 & 4.5); elastic loading, on the other hand, decreased the flexor-to-extensor amplitude ratio in steps (Figs. 4.13 & 4.14). Such alterations in both burst duration and amplitude are consistent with the results of many previous studies documenting modulations of EMG burst width and burst height associated with tonic limb perturbations (Happee, 1993; Hoffman and Strick, 1993; Schotland and Rymer, 1993; Gottlieb, 1996; Mackey *et al.*, 2002; Saltiel and Rossignol, 2004). Thus, muscle patterns elicited by altered sensory stimuli do play a prominent role in compensating for different external loads.

Many EMG changes reported in this thesis chapter were observed upon loading (Figs. 4.4B & 4.11), and some changes were reversed upon load removal (Fig. 4.5). These suggest that the EMG changes we noted were effected by some built-in, "ready-to-go" circuitries functioning as immediate compensatory mechanisms for adapting the behavior to the altered dynamic condition. It is possible that some EMG changes were the results of motor learning (in the sense that a new motor pattern emerges gradually over time), and that load removal did elicit an "aftereffect" similar to those reported in many studies of adaptation in reaching movements (Shadmehr and Mussa-Ivaldi, 1994; Shadmehr and Wise, 2005). However, since the frogs in our study were not trained or obliged to perform each behavior with fixed trajectories, there was substantial behavioral and EMG variability even in the control condition. Such data variability is desirable for studies like this one focusing on invariant EMG structures, but it is at the same time difficult to separate the variability attributable to possible motor learning or aftereffects from the natural behavioral variability without a precise model that can predict the trajectory from any EMG pattern. The EMG changes reported here, however, do seem to represent at least immediate neural responses for load compensation. This is supported by the observation that distributions of jumping and kicking varieties did not significantly change after inertial loading (Fig. 4.3), and that many EMG alterations seen in individual examples were validated at the population level (Figs. 4.6, 4.12 & 4.14).

The finding in stage II that many synergies remained invariant across all loaded and unloaded conditions (Figs. 4.8 & 4.15) and the fact that the EMG data of all conditions are described equally well by the extracted synergies, as enforced by the algorithm (Fig. 4.2), anticipate that many EMG changes we have noted can be described as changes in the coefficients of the shared synergies. Indeed, reconstructions of the EMGs using the synergies and their coefficients support this view (Figs. 4.9 & 4.16). Systematic comparison of the coefficient burst duration and amplitude across conditions shows that both the height and width of the activation bursts of a number of shared synergies were reversibly changed by loading (Tables 4.2 & 4.4; Figs. 4.10, 4.17 & 4.18). Together, these results argue for the hypothesis that, the temporal activation pattern of a group of robust, invariant synergies is constantly modulated by sensory afferents so that the amounts of joint torques produced by their respective activations can be adapted immediately to accommodate the changing dynamic requirements of the task. The type of adaptation achieved by such modulation of synergies is similar to what Pearson (2000) refers to as "short-term adaptation," or alterations in motor pattern that persist over a short to medium span of time, elicited for executing a behavior in a changed external environment (such as stepping uphill or swimming in a viscous medium).

Such a view of muscle synergies is not incompatible with the proposal that each synergy might be a low level controller of a behaviorally relevant kinematic (Cajigas-González, 2003) or biomechanical variable (Torres-Oviedo *et al.*, 2006). As a specific example, consider the stepping synergy Sp4/Sp5 (Fig. 4.18A), activated consistently during the extension phase (or the stance phase) of a step cycle. The behavioral goals of the stance phase include both supporting the body's gravitational load, and propelling the animal forward against the ground's friction (Duysens *et al.*, 2000). Suppose that co-activating the muscles composing this synergy – AD, VI, GA, PE, BI, SA, and VE – does produce a joint torque pattern suitable for carrying out these behavioral goals. If these two goals were made more difficult to accomplish as signaled by altered sensory stimuli from the stretched extensors, then increasing either the duration and/or amplitude of the synergy's activation would be of adaptive value. Indeed, as shown in Fig. 4.18B, when the limb was perturbed by an elastic load so that the hindlimb had to overcome an additional resistive force from the rubber band to propel the body forward to the same degree, the activation duration of this synergy was prolonged. When the frog stepped up an incline along with the elastic load so

that even more force was needed to support the body's gravitational load, its duration of activation increased further (Fig. 4.18B). These results demonstrate clearly how sensory modulation of the activation of a synergy controlling a global biomechanical variable could be adaptive to the animal. It is well possible that, the muscular compositions of the synergies represent an optimum between implementing a set biomechanical functions critical for the animal's survival, maximizing the adaptive values of the movements resulting from sensory modulation of the synergies during different behaviors, and accomplishing motor execution using the smallest possible number of parameters.

A control scheme consistent with the ideas presented above is depicted in Fig. 4.19. In this model, muscle synergies (S1, S2, and S3) are represented as centrally organized modules (Cheung *et al.*, 2005; Saltiel *et al.*, 2005) directly activated by feed-forward commands [$c_1(t)$, $c_2(t)$, and $c_3(t)$]. Each synergy is hypothesized to implicitly represent an aspect of the musculoskeletal dynamics relevant to a motor behavior. Motor execution is achieved by first mapping a desired behavioral goal to a small number of neural commands for activating the muscle synergies to produce the appropriate joint torque pattern. This map, denoted by *I* in the diagram, is analogous, but not equivalent, to an inverse dynamics computation, because the outputs of the map are not the actual joint torques required for executing the desired movement. An efference copy of the synergy activation commands (*eff.*) is sent to another network (*F*) capable of predicting the sensory consequences of the movement resulting from those neural commands. This map is thus analogous to a forward model of the musculoskeletal system. As the movement is being accomplished by activating the muscles (M1-M5) through the synergies, the actual sensory stimuli are transmitted back to the CNS from the periphery by group Ia, Ib, II as well as cutaneous afferent fibers. The actual sensory inflow [$s(t)$] is then compared against the predicted sensory inflow. Another network, *E*, then maps any deviation of the sensory signals from their predictions to modulatory neural signals (*mod.*) that alter the original activation pattern of the synergies so that adaptive responses could be elicited. Since $s(t)$ is itself a high-dimensional vector containing proprioceptive information from many muscles as well as cutaneous stimuli from many skin regions, the network *E* is a many-to-many map that potentially, but not necessarily, requires complex computations. A more sophisticated understanding of how the synergy modulatory signals can be computed easily from errors in the sensory signals would require further studies.

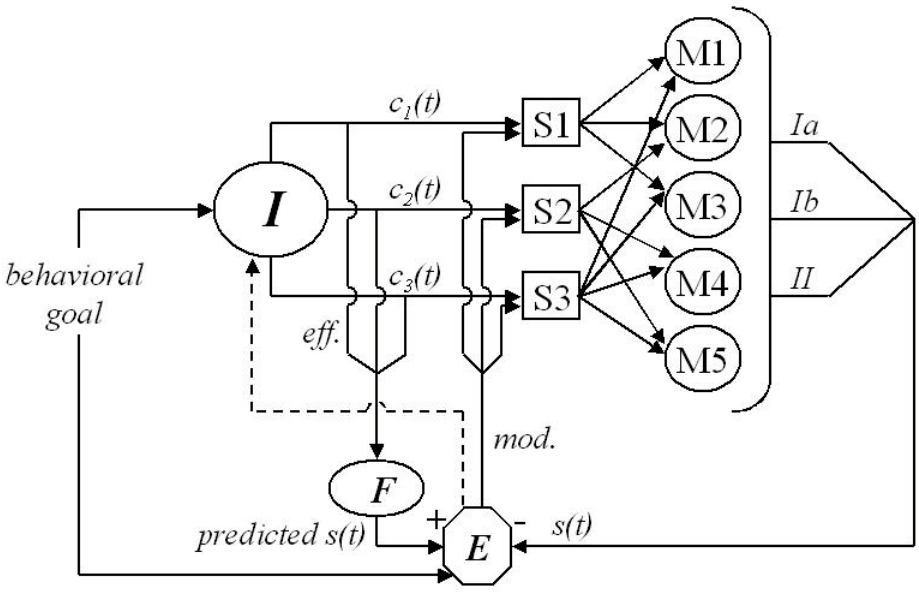


**FIGURE 4.19.** A control scheme consistent with the modulation of muscle synergies observed in the perturbation experiments described in this thesis chapter. In this model, muscle synergies (S1, S2, S3) activating different muscles (M1-M5) are represented as centrally organized modules directly activated by feed-forward, time-varying commands [$c_1(t)$, $c_2(t)$, $c_3(t)$], consistent with the conclusions presented in thesis chapter 3. Motor execution is achieved by first mapping a desired behavioral goal to a small number of synergy commands through a map, *I*, analogous (but not equivalent) to an inverse dynamics computation. An efference copy of the synergy commands (*eff.*) is sent to another network, *F*, capable of predicting the sensory consequences of the movement resulting from the sent commands. This prediction is then compared against the actual sensory signals, $s(t)$, conveyed through cutaneous inputs and groups Ia, Ib, and II fibers. Another network, *E*, then maps any error of sensory inputs to a set of modulatory signals (*mod.*) fine-tuning the activations of the muscle synergies. This *E* network is presumed to be state-dependent – i.e., the map between sensory error and *mod.* is expected to be a function of the behavior being executed. Also, the observation of a stepping synergy activated in jumping after elastic loading (Fig. 4.18) suggests that the inverse map, *I*, might be modified by large error signals (dotted line).

### Similar synergies for different behaviors modulated similarly by loading

We observed that there exist similar synergies, used for different behaviors, whose coefficient burst duration and/or amplitude were modulated similarly after loading (Figs. 4.10 & 4.17; Tables 4.2 & 4.4). This finding is not only consistent with previous reports of behavior-independent motor control modules (Jing *et al.*, 2004; d'Avella and Bizzi, 2005), but

also points to the possibility that, each shared synergy implements a biomechanical or kinematic function that is critical in the construction of several behaviors. Presumably, in those behaviors sharing the synergy, loading affects the function implemented by the shared synergy in similar ways, and thus, modulating its activation pattern similarly across those behaviors would result in adaptive responses (see also the previous section, "Sensory modulation of muscle synergies …"). An alternative interpretation is that the behaviors sharing the synergy in fact involve very different biomechanical functions, and the synergy used is just an optimum between increasing the capability of carrying out the behaviors successfully under the different biomechanical constraints, and maximizing the possible range of adaptive movements resulting from sensory modulation of its activation. Distinguishing these possibilities would again require many more studies of the biomechanics of the different frog behaviors (see, for instance, Kargo *et al.*, 2002).

**Synergy deletion after loading**

Our analyses of the data sets obtained from the elastic loading experiment reveal that under EL-hk, one synergy normally used for constructing the stepping EMGs (Sp11/Sp12/Sp13 in Fig. 4.15B) was deleted from the set of synergies underlying the stepping muscle pattern, analogous to earlier reports of module deletions (Stein and Daniels-McQueen, 2002, 2004). The deletion in our study is supported both by visual inspection of the stepping EMGs before and after loading (Fig. 4.13), and by the result that the data set selection assigned to this synergy by our stage-II algorithm includes control, EL-h, and wash, but not EL-hk-session-4 and EL-hk-sessions-5&6 (Fig. 4.15B). Thus, the normal, expected pattern of sensory inflow during some behaviors might be critical in activating a few synergies, suggesting that there might be control modules accessible only by sensory feedback signals, at least during those behaviors (Kargo and Giszter, 2000a). Such an interpretation is consistent with the notion that sensory feedback not only modulates the central pattern generators, but also plays a role in establishing features of the motor pattern (Pearson, 2004); our interpretation, however, provides an *explicit* mechanism specifying how the features established by feedback can be combined with the centrally organized patterns to produce the final motor program.

The specific synergy observed to be deleted in this study (Sp11/Sp12/Sp13 in Fig. 4.15B), however, does not appear to be accessible only by feedback, as this very same

synergy appeared as a swimming synergy activated in all conditions (Sw5/Sw6 in Fig. 4.15D). In fact, a similar synergy even seems to underlie the EMGs obtained from deafferented frogs (Cheung *et al.*, 2005, their Fig. 6). Hence, the magnitude of sensory influence on a synergy is itself dependent on the behavior being performed – that is, the gain of the feedback loop is itself a state-dependent parameter, likely to be modulated by descending signals (Pearson and Collins, 1993; Gottlieb, 1996; Burke, 1999; Rossignol *et al.*, 2006). In the model of synergy activation described above (Fig. 4.19), the network *E*, which maps the error in sensory signals to the synergy modulatory signals, is thus likely influenced by central descending commands specifying how this map should be related to the state of the system.

**Synergy addition after loading**

Aside from synergy deletion after loading, we also observed, in some of the loaded jumps (EL-h and EL-hk), expression of an additional synergy not normally utilized in the construction of the unloaded jumping EMG pattern (Fig. 4.16). This additional synergy might correspond to a built-in muscle pattern encoded in spinal and/or supraspinal structures that can be elicited by sensory stimuli for rapid corrective movements (Forssberg, 1979; Schotland and Rymer, 1993; Kargo and Giszter, 2000a).

What is more remarkable is that the additional synergy was activated within a new EMG phase inserted between the activations of two other synergies shared across the unloaded and loaded conditions (J4 & J3 in Fig. 4.16). Equally remarkable is that this additional synergy is very similar to the stepping synergy normally activated during step extension (Fig. 4.18). To explain these results, the model consisting only of synergies activated directly by central commands and modulated by sensory afferents (Fig. 4.19) is inadequate, for inserting a synergy of another behavior into a position within an established sequence of synergy activations involves reprogramming the map between the desired behavioral goal and the appropriate sequence of commands for synergy activations. We speculate that such immediate reprogramming might be accomplished by the sensory error signals influencing the network responsible for generating the synergy commands (Fig. 4.19, dotted line). To be more specific, in the examples shown in Fig. 4.16, it is conceivable that a connection between network *E* and network *I* (Fig. 4.19) is activated momentarily by a very large sensory error signal, causing the activation of the additional synergy J6, as well as the temporary suspension of the activations of synergies J3 and J2 while J6 is being activated.

This model of reprogramming synergy activations driven by sensory error is very speculative, but conceptually it is very similar to many models of motor learning involving an internal model with parameters gradually updated by motor command error (Wolpert *et al.*, 1998; Shadmehr and Wise, 2005).

**A novel method for extracting shared and specific synergies**

Our synergy analyses in this chapter are divided into two stages. In stage I, muscle synergies were extracted from each condition separately for determining the numbers of synergies sufficient to describe the EMG data well. Robustness of the synergies was assessed by fitting the control synergies to the data of the other loaded and washout conditions. Such a test of the generalizing potential of the synergies is the most obvious procedure to try (d'Avella *et al.*, 2006; Torres-Oviedo *et al.*, 2006), but it is also unclear as to what amount of $R^2$ decrease would indicate significant differences in the synergies underlying the different conditions. To account for this and other possibilities (see Methods, "Analysis stage II …"), we therefore developed an algorithm based on the NMF capable of extracting synergies, along with their corresponding data set selections, from the pooled data set comprising the EMGs of all conditions. The stage-II algorithm here is essentially an attempt to generalize the method, first proposed in Cheung *et al.* (2005) for comparing synergies of two conditions, to one suitable for comparing synergies of an arbitrary number of conditions. While the procedure in Cheung *et al.* (2005) assesses the degree of synergy sharing by comparing subspaces (see this thesis, ch. 3), the algorithm here searches for the data set selections that provide equally well descriptions of the EMGs of all conditions. Such a shift of strategy is necessary because it is unclear how one could accurately assess the dimensionality of a subspace (or more correctly, a sub-subspace) shared between more than three subspaces. We believe that our stage-II algorithm is a useful procedure that can be applied in other contexts for a rigorous and systematic assessment of the degree of feature sharing between many different data sets.

In this thesis chapter, we have presented experimental observations and analytic results arguing that sensory modulation of muscle synergies can be a mechanism of immediate or short-term adaptation during natural motor behaviors. It remains to be seen how motor learning or long-term adaptation can be achieved in a discrete motor system organized by a small number of muscle synergies.

# *Epilogue*

In their recent book, *The Plausibility of Life*, Kirschner and Gerhart (2005) try to reconcile the seeming contradiction between the bewildering diversity of life forms on planet Earth, and the recent finding in comparative genomics that many genes appear to have been conserved across the genomes of many species with different lineages. In their account, they coin the term, 'conserved core processes,' to describe some robust cellular mechanisms, each of which involving an ensemble of conserved proteins, that seem to have been integrated into the behaviors of diverse cell types ranging from bacteria to human neurons. They argue that defining these conserved core processes and understanding their interactions hold the key to resolving the paradox described above. It appears that during evolution, these conserved processes have been reused in different combinations, regulated by different external or internal signals, and expressed during different times in development, thereby giving rise to diverse phenotypes adapted to many environmental niches. These processes also appear to have been constructed in special ways, allowing them to provide critical cellular functions in wildly different contexts, and also, to be linked together easily into new combinations of processes.

Kirschner and Gerhart then proceed to argue that, evolutionary changes in phenotypes are facilitated by these stable, robust core processes. When an environmental change demands a new adaptive phenotype, nature does not construct another species anew from scratch. Novel morphological forms can arise from using the existing conserved core processes in different combinations, and regulating them with a different set of control signals. More importantly, phenotypic variations generated this way are likely to be less lethal than those resulting from random nucleotide mutations, which can easily disrupt some very critical cellular functions. Also, as a result of the robustness of the conserved core processes, integration of the functions subserved by the core processes within the new combination is expected to be easier. Therefore, even though the core processes can be viewed as constraints limiting the set of plausible life forms, they also "deconstrain" evolutionary changes (pp. 258-259), in the sense that their capacity to be reused differently increases the likelihood for any novel morphology to emerge.

This concept of conserved core processes in evolutionary changes bears striking resemblance to the concept of muscle synergy developed in this thesis. As described repeatedly in earlier chapters, flexible combination of a small set of muscle synergies may generate diverse motor patterns, just as different combinations of core processes may generate diverse phenotypes. As argued in chapter 1, muscle synergies may serve to simplify control by eliminating motor patterns that can lead to uncoordinated movements, and this role of synergies is analogous to the proposal that generating new phenotypes by recombining existing core processes may reduce lethality. As demonstrated in chapters 3 and 4, muscle synergies appear to be robust neural constraints insensitive to different perturbations, but the conserved core processes also appear to be robust modules (see also Schlosser, 2004) expressed in diverse species coming from different lineages. Finally, as shown in chapter 4, motor adaptation during one behavior may sometimes be achieved by activating a synergy normally used for another behavior, and this possibility also corresponds nicely to the hypothesis that many adaptive evolutionary changes in phenotypes are achieved by recombining a set of existing conserved cellular processes.

Thus, the construction of natural motor behaviors by combinations of muscle synergies can be viewed as a special manifestation of a much more general mechanism utilized by nature for generating diverse patterns from a small number of building blocks. In this mechanism, the robustness of the building blocks and their readiness to be linked together in new combinations greatly facilitate the emergence of novel patterns, thereby allowing rapid adaptation of a biological system – be it a species, or the motor system of a species – to occur in an environment that changes constantly, and often, unpredictably. This relationship between the muscle synergy hypothesis and a possibly very fundamental principle underlying all biological phenomena is precisely what makes the quest for muscle synergies such an intellectually satisfying journey.

# References

Ajiboye A, Weir R (2006) Analysis of shared and specific neuromuscular synergies of hand grasp patterns at varying force levels. *Neural control of movements 16th annual meeting abstracts*, **11**: D-06.

Akaike H (1973) Information theory and an extension of the maximum likelihood principle. In: *Second international symposium on information theory* (Petrov B.N., and Csaki F., Eds), pp. 267-281. Budapest: Academiai Kiado.

Bates DM, Watts, DG (1988) *Nonlinear regression analysis and its applications*. New York: Wiley.

Bell AJ, Sejnowski TJ (1995) An information-maximisation approach to blind source separation and blind deconvolution. *Neural Comput.* **7**: 1129-1159.

Bellman RE (1961) *Adaptive control processes*. Princeton, NJ: Princeton UP.

Berniker M (2005) Linearity, motor primitives and low-dimensionality in the spinal organization of motor behavior. Ph.D. thesis, Massachusetts Institute of Technology.

Bernstein N (1967) *The co-ordination and regulation of movements*. Oxford: Pergamon.

Bizzi E, Mussa-Ivaldi FA, Giszter S (1991) Computations underlying the execution of movement: a biological perspective. *Science* **253**: 287-291.

Bizzi E, Hogan N, Mussa-Ivaldi FA, Giszter S (1992) Does the nervous system use equilibrium-point control to guide single and multiple joint movements? *Behav. Brain Sci.* **15**: 603-613.

Brady M, Hollerbach J, Johnson T, Lozano-Perez T, Mason M (1982) *Robot motion: planning and control*. Cambridge, MA: MIT Press.

Brooks VB (1986) *The neural basis of motor control*. New York: Oxford UP.

Brown TG (1911) The intrinsic factors in the act of progression in the mammal. *Proc. R. Soc. Lond. B Biol. Sci.* **84**: 308-319.

Browne MW (2000) Cross-validation methods. *J. Math. Psychol.* **44**: 108-132.

Burke RE (1999) The use of state-dependent modulation of spinal reflexes as a tool to investigate the organization of spinal interneurons. *Exp. Brain Res.* **128**: 263-277.

Cajigas-González I (2003) Linear control model of the spinal processing of descending neural signals. Masters thesis, Massachusetts Institute of Technology.

Cappellini G, Ivanenko YP, Poppele RE, Lacquaniti F (2006) Motor patterns in human walking and running. *J. Neurophysiol.* **95**: 3426-3437.

Cheung VCK, d'Avella A, Tresch MC, Bizzi E (2005) Central and sensory contributions to the activation and organization of muscle synergies during natural motor behaviors. *J. Neurosci.* **25**(27): 6419-6434.

Cheung VCK, Tresch MC (2005) Non-negative matrix factorization algorithms modeling noise distributions within the exponential family. *Proc. IEEE Eng Med Biol 27th annl conf* (Shanghai, China, Sept 1-4, 2005), 4990-4993.

Clarac F (1991) How do sensory and motor signals interact during locomotion? In: *Motor control: concepts and issues* (Humphrey DR, Freund H-J, ed.), pp. 199-221. New York: John Wiley & Sons.

Danyan P, Abbott LF (2001) *Theoretical neuroscience.* Cambridge, MA: MIT Press.

d'Avella A (2000) Modular control of natural motor behaviors. Ph.D. thesis, Massachusetts Institute of Technology.

d'Avella A, Bizzi E (1998) Low dimensionality of supraspinally induced force fields. *Proc. Natl. Acad. Sci. USA* **95**: 7711-7714.

d'Avella A, Bizzi E (2005) Shared and specific muscle synergies in natural motor behaviors. *Proc. Natl. Acad. Sci. USA* **102**(8): 3076-3081.

d'Avella A, Portone A, Fernandez L, Lacquaniti F (2006) Control of fast-reaching movements by muscle synergy combination. *J. Neurosci.* **26**(30): 7791-7810.

d'Avella A, Saltiel P, Bizzi E (2003) Combinations of muscle synergies in the construction of a natural motor behavior. *Nat. Neurosci.* **6**(3): 300-308.

d'Avella A, Tresch MC (2002) Modularity in the motor system: decomposition of muscle patterns as combinations of time-varying synergies. In: *Advances in neural information processing, vol. 14* (Dietterich TG, Becker S, Ghahramani Z, ed.), pp. 141-148. Cambridge, MA: MIT Press.

Delcomyn F (1980) Neural basis of rhythmic behavior in animals. *Science* **210**: 492-498.

Duysens J, Clarac F, Cruse H (2000) Load-regulating mechanisms in gait and posture: comparative aspects. *Physiol. Rev.* **80**(1): 84-133.

Ecker A (1971) *The anatomy of the frog* (Haslam G, tran). Amsterdam: A. Asher & Co N.V.

Flash T, Hochner B (2005) Motor primitives in vertebrates and invertebrates. *Curr. Opi. Neurobiol.* **15**: 660-666.

Forssberg H (1979) Stumbling corrective reaction: a phase-dependent compensatory reaction during locomotion. *J. Neurophysiol.* **42**: 936-953.

Freitas SMSF, Duarte M, Latash ML (2006) Two kinematic synergies in voluntary whole-body movements during standing. *J. Neurophysiol.* **95**: 636-645.

Full RJ, Koditschek DE (1999) Templates and anchors: neuromechanical hypotheses of legged locomotion on land. *J. Exp. Biol.* **202**: 3325-3332.

Giuliani CA, Smith JL (1987) Stepping behaviors in chronic spinal cats with one hindlimb deafferented. *J. Neurosci.* **7**(8): 2537-2546.

Goldberger ME (1988) Partial and complete deafferentation of cat hindlimb: the contribution of behavioral substitution to recovery of motor function. *Exp. Brain Res.* **73**: 343-353.

Golub GH, Van Loan CF (1983) *Matrix computations.* Baltimore, MD: Johns Hopkins UP.

Gottlieb GL (1996) On the voluntary movement of compliant (inertial-viscoelastic) loads by parcellated control mechanisms. *J. Neurophysiol.* **76**(5): 3207-3229.

Greene PH (1972) Problems of organization of motor systems. In: *Progress in theoretical biology, vol. 2* (Rosen R, Snell FM, ed.), pp. 303-338. New York: Academic Press.

Gribble PL, Ostry DJ (1999) Compensation for interaction torques during single- and multijoint limb movement. *J. Neurophysiol.* **82**: 2310-2326.

Grillner S (1975) Locomotion in vertebrates: central mechanisms and reflex interaction. *Physiol. Rev.* **55**(2): 247-304.

Grillner S (1981) Control of locomotion in bipeds, tetrapods, and fish. In: *Handbook of Physiology, sec. 1* (Brooks VB ed.), pp1179-1236. Bethesda, MD: American physiological society.

Grillner S (1985) Neurobiological bases of rhythmic motor acts in vertebrates. *Science* **228**: 143-149.

Grillner S, Zangger P (1984) The effect of dorsal root transection on the efferent motor pattern in the cat's hindlimb during locomotion. *Acta Physiol. Scand.* **120**: 393-405.

Happee R (1993) Goal-directed arm movements. III: Feedback and adaptation in response to inertial perturbations. *J. Electromyography Kinesiology* **3**(2): 112-122.

Harris CM, Wolpert DM (1998) Signal-dependent noise determines motor planning. *Nature* **394**: 780-784.

Hart CB, Giszter SF (2004) Modular premotor drives and unit bursts as primitives for frog motor behaviors. *J. Neurosci.* **24**(22): 5269-5282.

Hays WL (1994) *Statistics.* Belmont, CA: Wardsworth.

Hiebert GW, Pearson KG (1999) Contributions of sensory feedback to the generation of extensor activity during walking in the decerebrate cat. *J. Neurophysiol.* **81**: 758-770.

Hoffman DS, Strick PL (1993) Step-tracking movements of the wrist. III. Influence of changes in load on patterns of muscle activity. *J. Neurosci.* **13**(12): 5212-5227.

Hogan N (1988) Planning and execution of multijoint movements. *Can. J. Physiol. Pharmacol.* **66**: 508-517.

Hollerbach JM (1982) Computers, brains and the control of movement. *Trends Neurosci.* **5**: 189-192.

Hollerbach JM, Flash T (1982) Dynamic interactions between limb segments during planar arm movements. *Biol. Cybern.* **44**: 67-77.

Hyvärinen A, Oja E (2000) Independent component analysis: algorithms and applications. *Neural Netw.* **13**: 411-430.

Ivanenko YP, Poppele RE, Lacquaniti F (2004) Five basic muscle activation patterns account for muscle activity during human locomotion. *J. Physiol.* **556**: 267-282.

Jankowska E (1992) Interneuronal relay in spinal pathways from proprioceptors. *Prog. Neurobiol.* **38**: 335-378.

Jerard RB (1976) Application of a unified theory for simultaneous multiple axis artificial arm control. PhD degree thesis, University of Utah.

Jing J, Cropper EC, Hurwitz I, Weiss KR (2004) The construction of movement with behavior-specific and behavior-independent modules. *J. Neurosci.* **24**(28): 6315-6325.

Johnson RA, Wichern DW (2002) *Applied multivariate statistical analysis.* Upper Saddle River, NJ: Prentice Hall.

Jolliffe IT (2002) *Principal component analysis*. New York: Springer.

Kandel ER, Schwartz JH, Jessell TM (2000) *Principles of neural science* (4th ed.). New York: McGraw-Hill.

Kargo WJ, Giszter SF (2000a) Rapid correction of aimed movements by summation of force-field primitive. *J. Neurosci.* **20**(1): 409-426.

Kargo WJ, Giszter SF (2000b) Afferent roles in hindlimb wipe-reflex trajectories: free-limb kinematics and motor patterns. *J. Neurophysiol.* **83**: 1480-1501.

Kargo WJ, Nelson F, Rome LC (2002) Jumping in frogs: assessing the design of the skeletal system by anatomically realistic modeling and forward dynamic simulation. *J. Exp. Biol.* **205**: 1683-1702.

Kargo WJ, Nitz DA (2003) Early skill learning is expressed through selection and tuning of cortically represented muscle synergies. *J. Neurosci.* **23**(35): 11255-11269.

Kargo WJ, Rome LC (2002) Functional morphology of proximal hindlimb muscles in the frog Rana pipiens. *J. Exp. Biol.* **205**: 1987-2004.

Kirschner MW (2005) The meaning of systems biology. *Cell* **121**: 503-504.

Kirschner MW, Gerhart JC (2005) *The plausibility of life.* New Haven, CT: Yale UP.

Koshland GF, Smith JL (1989) Mutable and immutable features of paw-shake responses after hindlimb deafferentation in the cat. *J. Neurophysiol.* **62**: 162-173.

Krishnamoorthy V, Goodman S, Zatsiorsky V, Latash ML (2003) Muscle synergies during shifts of the center of pressure by standing persons: identification of muscle modes. *Biol. Cybern.* **89**: 152-161.

Krouchev N, Kalaska JF, Drew T (2006) Sequential activation of muscle synergies during locomotion in the intact cat as revealed by cluster analysis and direct decomposition. *J. Neurophysiol.* **96**: 1991-2010.

Kugler PN, Kelso JAS, Turvey MT (1980) On the concept of coordinative structures as dissipative structures: I. Theoretical lines of convergence. In: *Tutorials in motor behavior* (Stelmach GE, Requin J, ed.), pp. 3-47. Amsterdam: North-Holland.

Lee DD, Seung HS (1999) Learning the parts of objects by non-negative matrix factorization. *Nature* **401**: 788-791.

Lee DD, Seung HS (2001) Algorithms for non-negative matrix factorization. In: *Advances in neural information processing systems, vol. 13* (Leen TK, Dietterich TG, Tresp V, ed), pp556-562. Cambridge, MA: MIT Press.

Lee WA (1984) Neuromuscular synergies as a basis for coordinated intentional action. *J. Motor Behav.* **16**(2): 135-170.

Loeb EP, Giszter SF, Borghesani P, Bizzi E (1993) Effects of dorsal root cut on the forces evoked by spinal microstimulation in the spinalized frog. *Somatosens. Mot. Res.* **10**: 81-95.

Loeb GE (1993) The distal hindlimb musculature of the cat: interanimal variability of locomotor activity and cutaneous reflexes. *Exp. Brain Res.* **96**: 125-140.

Mai MT, Lieber RL (1990) A model of semitendinosus muscle sarcomere length, knee and hip joint interaction in the frog hindlimb. *J. Biomech.* **23**(3): 271-279.

Mackey DC, Meichenbaum DP, Shemmell J, Riek S, Carson RG (2002) Neural compensation for compliant loads during rhythmic movement. *Exp. Brain Res.* **142**: 409-417.

Macpherson JM (1991) How flexible are muscle synergies? In: *Motor control: concepts and issues* (Humphrey DR, Freund H-J, ed.), pp. 33-47. New York: John Wiley & Sons.

Marder E, Bucher D (2001) Central pattern generators and the control of rhythmic movements. *Curr. Biol.* **11**:R986-R996.

McCrea DA (2001) Spinal circuitry of sensorimotor control of locomotion. *J. Physiol.* **533.1**: 41-50.

Mussa-Ivaldi FA (1997) Nonlinear force fields: a distributed system of control primitives for representing and learning movements. In: *Proceedings of the 1997 IEEE international symposium on computational intelligence in robotics and automation*, pp. 84-90. New York: IEEE Press.

Mussa-Ivaldi FA, Bizzi E (2000) Motor learning through the combination of primitives. *Phil. Trans. R. Soc. Lond. B* **355**: 1755-1769.

Nauwelaerts S, Aerts P (2002) Two distinct gait types in swimming frogs. *J. Zool.* **258**: 183-188.

Olson JM, Marsh RL (1998) Activation patterns and length changes in hindlimb muscles of the bullfrog Rana catesbeiana during jumping. *J. Exp. Biol.* **201**: 2763-2777.

Overduin SA (2006) Neuromuscular modularity and behavioral correlates of motor control. PhD thesis, Massachusetts Institute of Technology.

Pearson KG (2000) Neural adaptation in the generation of rhythmic behavior. *Annu. Rev. Physiol.* **62**: 723-753.

Pearson KG (2004) Generating the walking gait: role of sensory feedback. *Prog. Brain Res.* **143**: 123-129.

Pearson KG, Collins DF (1993) Reversal of the influence of group Ib afferents from plantaris on activity in medial gastrocnemius muscle during locomotor activity. *J. Neurophysiol.* **70**: 1009-1017.

Perret C, Cabelguen J-M (1980) Main characteristics of the hindlimb locomotor cycle in the decorticate cat with special reference to bifunctional muscles. *Brain Res.* **187**: 333-352.

Poggio T, Bizzi E (2004) Generalization in vision and motor control. *Nature* **431**: 768-774.

Pratt CA, Buford JA, Smith JL (1996) Adaptive control for backward quadrupedal walking V. Mutable activation of bifunctional thigh muscles. *J. Neurophysiol.* **75**: 832-842.

Prochazka A (1996) Proprioceptive feedback and movement regulation. In: *Handbook of physiology, sec. 12* (Rowell LB, Shepherd JT, ed), pp89-127. New York: Oxford UP.

Raasch CC, Zajac FE (1999) Locomotor strategy for pedaling: muscle groups and biomechanical functions. *J. Neurophysiol.* **82**: 515-525.

Roberts TJ, Marsh RL (2003) Probing the limits to muscle-powered accelerations: lessons from jumping bullfrogs. *J. Exp. Biol.* **206**: 2567-2580.

Rossignol S (1996) Neural control of stereotypic limb movements. In: *Handbook of physiology, sec. 12* (Rowell LB, Shepherd JT, ed), pp173-216. New York: Oxford UP.

Rossignol S, Dubuc R, Gossard J-P (2006) Dynamic sensorimotor interactions in locomotion. *Physiol. Rev.* **86**: 89-154.

Sabatini AM (2002) Identification of neuromuscular synergies in natural upper-arm movements. *Biol. Cybern.* **86**: 253-262.

Sainburg RL, Ghez C, Kalakanis D (1999) Intersegmental dynamics are controlled by sequential anticipatory, error correction, and postural mechanisms. *J. Neurophysiol.* **81**: 1045-1056.

Saltiel P, Rossignol S (2004) Critical points in the forelimb fictive locomotor cycle and motor coordination: evidence from the effects of tonic proprioceptive perturbations in the cat. *J. Neurophysiol.* **92**: 1329-1341.

Saltiel P, Wyler-Duda K, d'Avella A, Ajemian RJ, Bizzi E (2005) Localization and connectivity in spinal interneuronal networks: the adduction-caudal extension-flexion rhythm in the frog. *J. Neurophysiol.* **94**: 2120-2138.

Saltiel P, Wyler-Duda K, d'Avella A, Tresch MC, Bizzi E (2001) Muscle synergies encoded within the spinal cord: evidence from focal intraspinal NMDA iontophoresis in the frog. *J. Neurophysiol.* **85**: 605-619.

Schlosser G (2004) The role of modules in development and evolution. In: *Modularity in development and evolution* (Schlosser G, Wagner GP, ed.), pp. 519-582. Chicago: University of Chicago Press.

Scholz JP, Schöner G (1999) The uncontrolled manifold concept: identifying control variables for a functional task. *Exp. Brain Res.* **126**: 289-306.

Schotland JL, Rymer WZ (1993) Wipe and flexion reflexes of the frog. II. Responses to perturbations. *J. Neurophysiol.* **69**(5): 1736-1748.

Schouenborg J (2002) Modular organisation and spinal somatosensory imprinting. *Brain Res. Brain Res. Rev.* **40**: 80-91.

Shadmehr R, Mussa-Ivaldi FA (1994) Adaptive representation of dynamics during learning of a motor task. *J. Neurosci.* **14**(5): 3208-3224.

Shadmehr R, Wise SP (2005) *The computational neurobiology of reaching and pointing.* Cambridge, MA: MIT Press.

Shemmell J, Forner M, Tresilian JR, Riek S, Barry BK, Carson RG (2005) Neuromuscular adaptation during skill acquisition on a two degree-of-freedom target-acquisition task: isometric torque production. *J. Neurophysiol.* **94**: 3046-3057.

Smith JL, Hoy MG, Koshland GF, Phillips DM, Zernicke RF (1985) Intralimb coordination of the paw-shake response: a novel mixed synergy. *J. Neurophysiol.* **54**: 1271-1281.

Soffe SR (1993) Two distinct rhythmic motor patterns are driven by common premotor and motor neurons in a simple vertebrate spinal cord. *J. Neurosci.* **13**(10): 4456-4469.

Stein PSG (2005) Neuronal control of turtle hindlimb motor rhythms. *J. Comp. Physiol. [A]* **191**: 213-229.

Stein PSG, Daniels-McQueen S (2002) Modular organization of turtle spinal interneurons during normal and deletion fictive rostral sratching. *J. Neurosci.* **22**(15): 6800-6809.

Stein PSG, Daniels-McQueen S (2004) Variations in motor patterns during fictive rostral scratching in the turtle: knee-related deletions. *J. Neurophysiol.* **91**: 2380-2384.

Stein PSG, Smith JL (1997) Neural and biomechanical control strategies for different forms of vertebrate hindlimb motor tasks. In: *Neurons, networks, and motor behavior* (Stein PSG, Grillner S, Selverston AI, Stuart DG, ed.), pp61-73. Cambridge, MA: MIT Press.

Sugiuchi Y, Kakei S, Izawa Y, Shinoda Y (2004) Functional synergies among neck muscles revealed by branching patterns of single long descending motor-tract axons. *Prog. Brain Res.* **143**: 411-421.

Székely G, Czéh G, Vörös G (1969) The activity pattern of limb muscles in freely moving normal and deafferented newts. *Exp. Brain Res.* **9**: 53-62.

Ting LH, Kautz SA, Brown DA, Zajac FE (1999) Phase reversal of biomechanical functions and muscle activity in backward pedaling. *J. Neurophysiol.* **81**: 544-551.

Ting LH, Kautz SA, Brown DA, Zajac FE (2000) Contralateral movement and extensor force generation alter flexion phase muscle coordination in pedaling. *J. Neurophysiol.* **83**: 3351-3365.

Ting LH, Macpherson JM (2005) A limited set of muscle synergies for force control during a postural task. *J. Neurophysiol.* **93**: 609-613.

Torres-Oviedo G, Macpherson JM, Ting LH (2006) Muscle synergy organization is robust across a variety of postural perturbations. *J. Neurophysiol.* **96**: 1530-1546.

Tresch MC, Cheung VCK, d'Avella A (2006) Matrix factorization algorithms for the identification of muscle synergies: evaluation on simulated and experimental data sets. *J. Neurophysiol.* **95**: 2199-2212.

Tresch MC, Saltiel P, Bizzi E (1999) The construction of movement by the spinal cord. *Nat. Neurosci.* **2**(2): 162-167.

Tresch MC, Saltiel P, d'Avella A, and Bizzi E (2002) Coordination and localization in spinal motor system. *Brain Res. Brain Res. Rev.* **40**: 66-79.

Tuller B, Turvey MT, Fitch HL (1982) The Bernstein perspective: II. The concept of muscle linkage or coordinative structure. In: *Human motor behavior: an introduction* (Kelso JAS, ed.), pp. 253-270. Hillsdale, NJ: Lawrence Erlbaum Associates.

Turvey MT, Fitch HL, Tuller B (1982) The Bernstein perspective: I. The problems of degrees of freedom and context-conditioned variability. In: *Human motor behavior: an introduction* (Kelso JAS, ed.), pp. 239-252. Hillsdale, NJ: Lawrence Erlbaum Associates.

Weiss EJ, Flanders M (2004) Muscular and postural synergies of the human hand. *J. Neurophysiol.* **92**: 523-535.

Whelan PJ (1996) Control of locomotion in the decerebrate cat. *Prog. Neurobiol.* **49**: 481-515.

Wolpaw J, Cohen L, Nielsen J, Bouyer L, Eyre J (2006) Cortical control of spinal cord plasticity: it's a long-term story. *Neural Control of Movements 16th Annual Meeting Abstracts* **11**: 06.1.

Wolpert DM, Miall RC, Kawato M (1998) Internal models in the cerebellum. *Trends Cog. Sci.* **2**: 338-347.

Zernicke RF, Smith JL (1996) Biomechanical insights into neural control of movement. In: *Handbook of physiology, sec. 12* (Rowell LB, Shepherd JT, ed), pp. 293-330. New York: Oxford UP.